Study of the non-thermal character of electron distribution functions in the solar wind

Štěpán Štverák

Jointly Supervised PhD between

Czech Technical University in Prague
Faculty of Nuclear Science and Physical Engineering

And

University Pierre et Marie Curie
École Doctorale Astronomie et Astrophysique
d'Île-de-France

Thesis

Study of the non-thermal character of electron distribution functions in the solar wind

Štěpán Štverák

Directors of the thesis:

IAP, Prague	*Paris Observatory*
Pavel Trávníček	Milan Maksimović
	André Mangeney

Defended 11^{th} *May* 2009

Jury: Laurence Rezeau
Philippe Loaurn
S. Peter Gary
Pavel Trávníček
Milan Maksimović
André Mangeney
Petr Hellinger

Jointly Supervised PhD between

Thesis

Study of the non-thermal character of electron distribution functions in the solar wind

Štěpán Štverák

Directors of the thesis:

IAP, Prague
Pavel Trávníček

Paris Observatory
Milan Maksimović
André Mangeney

Contents

Preface

The solar wind, a continuous stream of charged particles emitted from the very hot solar corona, represents a great opportunity to study astrophysical plasmas directly by *in situ* measurements. As an enormous bubble it extends from the Sun out beyond the planets to the heliopause where its pressure is balanced by the pressure of the local interstellar medium. Such a wind should be considered to be easily explained because the particles in the hot solar atmosphere already have velocities greater than the local escape velocity. However, after more than fifty years of a detail discovery by many space-borne instruments, scientists still do not understand the subtle plasma physics behind the process of the solar wind expansion into the interplanetary space. The problem boils down to two broad questions: *(i)* what are the initial conditions at the base of the solar wind - in the corona, and *(ii)* how the expanding solar wind transport the heat from the corona out to the interplanetary space. In situ observations and recent advances in the theoretical plasma physics show that kinetic processes could represent the key to most of the unsolved solar wind puzzles. Therefore, a detail study of observed particle velocity distribution functions is greatly important.

Solar wind plasmas, made up primarily of protons ($\sim 95\%$) and alpha particles ($\sim 4\%$) with some trace heavier ions, are found to be quiet tenuous while relatively hot at once. In such a medium the effect of Coulomb collisions, representing the basic driving mechanism which maintains a gas locally in the thermodynamic equilibrium, is quite limited. Moreover, as the mean free path rapidly increases with particle velocity, particle velocity distribution functions are expected to develop many non-thermal properties And indeed, *in situ* observations exhibit deviations from thermodynamic equilibrium, i.e., from the Maxwellian velocity distribution function, for protons (drifting beams) as well for solar wind electrons (high-energy non-thermal tails, skewness along the magnetic field).

Electrons, because of their small mass, do not play a significant role for the overall transport of solar wind momentum. However, they ensure the local quasi neutrality, produce an ambipolar electric field through their thermal pressure gradient and above all carry the heat. The electron velocity distribution functions (eVDFs) observed in the solar wind typically consist of a thermal core and non-thermal tails. The core electrons represent in average roughly 95% of the total number density. Despite of theoretical predictions, the ratio of the parallel and perpendicular temperatures of the core component is surprisingly observed very close to unity and the core of observed eVDFs is typically almost isotropic. The high-energy tails consist actually of two different components: a halo and a strahl. While the halo tails are

present at all pitch angles, the strahl appears as a beam-like population moving away from the Sun highly focused along the ambient magnetic field. Since the core remains almost isotropic or at least symmetric in the rest plasma frame, the strahl component represents the main factor of the overall heat transport, that is one of the most important characteristics for understanding the solar wind acceleration and consequent expansion. What are the main phenomena driving the electron populations in the course of the solar wind expansion and how much they really affect the shape of the electron distributions and its components? This is the principal question and main objective of the current study.

In order to better understand the non-thermal features of observed eVDFs as well as the transport of the heat in the solar wind, we performed a statistical study of a substantial amount of measured eVDFs. All the eVDF samples were acquired in the low ecliptic latitudes covering the heliocentric distance from 0.3 up to 4 AU. In order to provide a substantial amount of electron observations covering a sufficiently large heliocentric radial range we combine data acquired on board four spacecraft, namely Helios I&II, Cluster II and Ulysses.

All electron parameters are estimated by fitting of measured eVDFs with a model distribution function. For our study, a new model was proposed which, for the first time, describes all three components of the solar wind eVDFs (i.e. the core, the halo and the strahl) analytically. Two main goals of the present work are *(i)* to examine the radial evolution of main eVDF characteristics, i.e., the density, the temperature and the heat flux, with increasing heliocentric distance; and *(ii)* to study the effect of possible mechanism which can provide some additional heating or energy dissipation to solar wind electrons and moderate thus the shape of observed eVDFs during the solar wind expansion. There are two main candidates which can provide some effective mechanisms cons training the overall shape and properties of electron distribution functions. These are the wide family of wave-particle interactions, like kinetic plasma instabilities, and, despite their already described limitations, Coulomb collisions.

In the present study, we show the radial evolution of the model eVDF. Our findings indicate some indirect proofs of scattering mechanisms of strahl electrons into halo tails and also the increasing deviations of eVDF non-thermal tails at larger heliocentric distances. Furthermore, we show that both, kinetic plasma instabilities and Coulomb collisions, impose effective constraints on observed electron temperature anisotropies of the core component and also on the observed overall electron heat flux.

Chapter 1

Solar Wind

Not only is the Sun a source of wide spectrum of electromagnetic radiation including the most familiar one - the visible light - but also outburst its own matter. Every second, one million tonnes of mass is continuously ejected into the interplanetary space. The solar atmosphere is so hot that it can not be held back neither by the pressure of the interstellar medium nor even by the own gravity of the Sun. And it blows out. Due to very high temperatures, about few thousands at the surface of the Sun and even more than one million degrees in the solar corona, the solar atmosphere is almost completely ionized. Yet, the ions and electrons are in overall balance and the gas is therefore electrically neutral as a whole, which we refer to as plasma - the fourth state of matter. This permanent outflow of charged particles from the atmosphere of the Sun that fills the whole heliosphere is what we call the *solar wind*.

1.1 Discovering the Wind from the Sun

Perhaps the first ideas of charged particles streaming away from the Sun appeared in the middle of the nineteenth century. A British astronomer Richard C. Carrington noticed, while observing the sunspots, a sudden outburst of energy from the Sun's atmosphere - a phenomenon what we call today a solar flare. Consequently, a day after, the Earth was hit by a geomagnetic storm. Carrington then correctly suggested a possible connection of the storm event to his observation. The conclusions of Carrington were than further developed by George Fitzgerald who supposed that intermittent beams of charged particles are accelerated by a power-full electrostatic field of the Sun and are consequently reaching the magnetosphere of the Earth.

At the turn of the century, the Norwegian physicist Kristian Birkeland pushed the concept of sporadic solar streams a little closer to our today's knowledge. At that time, the connection between solar particles, the geomagnetic activity and also the polar auroras was already known and generally accepted. Birkeland, based on his large geomagnetic surveys showing a nearly permanent auroral activity, introduced for the first time a concept of a continuous outflow of charged particles of both kinds, negative electrons and positive ions, emitted from the Sun. However, this idea was first ignored for many years.

As lately as in the 1950s, a German scientist Ludwig Biermann explained the often observed secondary tails of comets, always pointing away from the Sun, by a steady stream of particles emitted from the Sun pushing the comet's tail away, and Birkeland's idea revived again. However, in contrast with Biermann's conclusions, the British mathematician Sydney Chapman concurrently predicted from the kinetic theory of gases an almost static solar atmosphere reaching well beyond the orbit of the Earth. A contradiction to Biermann's suggestions, which had to be explained, arised.

It was Eugen N. Parker, an American solar astrophysicist, who realised the Chapman's model and Biermann's hypothesis to be a result of the same phenomenon - the solar wind. Contrary to Chapman, Parker correctly supposed a large heat flux in the solar corona which results in a very hot solar atmosphere, even at larger distance. Therefore, the thermal pressure of the particles can overcome at a few solar radii the gravity of the Sun and particles escape in a form of a supersonic flow. It was the Parker's theory that laid the foundations of the moder concept of the solar wind physics. The existence of a solar wind was subsequently slowly adopted by the scientific community. Yet the final prove was still missing - direct *in situ* measurements.

It was fortunate that at the same time the space age was beginning and the race between that time Great Powers, the United States and the Soviet Union, rapidly advanced the explorations of the outer space. First ever direct observations and measurements of the solar wind, a strong flow of positive ions streaming through the interplanetary space, were performed in 1959 by the spacecraft Luna 1 and the same year consequently confirmed by enhanced detectors on board Luna 2. However, neither Luna 1 nor Luna 2 could resolve the direction of the impacting stream of particles. The final proof of the solar wind existence was provided three years later by the spacecraft Mariner 2. By its solar plasma spectrometer, it was shown that the interplanetary space is indeed filled by a permanent stream of charged particles continuously flowing outwards from the Sun. Up to now, several tens of different spacecraft have explored the space in our solar system and acquired a substantial amount of data. Today, the solar wind is thus almost fully described, yet, still not fully understood.

1.2 Brief Description

In order to understand the origin of the solar wind we have to examine in the solar corona - a very tenuous and even more hot top layer of the solar atmosphere. The solar corona extends from the chromosphere up to a few tens of solar radii with no definite boundaries. In the transition layer between the chromosphere and the corona the temperature starts to rise rapidly from a few thousands to more than one million Kelvins. Leaving the famous puzzle of the solar coronal heating[1] behind,

[1]From basic principals of thermodynamics, the heat from the corona should be conducted downward to relatively cooler chromosphere and convected at the same time outward in order to maintain the hot corona. A fundamental question arises - how does the Sun heat the corona?

the high temperature in the corona is essential for two reasons. It makes gases in the corona fully ionized and particularly allows the charged particles of the ionized atmosphere to escape the gravity of the Sun. More precisely, the thermal pressure gradient in the solar corona falls off with radial distance slower than the gravitational force and the solar wind can thus blow out. Its velocity reaches several hundreds kilometers per second already at few solar radii from the surface.

The energy transported by the solar wind compared to the total energy output of the Sun represents only a very small fraction, about one millionth that of electromagnetic radiation. However, the solar wind largely determines the conditions within the whole heliosphere and plays an crucial role in the interaction with all the bodies of the solar system. Most of its momentum is carried by positive ions. The solar wind consists largely ($\sim 95\%$) of ionized hydrogen (protons) with a small ($\sim 4\%$) admixture of ionized helium (alpha particles) and of a fractional number of ions of heavier elements. The bulk speed of the protons, as well of the alpha particles which travel even faster, exceeds their thermal velocity indicating both protons and alphas to be supersonic. The total number of positive ions is balanced by equal number of electrons. Both ions and electrons flow together with about the same bulk speed. Electrons, because of their much smaller mass and still comparable temperature to protons, have thermal velocities considerably exceeding the speed of the wind and are therefore subsonic. Furthermore, electrons ensure the local quasi-neutrality and particularly carry the bulk of the solar wind heat flux, as we will see later, one of the crucial quantities driving the solar wind expansion.

1.2.1 Main characteristics of solar wind state

For any kind of gas two parameters are essential to characterize its state - the density and the temperature. For instance, these two quantities further determine the thermal pressure, which in the case of solar wind plays an important role for the solar wind acceleration. From indirect measurements the density of both protons and electrons in the corona is estimated to be about $10^{14}\ m^{-3}$. Assuming a purely radial expansion with a constant speed of the flow, the conservation of mass implies the total mass flux Φ_m through a sphere of a radius r to be constant ($\Phi_m = 4\pi r^2 n v = const$). Therefore, the density n of the solar wind in such conditions should fall off as $n \propto r^{-2}$. This theoretical radial profile is indeed in fair agreement with observations. *In situ* measurements near 1 AU, i.e., in the proximity of the Earth, show a typical density of about 5-10 protons/electrons per cubic centimeter.

The radial evolution is more complex in the case of the solar wind temperature. From the million-degree corona the temperature falls only to about $10^5\ K$ near 1 AU. For an ideal gas (thus $p = nk_BT$) expanding as a polytrope flow, i.e., with the pressure proportional to the density as $p \propto n^\gamma$, the exponential decrease of the temperature with radial distance is given by $T \propto r^{2(1-\gamma)}$. If there were neither sources nor dissipation of energy, the expansion would be purely adiabatic ($\gamma = 5/3$) and the temperature should decrease as $T \propto r^{-4/3}$. However, the adiabatic approach

Understanding the source of the coronal heating still remains as one of the most striking phenomena of the solar physics.

is not valid neither for electrons nor for protons indicating heating mechanisms to be present during the solar wind expansion. Furthermore, the general power law $T \propto r^{-\alpha}$ is observed to be variable with other solar wind properties. From many observations the α exponent for protons was estimated to lie approximately between 0.9 and 1.4, thus still quiet close to the adiabatic case. By contrast, electrons are observed with α covering almost a full range between the adiabatic and isothermal limits with typical values ranging from 0.4 to 0.8 (see a summarizing Figure 1.1).

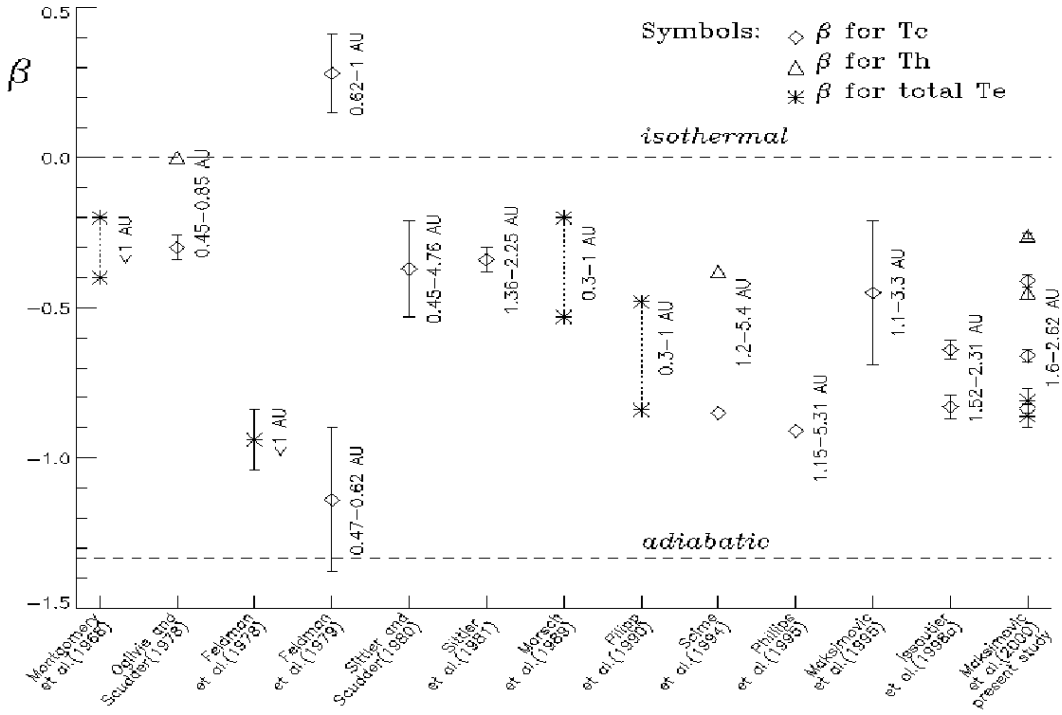

Figure 1.1: (*Maksimovic* (2009), private communication) Temperature gradients of solar wind electrons were already subjected during the several last decades to many observational studies. Obviously, there is no single value of the β exponent of the temperature power law $T \propto r^{-\beta}$. In fact, observations fill almost the whole range between the adiabatic and isothermal limits.

We already have an overview about the densities and temperatures prevailing in solar wind plasmas. Now, another question naturally arises. What is the actual speed of the solar wind? In fact there is more than one correct answer. Early space missions, all of them with nearly in-ecliptic trajectories, revealed that the solar wind speed can be as slow as about 200 km/s while also fast streams were observed with velocities greater than 750 km/s. The origin and topology of this variable velocity pattern of slow and fast streams was finally clarified by the mission Ulysses. The Ulysses spacecraft was launched in 1990 and it was the first space mission with an out-ecliptic trajectory passing over the poles of the Sun. All prior observations had been made at or near the solar system's ecliptic plane. The most important

discovery of Ulysses is summarized in Figure 1.2. The polar diagram shows the solar wind velocity as a function of the heliographic latitude for two pole-to-pole passages from years 1995-1996 and 2000-2001. These two periods correspond to the seasons of minimum and maximum solar activity respectively. The left panel of Figure 1.2 (solar minimum) clearly shows two different regimes of the solar wind. First, fast streams are observed in the inactive dark coronal holes located at higher solar latitudes up to the poles. Here the open magnetic field lines extend almost radially outward the surface of the Sun. The charged particles, which follow the magnetic field lines, can thus easily escape. In contrast a more variable slow wind is observed around the equatorial plane. These slow streams originate from the edges of temporarily open streamers or from opening loops and active regions of the Sun's magnetic field. Obviously the situation dramatically changes when the solar activity reaches its maximum during which the Sun's magnetic dipole is highly distorted. The magnetic topology in the corona becomes much more complex and the alternating fast and slow streams are observed at all latitudes.

In addition, as a third solar wind regime are usually consider the transient flows. These are associated with episodic solar events produced by solar eruptions referred to as coronal mass ejections (CME). CMEs disrupt closed magnetic field lines above the solar surface and, depending on the energy released, can have low as well as very high speeds. The occurrence of CMEs is prevailing during the maximum of the solar cycle.

1.2.2 Interplanetary Magnetic Field

The magnetic field of the Sun is composed of localized strong magnetic structures in the photosphere with typical intensity of $10^{-1}\ T$ that are superimposed on a much weaker global dipolar field with an intensity of about $10^{-4}\ T$. The effect of localized non-dipolar components becomes smaller with increasing heliocentric distance. A dipole would be thus a reasonable approximation far away from the Sun. However, the global structure of the interplanetary magnetic field (IMF) is more complex.

The high conductivity of solar wind plasmas results in magnetic Reynolds numbers[2] much greater than unity. Therefore, the expanding solar wind causes the magnetic field lines to move with away from the Sun - we call the magnetic field to be frozen into the moving plasma. Furthermore, since the Sun is rotating with respect to the radially expanding solar wind, magnetic field lines, anchored to their source location, are bent and form the so-called *Parker's spiral* (see the left panel of Figure 1.3). The IMF can be thus considered as radial only up to a limited distance. The inclination of the magnetic field lines in the equatorial plane to the radial direction is already about 45° at 1 AU and is nearly perpendicular beyond 10 AU. The radial expansion together with conservation of the magnetic flux then yield the magnetic intensity to decrease as $B \propto r^{-2}$ with heliocentric distance. About 1 AU from the Sun the magnetic field has a strength of approximately 5-10 nT.

[2]The magnetic Reynolds number describes the ratio between the magnetic diffusion, produced by conductive losses, and the convection due the plasma motion. It represents an analogy to Reynolds number for classical fluids which quantities the effect of viscosity.

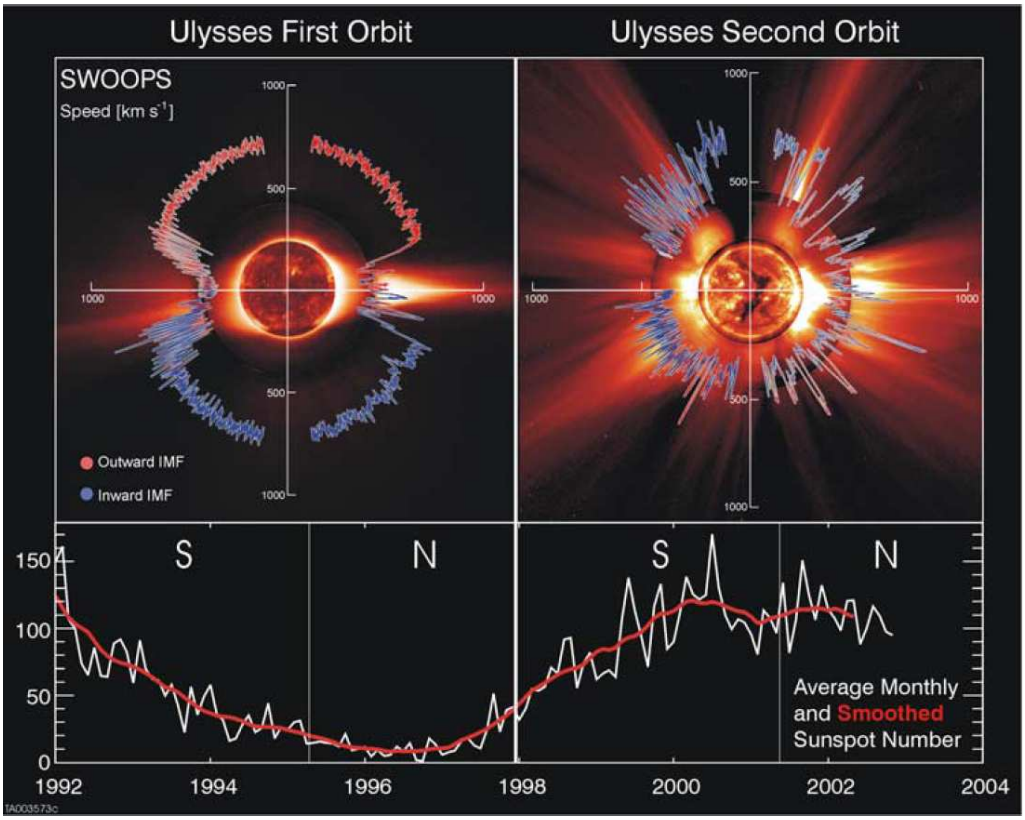

Figure 1.2: (From *McComas* (2003)) Polar diagram of the solar wind speed as measured by the Ulysses spacecraft within the first two pole-to-pole passes. The two displayed orbits correspond to the solar minimum (left panel) and solar maximum (right panel) respectively. During low solar activity a regular pattern is found with fast streams at higher latitudes and variable slow streams around the equatorial plane. The pattern of slow and fast streams is more complex in the case when solar activity reached its maximum.

In order to complete the simplified picture of the IMF, we have to introduce another important structure called the *heliospheric current sheet* (Figure 1.3, right panel). With respect to the approximately dipolar structure of the IMF close to the Sun, the sense of the solar magnetic field lines is opposite in both hemispheres. From the Ampere's law, an electric current thus flows in a thin layer near the equatorial plane where the magnetic field reverse its orientation. The magnetic dipole is not exactly parallel to the solar rotation axis and the magnetic equator thus has a small tilt angle with the solar equatorial plane. As a result, the heliospheric current sheet, being drawn by the solar wind outward from the rotating Sun, is warped and takes a wavy spiral form. An observer in the equatorial plane thus sees four magnetic sectors with alternating positive and negative polarity of the IMF.

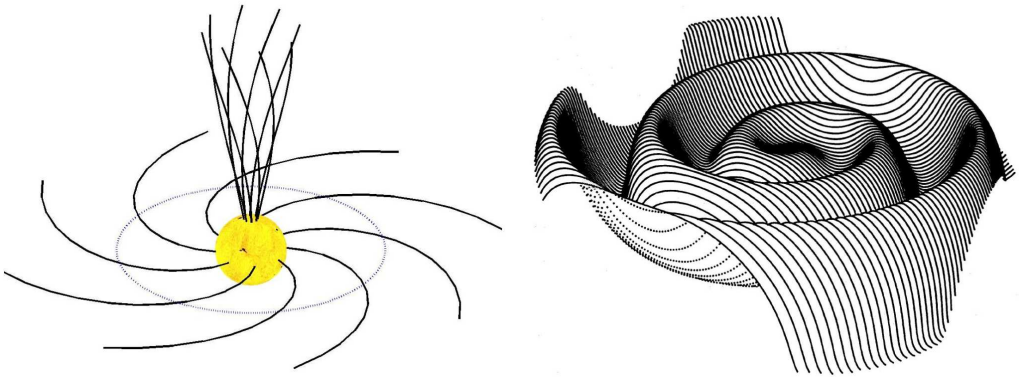

Figure 1.3: Left panel: The magnetic field lines frozen into the radially expanding solar wind are bent due to the rotation of the Sun into to so-called Parker's spiral. Right panel (adopted from *Jokipii and Thomas* (1981)): The heliospheric current sheet, a thin current layer where the magnetic field reverse its polarity, is deformed into a wavy plane. Its intersection with the equatorial plane defines four magnetic sectors with the magnetic sense alternating from sunward to antisunward direction.

1.3 Basic Solar Wind Physics

Addressing the solar wind phenomenon from basic principles introduces several difficulties. The state of a mechanical system is defined by the position and velocity of all particles at a given time. We could then exactly determine the evolution of the system by solving equations of motion for all the individual particles. The solar wind represents a many-body system of charged particles. These particles feel not only the gravity but particularly the present electromagnetic fields through the effect of the Coulomb and Lorentz forces. Moreover, each charged particle generates its own field and concurrently reacts with microscopic fields of all other particles. The actual electromagnetic field is thus a sum over all particle-generated microscopic fields and the external ones. Hence, we have to deal with a very complex and self-consistent physical system. Obviously, with still more than 10^6 particles per m^3 at 1 AU, the classical mechanical descriptions requires enormous computational capacity that substantially overcomes even the fastest computers available. In order to decrease the level of complexity of our problem, descriptions of statistical nature are required. However, note that by decreasing the original number of variables, the statistical approaches can provide approximate solutions only.

The closest statistical approach to our problem is the so-called *kinetic plasma theory*. The state of the system is defined by the velocity distribution functions (VDFs) of all particle species that give the probable number density of particles with certain velocity at a given position and time. The full set of the equations of motion is then replaced by corresponding equations determining the evolution of the VDFs. In the absence of collisions, the equation for the velocity distribution

function f_i, called the *Vlasov equation*, for one single specie i reads as

$$\frac{\partial f_i}{\partial t} + \mathbf{v} \cdot \nabla_{\mathbf{x}} f_i + \frac{q_j}{m_j} (\mathbf{E} + \mathbf{v} \times \mathbf{B}) \cdot \nabla_{\mathbf{v}} f_i = 0 \tag{1.1}$$

where $\mathbf{E}$ and $\mathbf{B}$ are the electric and magnetic fields acting on particles of charge q_i and mass m_i. The Vlasov equation simply tells that a collisionless plasma behaves as an incompressible fluid. When collisions become important, a non-zero differential term of f_i appears on the right-hand side of eq. 1.1. In plasmas where collisions act through the Coulomb force, this yields the *Fokker-Planck equation*. Similarly, if gravity or other forces acting on the particles are not negligible a corresponding term has to be added to the left side of the Vlasov equation. As the closest approach, the kinetic theory still retains some of properties of individual particles. On the other hand it leads to tractable solutions only in some simple geometries.

A next step further in the statistical process of averaging is the fluid description. If we deal with electrically charged fluids subjected to present magnetic fields, the fluid theory for magnetized plasmas is called the *magnetohydrodynamics* (MHD). The fluid approximation assumes the plasma to be treated by examining only the behavior of several first moments of the velocity distributions. The basic moments typically involved in the MHD approach, i.e., the density n, the bulk speed $\mathbf{v}_b$ the temperature T, the pressure tensor $\mathbf{P}$ and the heat flux vector $\mathbf{Q}$, are defined by the distribution function $f(\mathbf{v})$ as

$$n = \int f(\mathbf{v}) d^3\mathbf{v}, \tag{1.2}$$

$$\mathbf{v}_b = \frac{1}{n} \int \mathbf{v} f(\mathbf{v}) d^3\mathbf{v}, \tag{1.3}$$

$$T = \frac{m}{3nk_B} \int |\mathbf{v} - \mathbf{v}_b|^2 f(\mathbf{v}) d^3\mathbf{v}, \tag{1.4}$$

$$\mathbf{P} = m \int (\mathbf{v} - \mathbf{v}_b) \cdot (\mathbf{v} - \mathbf{v}_b) f(\mathbf{v}) d^3\mathbf{v}, \tag{1.5}$$

$$\mathbf{Q} = \frac{m}{2} \int (\mathbf{v} - \mathbf{v}_b) |\mathbf{v} - \mathbf{v}_b|^2 f(\mathbf{v}) d^3\mathbf{v}. \tag{1.6}$$

The MHD approach thus significantly decrease the number of the variables, from an infinity number of parameters, in general needed to describe the whole VDF, to a more reasonable finite number. However, we are loosing the chance to handle the microscopic, sometimes very important processes produced by individual particles. The most general approach of the MHD is the *multi-fluid theory* treating all particle species as individual conducting fluids. The evolution equations for the macroscopic quantities are derived from appropriate moments of the Vlasov equation. The zero-order moment for the ith specie of plasma particles gives the continuity equation

$$\frac{\partial n_i}{\partial t} + \nabla \cdot (n_i \mathbf{v}_{b,i}) = 0. \tag{1.7}$$

Analogically the moment of the first order of the Vlasov equation gives the evolution

equation for the bulk speed of the fluid, i.e., the fluid equation of motion

$$\frac{\partial \mathbf{v}_{b,i}}{\partial t} + (\mathbf{v}_{b,i} \cdot \nabla)\mathbf{v}_{b,i} + \frac{1}{\rho_i}\nabla \mathbf{P}_i - \frac{q_i}{m_i}\left(\mathbf{E} + \mathbf{v}_{b,i} \times \mathbf{B}\right) = 0 \tag{1.8}$$

In the continuity equation, the evolution of the density depends on the fluid velocity. Equally in the equation of motion the velocity of the fluid evolves under the influence of the pressure tensor. Repeating the same procedure and calculating the next moment of the Vlasov equation, we will find that in the resulting equation of energy conservation the pressure depends on the heat flux. Generally each moment of the Vlasov equation in the MHD plasma description requires on order higher moment of the distribution function to be known. The major problem encountered by the MHD approach is the fact that it is fully valid only if the studied distributions can be defined by a finite set of their moments. Otherwise the infinite set of MHD equations has to be truncated by some assumption on the highest order moments of the VDF. This closure in fluid treatments is often arbitrary and based on analogies with ideal gases that may not always apply.

In a collisional gas in thermodynamic equilibrium, the phase space distribution tends toward a Maxwellian distribution. Maxwellians have special properties that make them simple to use. The Maxwellian distribution is fully described by only two parameters, namely the density and the temperature. The simplicity of this model enables one to study the fluid evolution analytically. The MHD approach is thus for this case highly developed. But plasmas are not always Maxwellian. One must be therefore very careful about applying theories or equations that may implicitly assume Maxwellian behavior. Some processes, like collisions, are strongly required to ensure the local thermodynamic equilibrium, and thus a Maxwellian distribution. As we will see later, this is hardly achievable in plasmas like the solar wind. Therefore, there is controversy as to whether the solar wind can be treated as a Maxwellian or not and even whether fluid theory can be applied.

In the equations of the kinetic plasma theory as well as of the MHD approach electric and magnetic field are included acting on the charged particles and fluid elements respectively. As the system evolves the corresponding sets of equations have to be completed by the set of equations describing the evolution of the fields. This set of equation describing the properties of the electric and magnetic fields and relating them to their sources, charges and electric currents, is represented by the four Maxwell's equations

$$\nabla \cdot \mathbf{E} = \frac{1}{\epsilon_0}\sum_i n_i q_i, \tag{1.9}$$

$$\nabla \cdot \mathbf{B} = 0, \tag{1.10}$$

$$\nabla \times \mathbf{E} = -\frac{\partial \mathbf{B}}{\partial t}, \tag{1.11}$$

$$\nabla \times \mathbf{B} = \mu_0 \sum_i n_i q_i \mathbf{v}_{b,i} + \frac{1}{c^2}\frac{\partial \mathbf{E}}{\partial t} \tag{1.12}$$

The full set of equations either of the kinetic or MHD description provides, if applied correctly, a powerful tool to examine the solar wind plasmas. However, this

system of integro-differential equations is very difficult to solve. Very often, some analytical or even numerical solutions are obtained under simplifying assumptions or approximate descriptions of the original problems.

1.4 Solar Wind Solution

The principal question of the solar wind physics is also the most problematic one. How does the solar wind blow out into the interplanetary space? From the brief introduction we know that the basic power providing the acceleration to the solar atmosphere is the very high temperature in the corona. However, the situation is much more complex as we will see even from the simplest theoretical approach. For its simplicity, we will start with the one-fluid description as it was done by E. N. Parker in the first classical theory of the solar wind expansion.

1.4.1 Fluid description

For a time stationary state ($\partial/\partial t = 0$) and an incompressible fluid, the integration of the equation of motion results in the Bernoulli's theorem describing the equilibrium between the pressure of the fluid and external forces. Neglecting the effect of electromagnetic fields, the Bernoulli's theorem for the solar atmosphere reads as

$$w = \frac{v^2}{2} + \int \frac{1}{\rho} dp - \frac{M_S G}{r} = constant. \tag{1.13}$$

where w is the energy per unit mass, v, ρ and p are the speed, mass density and pressure of the fluid respectively and the negative term in (1.13) expresses the gravitational energy of the Sun. For any polytrope flow, the pressure p is related to the mass density ρ as $p \propto \rho^\gamma$ with $1 \leq \gamma \leq 5/3$. Let us first examine the upper limit, i.e., the adiabatic case ($\gamma = 5/3$). Substituting the law of a perfect gas $p = \rho k_B T/m$ into (1.13) we have

$$w = \frac{v^2}{2} + \frac{5}{2}\frac{k_B T}{m} - \frac{M_S G}{r}. \tag{1.14}$$

Now inserting values typically observed at the base of the solar corona we find that w is negative. The adiabatic flow is to weak to escape the gravity of the Sun and we end without any wind. The opposite limit of the polytrope relation is the isothermal flow ($\gamma = 1$). In this case the Bernoulli's equation gives

$$w = \frac{v^2}{2} + \frac{k_B T}{m} \ln \rho - \frac{M_S G}{r}. \tag{1.15}$$

Substituting again the values typical for coronal plasmas we find that the isothermal flow is able to produce a wind since w is now positive.

Replacing ρ in (1.15) from the conservation of mass in radially expanding atmosphere and taking the derivative with respect to r yields

$$\frac{1}{v}\frac{dv}{dr}\left(\frac{v^2}{c_s^2} - 1\right) = \frac{2}{r}\left(1 - \frac{r_c}{r}\right) \tag{1.16}$$

where $c_s = \sqrt{k_B T/m}$ is the isothermal sound speed and $r_c = M_S G/2c_s^2$ is a critical radial distance for which the right hand side of (1.16) vanishes. From (1.16) we can find a solution of v as a function of r. In general, there are five types of solutions from which only three are relevant for a possible solar wind, see Figure 1.4. Furthermore, from these three solutions, only one is stable to produce an outwards expanding solar atmosphere similar to what we observer. It is the *transonic solar wind* solution. The transonic wind starts to accelerate from a low speed in the corona, crosses the sound speed at the critical distance r_c and further increases its velocity to infinity with increasing radial distance.

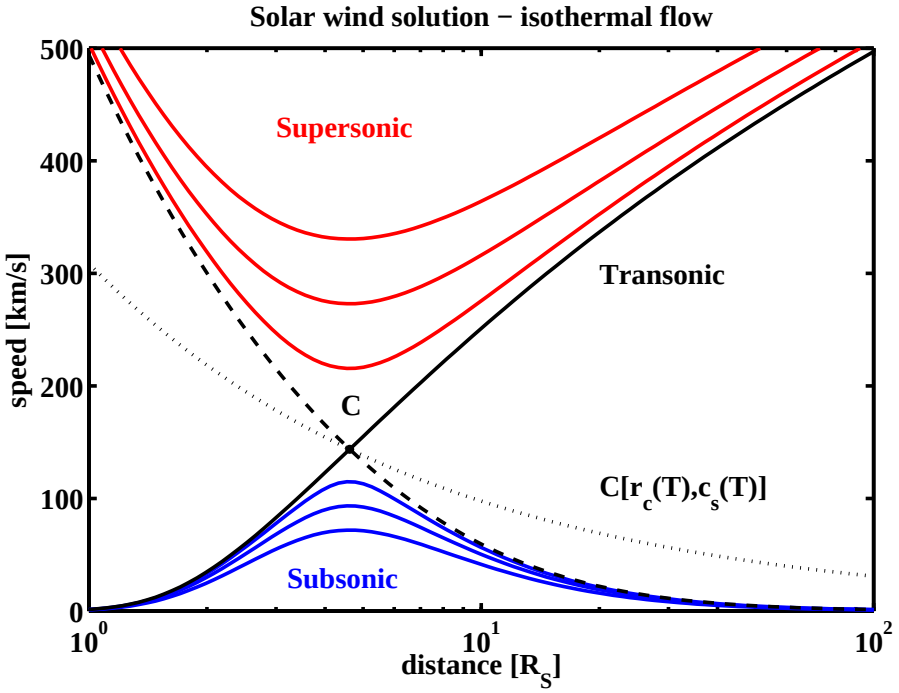

Figure 1.4: There are three types of solutions of the isothermal solar atmosphere possibly producing a wind: subsonic (blue), supersonic (red) and transonic (black). However, only the transonic solution produce a stable outflow, thus a solar wind. The transonic wind starts with a subsonic velocity and continuously accelerates crossing a critical point C at a critical distance r_c with the the sound speed c_s. The position of the critical point is displayed (dotted line) as a function of the initial temperature.

We have shown that the isothermal flow can produce a solar wind. However, note that is represents an unphysical approach. In order to keep a constant temperature along the radial expansion, it requires an infinite source of energy as well as an infinite heat flux to transport this energy from the source to the whole space. Consequently the isothermal wind therefore also results into the infinite terminal speed.

Consider now the general polytrope law with $1 < \gamma < 5/3$ excluding the two limit cases. Contrary to the isothermal expansion, the temperature now decreases

with increasing heliocentric distance but the cooling of the flow is not so fast as in the adiabatic case. Namely for a stationary radial expansion (i.e., $\rho v r^2 = constant$) the radial profile of the temperature is given by

$$T \propto r^{-2(\gamma-1)} \tag{1.17}$$

The heat flux needed to slow down the adiabatic cooling has to be therefore subjoined to the overall energy balanced given by (1.14). Neglecting the radiation, the necessary heat can be conducted by the motion of individual particles in the frame where the plasma is at rest. The total heat carried by the flow has thus two components, the energy transported by the flow and the heat flux Q produced by the heat conduction. In the absence of additional heating, the total energy crossing a sphere of radius r is conserved and is equal to

$$W = 4\pi r^2(\rho v w + Q) = constant \tag{1.18}$$

Using (1.18), we can rewrite (1.14) as

$$\frac{v^2}{2} + \frac{5}{2}\frac{k_B T}{m} - \frac{M_S G}{r} + \frac{Q}{\rho v} = constant. \tag{1.19}$$

From (1.19), we can make an estimation of the heat flux Q_0 required at the base to accelerate the solar wind. In order to reach flow speeds at large distance equal to those observed, the heat flux Q_0 has to be at least about 70 Wm^{-2} or greater. The classical heat flux (*Spitzer and Härm* (1953)) derived in the fluid theory is based on the effect of frequent particle collisions. For an electron gas it can be written as

$$Q_{e,col} = -\kappa_e \nabla T_e(r), \tag{1.20}$$

where κ_e is the electron heat conductivity approximately given by (*Huba* (2007))

$$\kappa_e \doteq 3.2\frac{n k_B T_e}{m_e \nu_{ee}} \tag{1.21}$$

where ν_{ee} is the electron-electron collisional frequency. In the region of solar wind acceleration (1.20) can be approximated as (*Meyer-Vernet* (2007))

$$Q_{col} \doteq 2.86 \cdot 10^{10}\frac{T_e^{7/2}}{r}, \tag{1.22}$$

which for the observed conditions gives only about 17 Wm^{-2}, a value much smaller than the required one.

The present simple model of the solar wind expansion can be further improved and developed, e.g., by introducing multi-fluid description. However, the most important conclusion won't change too much. In order to produce a supersonic solar wind far away from the Sun, a sufficiently large heat flux, or an equivalent source of energy, must exist in the acceleration region. The theoretical heat flux derived for a collisional environment is not powerful enough to provide the required amount of

energy. There are two ways which could possibly solve this discrepancy. One could try to find some other processes heating the particles, the main ideas are based on wave-particle interactions, or rather try to define correctly the real heat flux for the solar wind environment. Furthermore, one should remind that the fluid approach is developed on the basic assumption of all particle species having Maxwellian distributions. In the solar wind, the observed VDFs for both ions and electrons show many non-Maxwellian features. Out of the thermal equilibrium, the proper derivation of the heat flux has to take into account the effect of individual particles, at least statistically in the form of VDFs. From the basic principals, purely collisional fluid models cannot be employed to model the observed VDF since they do not, by definition, handle the non-Maxwellian suprathermal tails. Therefore, the key issue of the solar wind acceleration can not be properly addressed by any MHD models. In order to better understand the solar wind nature, a kinetic description has to be employed.

1.4.2 Kinetic description

The weakly collisional and turbulent plasmas in the solar wind represent a complex problem which rather requires a kinetic treatment, i.e., a description of processes and mechanism produced by individual plasma particles. Solving the problem of solar wind heat flux correctly, all the particle species, including electrons, have to be treated separately. Since protons and other ions are relatively heavy and slow, electrons having much higher thermal speeds are the main candidate to provide transport of a substantial amount of the heat in the solar wind.

The electrons, thanks to their very small mass, can easily escape from the gravitational attraction of the Sun. They thus tend to displace the charge which sets up an outward oriented interplanetary electric field. As a consequence, the electric field serves to balance the higher electron thermal pressure and accelerates the positive ions. From the kinetic point of view, it is the electric field that drives the solar wind expansion and drags the ions away against the gravity of the Sun. With gravity being negligible for the electrons, the electric potential Φ_E can be estimated from the energy balance equation as

$$e\Phi_E \approx \frac{5}{2}k_B T_e + \frac{Q_e}{n_e v} \tag{1.23}$$

It is not a big surprise that the electric potential as a function of the radial distance $\Phi_E(r)$ depends on the electron temperature T_e and the electron heat flux Q_e.

In the absence of collisions, only electrons with speeds greater than the local escape velocity

$$v_E = \sqrt{2e\Phi_E(r)/m_e} \tag{1.24}$$

can reach higher heliocentric distances. Otherwise, they are trapped by the potential barrier. This simple idea of a velocity filtration effect applied on electron velocity distribution functions (eVDFs) represents the basic concept of the exospheric kinetic models. Within the exospheric approach, the particle VDFs are given at the base

of the corona and then, according to the Liouville's theorem and to the Vlasov or Fokker-Planck equation, they are determined everywhere in the whole heliosphere.

The simplest exospheric approaches completely neglect collisions (*Lemaire and Scherer* (1971), *Maksimovic et al.* (1997a), *Lamy et al.* (2003), *Zouganelis et al.* (2004)). In these models the final eVDF shape results only from velocity filtration by the interplanetary ambipolar electric field. While these exospheric models can explain the acceleration of the fast solar wind if non-thermal eVDFs are already present in the corona (*Scudder* (1992), *Maksimovic et al.* (1997a), *Zouganelis et al.* (2004)), they fail in predicting the precise eVDF shape in the heliosphere. Indeed, in these models there are no electrons above the local escape velocity in the sunward direction and the eVDFs are therefore truncated (*Maksimovic et al.* (2001)). This is in contradiction with observations even at 0.3 AU.

Some improvements to the exospheric approach can be achieved by including the effect of Coulomb collisions. *Lie-Svendsen et al.* (1997) solved the Boltzmann equation with the Fokker-Planck approximation of the collision operator for test particles expanding in a background Maxwellian plasma. Starting their modelization at the base of the corona, these authors produced a skewed eVDF at 0.3 AU qualitatively similar to the observed eVDF shapes. However the suprathermal tails were completely absent in this model. *Pierrard et al.* (1999, 2001) adopted this model with a few modifications. Firstly, they used typical eVDF measured *in situ* at 1 AU as boundary condition instead of a Maxwellian deep in the corona (as it was done in *Lie-Svendsen et al.* (1997)) where no detailed observation of eVDFs are available. Secondly, the eVDFs used for the background electrons were more general Lorentzian functions (see *Pierrard and Lemaire* (1996), *Maksimovic et al.* (1997b)) instead of Maxwellians. Within this scenario, which only includes the effect of Coulomb collisions, the authors concluded that non-thermal tails, much less important than at 1 AU, must already be present in the corona in order to explain the observations and that the sunward part, truncated in the collisionless approach, is present in the inner heliosphere only if it is imposed as a boundary condition at 1 AU.

Although the exospheric models provide an improved description of the solar wind expansion, they still have some limitations predicting the observed characteristics of solar wind plasmas. Above all, their results are highly depend on imposed boundary conditions in the regions which are critical for the solar wind acceleration. Mainly the acceleration of the solar wind is achieved assuming sufficiently strong suprathermal eVDF tails. The heating problem is thus only circumvented, since again, the existence of the increased number of high-energetic electrons has to be explained by some heating or accelerating mechanisms. Unfortunately, until now we do not have any real detailed *in situ* measurements in the solar corona that could set the boundary conditions for the exospheric models. The problem of the solar wind acceleration remains therefore still open.

1.5 Particle Distribution Functions in the Solar Wind

Techniques to measure different plasma characteristics, and their spatial and temporal variation, are based on a wide variety of physical principles. In order to fully describe and examine the local conditions and state of the solar wind plasma one needs to perform basically two kinds of diagnostics, namely to probe electromagnetic fields and to detect and analyse surrounding particles. The electric and magnetic fields are measured by search-coils and flux-gate magnetometers and different electric antennas which return the intensity of the fields as well as their fluctuations, i.e., the electromagnetic wave activity. Regarding the solar wind particles, we measure their composition (particle detectors) and particularly distributions of the individual species in the velocity phase-space (energy analyzers).

Although the phase-space distribution function is central to a theoretical interpretation of the behaviour of collections of particles, it is measured only indirectly. The energy analyzers acquire counts versus energy per charge and provide thereby the differential directional flux of particles within a range of solid angles and within an energy band of a given width. Knowing the exact geometry of the detector and the method of measurement the acquired counts can be consequently transformed into velocity distribution functions. Most solar wind instruments flown to date were 1-D or 2-D detectors. In the case of of spinning spacecraft one can thus acquire 2-D or full 3-D distributions respectively. Since charged particle distributions are usually cylindrically symmetric around the magnetic field (gyrotropic), knowing the 2-D angular distributions displaying the flux parallel and perpendicular to the magnetic field is usually sufficient to study most of the important properties.

Coulomb collisions are the basic driving mechanism which maintains a plasma locally in the thermodynamic equilibrium. In the solar wind where the plasma is hot and tenuous the effect of Coulomb collisions is limited. Moreover, as the mean free path (m.f.p.) between two collisions rapidly increases with particle velocity ($m.f.p. \propto v^4$), the Coulomb collisions above a certain energy are almost negligible and the particle velocity distribution functions develop high-energy non-thermal tails. Consequently, significant deviations from an isotropic Maxwellian distribution may occur in the particle velocity phase space.

In situ measurements of solar wind VDFs are already carried out about more than four decades and, indeed, the VDF deviations from thermodynamic equilibrium have been observed by many space instruments for both electrons and protons of the solar wind plasma. In addition to high-energy non-Maxwellian tails, the observed VDFs are often misshapen by occurrence of various beams or asymmetric distortions. It is also the topology of the IMF that has an influence on the shape of solar wind VDFs. While charged particles can freely flow along the field lines, their motion in the perpendicular direction to the magnetic field is highly limited. As a result of this, VDFs in the solar wind may develop different effective kinetic temperatures in the parallel and perpendicular direction with respect to ambient magnetic field and the VDF shape in the parallel direction can exhibit more complex structures.

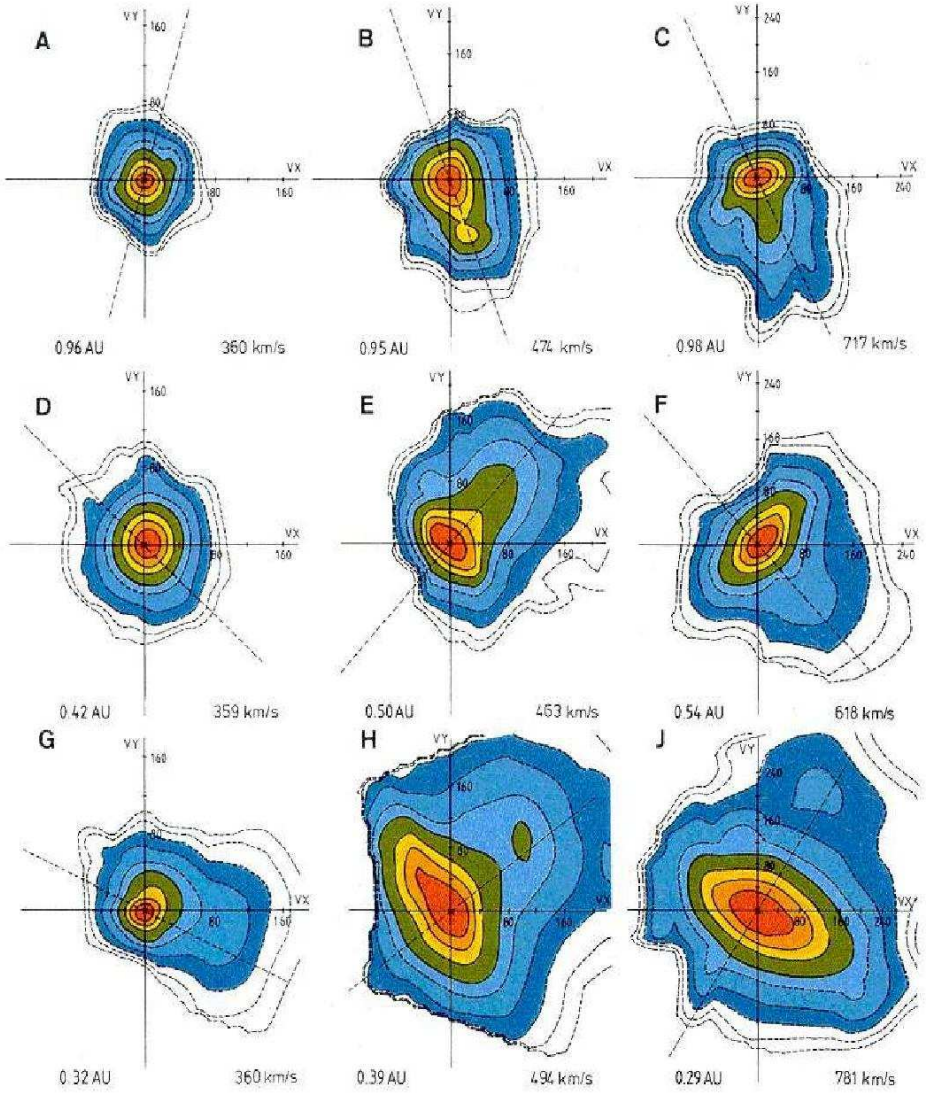

Figure 1.5: (From *Marsch et al.* (1982)) Proton VDFs observed by Helios spacecraft at different radial distances and under different solar wind bulk speeds (as indicated below each plot). The measured VDFs are shown as isodensity contours of 2-D cuts in the velocity phase space. The dotted line represents the direction of the local magnetic field.

We describe here the basic characteristics of the observed VDFs of all main solar wind species, namely the protons, alpha particles and electrons. We keep the description of the ion species very brief and focus mainly on the solar wind electrons which represents the main topic of the current study. In the second part of this chapter we provide a detail description of our data set. The data set, including measured electron VDF from several spacecraft, is used for the statistical analysis on which we base all our conclusions.

1.5.1 Ion Distribution Functions

Thermal velocities of solar wind ions are much smaller than the mean bulk speed of the solar wind. Therefore, the ions behave as a supersonic flow. Due to their relatively large mass, the ions carry the majority of the solar wind momentum. In the solar wind, protons dominates over all other ions representing more than 95% of the total ion number density. The shape of measured proton VDFs can range from almost Maxwellian to highly non-thermal one. Figure 1.5 shows a representative set of proton VDFs acquired under various conditions by the Helios spacecraft. Two main features typical for solar wind observations are clearly visible. Firstly the proton VDFs exhibit considerably large temperature anisotropies. The observed temperature ratios of $T_{p,||}/T_{p,\perp}$ or inversely $T_{p,\perp}/T_{p,||}$ can reach values up to ~ 10, here $T_{p,||}$ and $T_{p,\perp}$ are the parallel and perpendicular proton temperature respectively. Secondly, a faster proton population is often present drifting with respect to the core along the magnetic field ($v_{||} > 0$). The drifting proton population sometimes results in a secondary peak as it is observed for example on panels H and J of Figure 1.5.

The second most numerous species of the solar wind ions are the alpha particles (He^{++}). With an abundance of 3-5 per cent they still contribute to the dynamics of the wind. Alpha particles are also the only other specie for which the full 3-D VDFs have been acquired. Observations show alphas to stream faster than protons. The alpha-proton drift can be only a few km/s, however, it can also slightly exceed the local Alfvén velocity. Compared to protons, alpha particles also exhibit greater temperature anisotropies.

As it is already difficult to drag out the heavy ions of helium against the gravitational attraction of the Sun, the heavier ions (e.g. C, O, Ne or Fe) represent only a minor component. Due to their low densities, even the modern spectrometers can usually resolve only their chemical composition and state of ionization.

1.5.2 Electron Distribution Functions

Although the solar wind electrons exhibit some similar features, they behave in a different way than ions do. Because of their small mass with respect to ions ($m_e/m_i \ll 1$) and approximately equal temperatures, their thermal speeds largely exceed the one of the solar wind and the electrons are therefore subsonic. Moreover, electrons at higher energies ($\gtrsim 100\ \ eV$) are able to easily explore the global structure of the whole heliosphere within much shorter time scales.

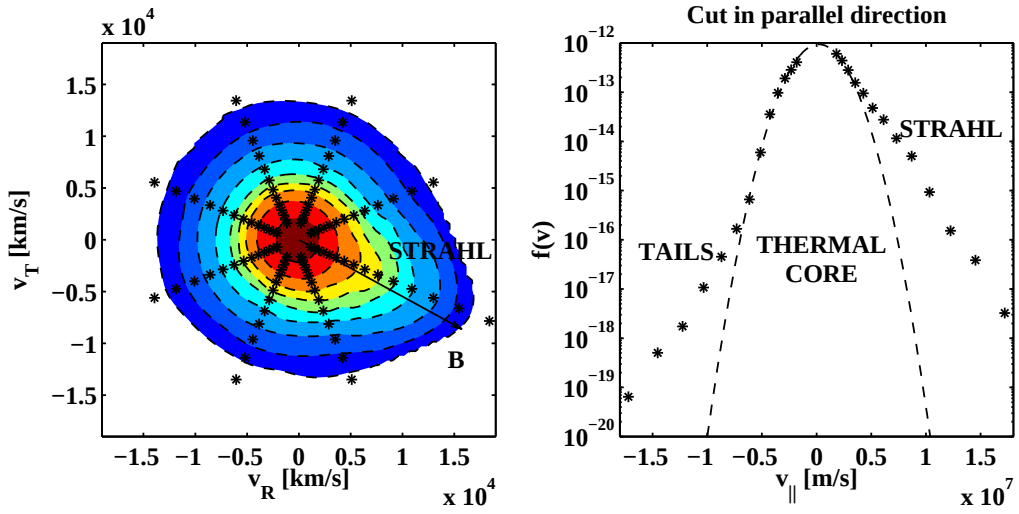

Figure 1.6: Typical electron velocity distribution function as measured by the Helios spacecraft. Left panel: the eVDF is displayed as isodensity contours in the ecliptic plane (v_R and v_T for radial and tangential velocity respectively). The eVDF shows a large skewness along the magnetic field (black arrow) which has been called the strahl. Right panel: The deflections from the Maxwellian distribution (dashed line), namely the halo tails and the strahl, are shown on the parallel eVDF cut along the magnetic field.

Study of the radial evolution of the electron velocity distribution functions (eVDFs) is interesting for several reasons. Electrons play an important role in the solar wind expansion since they ensure the quasineutrality and carry the bulk of the solar wind heat flux (*Feldman et al.* (1975), *Marsch* (2006)). The knowledge of the precise shape of the eVDFs is also fundamental in determining the radial profile of the interplanetary ambipolar electric field which is responsible for the solar wind acceleration in the exospheric models (*Lemaire and Scherer* (1971), *Maksimovic et al.* (1997a, 2001)). Furthermore, some authors suggest (e.g. *Scudder and Olbert* (1979)) that because of the weak collisionality, a lasting influence of the boundary conditions in the transition region or even in the corona can be found on the collisionless suprathermals even far away from the Sun. A detailed description of the non-thermal part of the eVDFs can therefore provide clues to better estimate the solar wind initial conditions and to solve the problem of the solar wind acceleration.

The eVDFs in the solar wind typically exhibit three different components: a core, a halo and a strahl (*Montgomery et al.* (1968), *Feldman et al.* (1975), *Rosenbauer et al.* (1977), *Pilipp et al.* (1987a), *Maksimovic et al.* (2005)). The core represent on average about 95% of the total number density. With a still sufficient effect of collisions, the thermal core electrons are well modeled by a bi-Maxwellian velocity distribution. The non-Maxwellian suprathermal tails consist of two separate parts:

the halo and the strahl. While the halo is present at all pitch angles, the strahl appears as a beam-like population moving predominantly away from the Sun and is highly focused along the ambient magnetic field. Note that some special configurations when the direction of the magnetic field is locally inverted (see e.g. *Crooker et al.* (2004)) may change the strahl propagation. Such observations of sunward moving or even bidirectional strahl electrons have been also reported (see *Gosling et al.* (1987, 1993) for instance). A typical eVDF observed in the ecliptic plane by the Helios spacecraft is shown in Figure 1.6. The non-thermal components of the electron distribution, namely the halo tails and the strahl, are visible in the parallel eVDF cut along the magnetic field (right panel).

From the observational point of view, the solar wind eVDFs were originally studied in detail by *Feldman et al.* (1975). The drift of the non-thermal component of the eVDFs with respect to the thermal core was shown to be in agreement with the zero-current relation, i.e., in average no electric current flows in the rest frame of the solar wind plasma. The non-thermal electrons were also indicated as the main source of the total electron heat flux. Later on, the non-thermal tails were found to be more important in the fast wind than in the slow one (*Rosenbauer et al.* (1977), *Pilipp et al.* (1987a,b)). Alike solar wind ions, electrons also exhibit temperature anisotropies with respect to the direction of the magnetic field, however, the observed values are found much closer to the isotropic state with an average $T_{e,||}/T_{e,\perp} \simeq 1.2$ (*Feldman et al.* (1975) and *Pilipp et al.* (1987b)).

More recently, *Maksimovic et al.* (2005) examined the relative importance of the non-thermal electrons in the fast solar wind as a function of the increasing radial distance from the Sun. The main result obtained by *Maksimovic et al.* (2005) for the fast wind is that the strahl relative density is declining with increasing radial distance, whereas the halo importance increases. These findings, together with those of *McComas et al.* (1992), who showed that the the core relative density remains almost unaffected during the expansion, and those of *Hammond et al.* (1996), who showed that the strahl angular width broadens with increasing radial distance, support the scenario of strahl electrons being scattered into the halo, probably by waves processes (*Vocks et al.* (2005), *Gary and Saito* (2007) and *Saito and Gary* (2007)). However, until now any clear observational evidence of such processes has been reported. In the present work, we extend the *Maksimovic et al.* (2005) study to the slow solar wind case, for the results see chapter 4.

1.6 Plan of the Thesis

There is much about the solar wind that we do not understand as well as we would like to understand. Not only from the theoretical point of view represents the origin of the solar wind and its acceleration still one of the most striking questions of the moder solar physics. Neither the MHD fluid approach nor the exospheric kinetic models give a satisfying answer explaining all the observed features in the solar wind velocity distribution functions of either protons or electrons. The heat transport, mostly driven by the electrons, plays a key role in the solar wind dynamics.

The classical collisional heat flux, based on an assumption of local thermodynamic equilibrium, is shown to be insufficient to power the solar wind acceleration. In fact, the observed eVDFs in the solar wind exhibit many non-Maxwellian features and a correct computation of the heat flux must be performed kinetically. Therefore, a detail description of the solar wind eVDFs and a study of their radial evolution is highly important.

In order to better understand the non-thermal features of observed eVDFs as well as the transport of the heat in the solar wind, we performed a statistical study of a substantial amount of measured eVDFs. All the eVDF samples were acquired in the low ecliptic latitudes covering the heliocentric distance from 0.3 up to 4 AU. All electron parameters are estimated by fitting of measured eVDFs with a model distribution function. For our study, a new model was proposed which, for the first time, describes all three components of the solar wind eVDFs (i.e. the core, the halo and the strahl) analytically. Two main goals of the present work are *(i)* to examine the radial evolution of main eVDF characteristics, i.e., the density, the temperature and the heat flux, with increasing heliocentric distance; and *(ii)* to study the effect of possible mechanism which can provide some additional heating or energy dissipation to solar wind electrons and moderate thus the shape of observed eVDFs during the solar wind expansion.

Two possible candidates of such mechanism that theoretically act as a possible mediator for the transport of energy between individual particles are introduced in chapter 2. Here we present the basic properties of Coulomb collisions and several kinetic plasma instabilities which are relevant for our further analysis. In chapter 3 we describe in detail the new analytical model distribution function and the complete data set of measured eVDF samples on which this model was applied. The observed radial evolution of the eVDFs in the solar wind is studied in chapter 4, where we summarize the results from *Štverák et al.* (2009). Based on results reported in *Štverák et al.* (2008), we examine in chapter 5 from the observational point of view the possible constraints imposed by kinetic instabilities and Coulomb collisions on the electron temperature anisotropy. The properties of the electron heat flux as obtained from our analysis are described in chapter 6. Finally, conclusions from our findings and some perspectives for the future work are given in chapter 7.

Chapter 2

Driving Mechanisms

Without any interactions of charged particles with external fields and forces and between the particles themselves, the overall shape of the velocity distribution function would be preserved in time and space. The only way of modifying VDF properties would be to change the kinetic energy or momentum of individual particles. In a classical neutral gas such mechanisms are, in principle, limited to binary encounters between individual particles (mechanic collisions) and to external forces such as gravity.

The situation is different in plasmas. Firstly, the classical binary collisions are replaced by Coulomb interactions between electrically charged particles. Since the Coulomb force acts on (relatively) large distance, close encounters which result in strong scattering are rather rare. In fact, the trajectories of particles are consecutively deviated by a succession of small interactions. In addition to external forces and heating mechanism common with neutral gases (like caused by gravity or radiation) charged particles particularly feel the effect induced by the presence of electromagnetic fields and their oscillations.

The most important family of processes which cause the exchange between the kinetic energy of charged particles with the energy of electromagnetic oscillations (and thus constrain or modify the VDF evolution) are the wave-particle interactions. Various modes of electromagnetic waves can be present in plasmas. There are modes either propagating or standing with respect to plasma rest frame. If the phase speed or the cyclotron speed of a wave is comparable to the speed of charged particles, they become resonant with each other and can exchange their energy. In the following two sections, we will describe the concept and basic properties of Coulomb collisions and wave-particle interactions in the solar wind plasmas.

2.1 Coulomb Collisions

As for collisions between neutral particles, collisions in plasmas can be characterized by a mean free path l_f between two encounters or equivalently by the collision frequency ν which is given by $\nu = v/l_f$ where v is the speed of the colliding particle. The mean free path, i.e., the mean distance between two consecutive collisions, can

be simply derived as

$$l_f = \frac{1}{n\sigma_{col}} \tag{2.1}$$

where n is the density and σ_{col} the effective cross-section of a single collision. In plasmas, charged particles interact via Coulomb force and effective collision cross-sections are very different from those in neutral gases. A rough estimate of the mean free path can be obtained using the following reasoning. In order to significantly change the momentum of a colliding particle the potential energy of the interaction $(e^2/4\pi\epsilon_0 r)$ with r being the distance of the colliding particles, must be at least comparable with their kinetic energy $(mv^2/2)$. With $\sigma_{col} \sim \pi r^2$ the mean free path given in (2.1) can be expressed as

$$l_f = \frac{4}{n}\left(\frac{\pi\epsilon_0 m v^2}{e^2}\right)^2 \propto \frac{v^4}{n}. \tag{2.2}$$

Thus in plasmas, the mean free path rapidly increases with particle velocity ($\propto v^4$) and consequently fast particles are almost collisionless. Replacing $mv^2/2$ by the average thermal energy $k_B T$ gives

$$l_f \propto T^2/n. \tag{2.3}$$

Relation (2.3) has an important consequence for solar wind plasma which is quite tenuous and still sufficiently hot. At 1 AU with $n \sim 5e6 \;\; m^{-3}$ and $T \sim 1e5 \;\; K$, the average distance between particles is about 5 mm and the mean free path about $l_f \sim 1e8 \;\; km$. The collisions in the solar wind are thus rather rare. Note also that since electrons and protons have roughly the same temperatures and densities their mean free paths are comparable. It is also important that the formula (2.3) gives an estimation of the free path for a particle moving with the mean, i.e., thermal, velocity v_{the}. In fact, Coulomb collisions still become important for the thermal core of the electron population for which $v \lesssim v_{the}$.

The importance of collisions in plasmas can be well evaluated through the *Knudsen number* which is defined as the ratio of the mean free path to the typical scale height of variation of basic parameters of the system such as the density or the temperature. Since the temperature gradient is less known in the solar wind, therefore, the density (n) profile is typically used to compute the scale height as

$$H_n = \left|\frac{d(\ln n)}{dr}\right|^{-1}. \tag{2.4}$$

where the derivation is with respect the the radial heliocentric distance r. For a stationary radial outflow with $n \propto r^{-2}$, the density scale height equals to $H = r/2$. Figure 2.1 shows the resulting radial profile of the Knudsen number ($K_n = l_f/H$) as derived from remote and in situ space observations. While deep in the photosphere the Knudsen number is still smaller than $\sim 10^{-10}$, one can see that $K_n \approx 1$ already in a distance of a few solar radii from the photosphere. In order to keep applicability of the MHD approach we have to guarantee only small deviations from the thermal

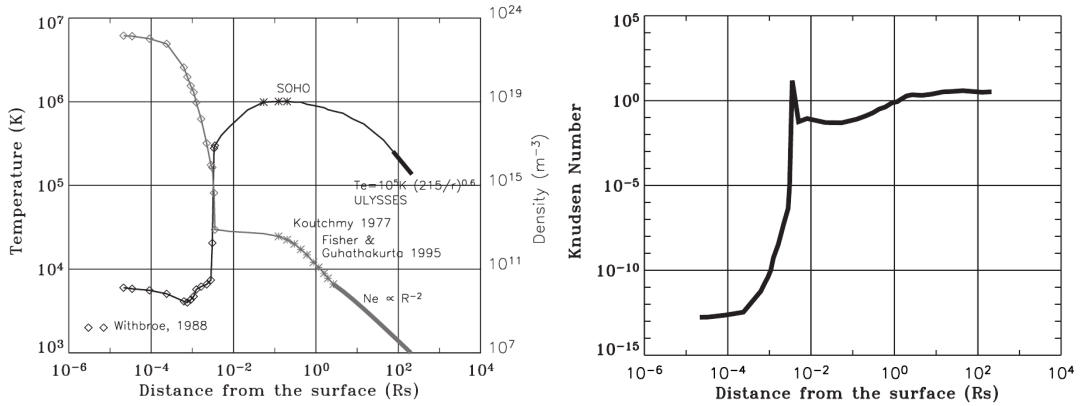

Figure 2.1: (After *Maksimovic* (2007)) Variations of the coronal electron density (light line) and temperature (heavy line) as obtained by interpolating of coronal, SoHo and Ulysses observations (left panel) and the resulting radial profile of the Knudsen number for electrons as a function of the heliocentric radial distance.

equilibrium. To do so we need the length scale of the system to be much greater then the mean free path of the particles ($L \gg l_f$). Figure 2.1 shows that this condition is hardly fulfilled in the solar wind. However, neither collisionless exospheric models are fully appropriate for which the Knudsen number should be much greater than unity ($K_n \gg 1$).

Even though Coulomb collisions in the solar wind are infrequent, some studies suggest that they can still affect and moderate the VDF evolution through the solar wind expansion. Especially for denser and colder plasmas (*Livi et al.* (1986)) the collision frequency is increased and the electron Coulomb collisions can become important. Numerical simulations of *Livi and Marsch* (1987) have shown that already very few collisions may constrain the extreme temperature anisotropies of the exospheric VDFs. It was also shown by *Phillips et al.* (1989) that the electron temperature anisotropy is well correlated with density (see the left panel of Figure 2.2). In denser plasmas the electrons were mostly found closer to the isotropic state indicating a possible effect of collisions. Consequently, *Phillips and Gosling* (1990) have modeled the relaxation of electron temperature anisotropy due to Coulomb collisions and found a good agreement with the previous observations of ISEE 3 spacecraft.

More recently, another and more sophisticated way to compare the effect of Coulomb collisions with the observed electron properties was presented in *Salem et al.* (2003), when used electron collisional age A_e defined as the most probable number of collisions suffered by an electron during the expansion of the solar wind. These results are again in agreement with the expectation that collisionally older plasmas are typically less anisotropic. The collisional age A_e was computed by integration of the frequency of electron collisions over the time of the solar wind expansion. Note however, that this concept does not apply to trapped electrons that circle on closed magnetic field lines (*Bame et al.* (1981) and *Gosling et al.* (1987)).

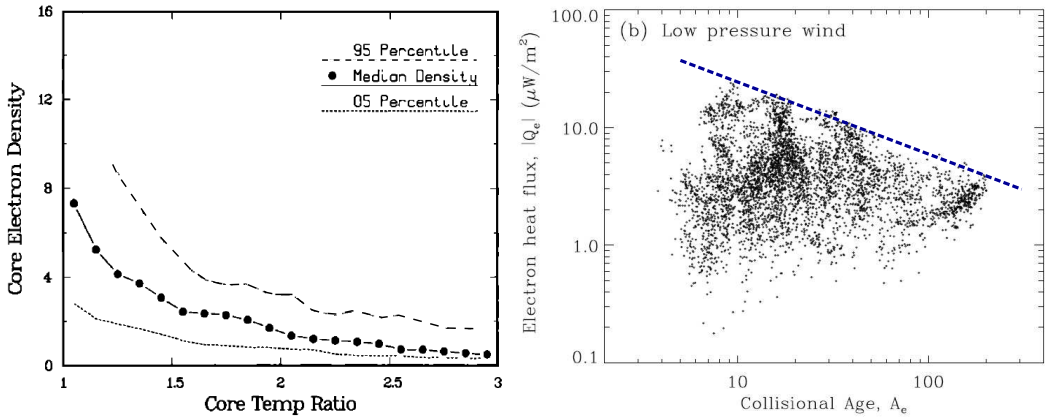

Figure 2.2: (Left panel) On ISEE 3 observations, *Phillips et al.* (1989) has shown a clear correlation between the electron temperature anisotropy and the electron density which may indicate a role of Coulomb collisions. (Right panel) *Salem et al.* (2003) examined the effect of Coulomb collisions on the solar wind heat flux through the collisional age A_e (see text). Observations from WIND spacecraft in the low pressure wind show a net upper bound (blue dashed line) of the electron heat flux which decreases for an increasing collisional age.

Salem et al. (2003) also used the collisional age to examine whether collisions can regulate the solar wind heat flux (see the right panel of Figure 2.2). Their findings show a net upper bound of the electron heat flux which decreases for an increasing collisional age. Moreover, *Salem et al.* (2003) concluded from the WIND observations that the theoretical collisional heat flux derived by *Spitzer and Härm* (1953) can be reached in the solar wind for low Knudsen numbers.

Although the theory predicts the Coulomb collisions to be very rare and thus insufficient to moderate the solar wind eVDFs, the observations indicate an opposite - collisions can not be neglected! We present in chapter 5 some observational evidence of constraints on the electron temperature anisotropy caused by Coulomb collisions (based on results of *Štverák et al.* (2008)). Since our data were acquired at different radial distances from Sun, we have adopted from *Salem et al.* (2003) the concept of collisional age A_e which reflects time evolution of Coulomb collisions in the expanding solar wind. In chapter 6, we further investigate the role of Coulomb collisions on the transport of heat in solar wind plasmas.

2.2 Plasma Waves and Instabilities

Collisions are not the only mechanism shaping observed eVDFs in the solar wind. Another mechanism how charged particles can exchange their kinetic energy is mediated by wave-particle interactions. From the theoretical point of view, they are very effective and are believed to dominate in the solar wind plasmas over Coulomb collisions. The magnetized plasma of the solar wind represents an environment with an ubiquitous activity of many different electromagnetic wave modes. A complete

set of all possible electromagnetic wave modes can be found by solving the system of Vlasov-Maxwell equations. However, this represents a too difficult task and a linear approximation to this system is typically applied. For a particular solution in the form of a planar wave disturbance

$$\delta\mathbf{A}(\mathbf{x},t) = \delta\mathbf{A}(\mathbf{k},\omega)\exp[i(\mathbf{k}\cdot\mathbf{x}-\omega t)], \tag{2.5}$$

we assume the disturbance $\delta\mathbf{A}$ to be much smaller than the undisturbed quantity $\mathbf{A}$. Consequently, all non-linear terms of $\delta\mathbf{A}$ in the Vlasov-Maxwell equations can be neglected. This reduces the original system to a set of linear algebraic equations which determinant $\mathbf{D}$ has to vanish in order to get a non-trivial solution

$$\mathbf{D}(\omega,\mathbf{k},f) = 0. \tag{2.6}$$

Equation (2.6) is called the dispersion relation and provides the dependence of the frequency ω on the wave vector $\mathbf{k}$. The kinetic description of corresponding plasma species enters the Vlasov-Maxwell system through the initial particle VDF (f). Any wave function can be then represented by a superposition of an infinity number of such plane waves.

In plasmas, there are basically two groups of solutions of the general dispersion relation. These are *electrostatic modes* (Langmuir and ion-acoustic waves) and so-called *electromagnetic waves* (whistlers, ion-cyclotron modes, Alfvén waves). A comprehensive list of possible solutions of (2.6) can be found, e.g., in the classical textbook of *Stix* (1992). Here we will focus on some particular solutions of modes which can become unstable (see, e.g., the textbook of *Gary* (1993)).

The concept of linear plasma instabilities arises from an extension of real solutions of the dispersion relation to the complex domain. Assuming complex solution

$$\omega = \omega_r + i\gamma \tag{2.7}$$

of (2.6) has an important consequence on the resulting planar wave. For a non-zero imaginary part of the frequency (γ), the real amplitude of the wave becomes an exponential function of time and the wave is either damped ($\gamma < 0$) or exponentially grows ($\gamma > 0$). Parameter case γ is called the *growth rate* of the unstable mode. Instabilities can arise only if there is some free energy in the plasma which can feed their growing amplitude. Both unstable cases, wave damping and growth, thus require (or result in) an energy exchange with the surroundings.

2.2.1 Wave-particle interactions

A possible source of free energy as well as an energy deposit for the unstable wave modes can be provided directly by solar wind particles. The process of energy exchange caused by waves coupling with the motion of particles is what we call the wave-particle interactions. Taking an average over a sufficient time interval, the mean effect of a fluctuating electromagnetic field on a randomly moving charged particle will be negligible. However, this is not true in some special configurations.

A particle moving in the direction of the wave propagation (along the wave vector $\mathbf{k}$) with speed close or even equal to the phase velocity of the wave ($v_{ph} = \omega/k$) won't see a fluctuating field but rather a stationary one. In such a configuration, the particle can easily exchange its kinetic energy with the wave. Depending on the field configuration, this may lead to particle acceleration (particles gain energy from the wave and the wave is damped) or, vice versa, to particle deceleration (when the wave gains energy from particle and grows). We describe this situation as the wave being in resonance with the co-moving charged particle. The straightforward condition for the resonance, called *Landau resonance*, reads as

$$\omega - \mathbf{k} \cdot \mathbf{v} = 0 \tag{2.8}$$

where ω is the frequency of the wave, $\mathbf{k}$ is the wave vector and $\mathbf{v}$ is the particle's velocity.

Contrary to a chaotic motion in neutral gases, the motion of charged particles in plasmas embodies periodic features with some typical frequencies. These are the gyration of particles around the magnetic field lines with the cyclotron frequency for a plasma specie j given as

$$\Omega_{cj} = \frac{q_j B}{m_j} \tag{2.9}$$

and plasma oscillations with typical plasma frequency

$$\omega_{pj} = \sqrt{\frac{n_j q_j^2}{m_j \epsilon_0}} \tag{2.10}$$

Another possible particle resonance, the *cyclotron resonance*, is then related to the periodic gyromotion. The particles become resonant with the wave if the condition

$$\omega - \mathbf{k} \cdot \mathbf{v} \pm \Omega_c = 0 \tag{2.11}$$

is fulfilled. In other words, if a field perturbation rotates in the same direction and frequency of the rotation is similar with the one of the periodic gyration, particles in their rest frame do not feel a variable field but again a static one. Thus the energy between wave and particles can be easily exchanged.

In the MHD approach, by definition, all particles of one specie are having the same mean properties (bulk speed, temperature, etc.). This is not the case in the (more realistic) kinetic description where the state of all particles is defined through the VDF. Therefore, for a given wave, only some of the particles can be resonant while the others are not. Then, depending whether more particles are accelerated or decelerated by the wave activity, the wave is either damped or becomes unstable and its amplitude grows. This is mostly determined by the shape of the VDF around the region of resonance. In other words, if the VDF can convert its free energy to the unstable mode, the wave will grow, otherwise no instability will arise. This is the basic driving mechanism of the kinetic plasma instabilities.

Non-drifting isotropic Maxwellian VDFs will always lead to wave damping and energy absorption. Only departures from purely isotropic Maxwellian distributions,

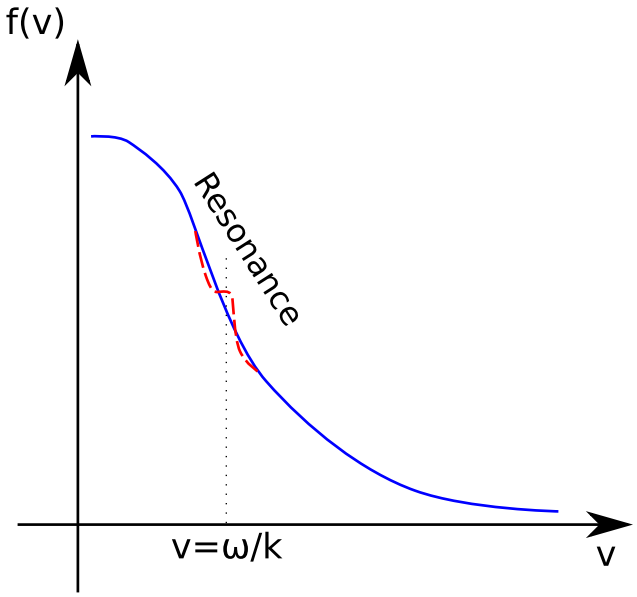

Figure 2.3: (Adapted from *Baumjohann and Treumann* (1996)) In the kinetic treatment, only particles with speeds close to the condition of resonance feel the effect of the wave. Depending whether more particles are accelerated or decelerated, the wave is either damped or its amplitude grows.

e.g., beams, temperature anisotropies or skewed VDFs, represent a natural source of free energy which can excite some unstable wave modes. These generated waves then in turn can retroactively redistribute their energy and regulate the initial VDF distortions. For example, wave-particle interactions resulting from temperature anisotropy driven plasma instabilities represent therefore an effective mechanism which can constrain the temperature anisotropy of a VDF during its evolution in the expanding solar wind. More generally, in a stable configuration, there are no enhanced fluctuations in the plasma which can constrain its macroscopic characteristics. In contrast, if enhanced unstable fluctuations are present, the consequent wave-particle scattering rapidly leads the unstable configuration of the plasma state back to a marginal stability.

2.2.2 Temperature anisotropy instabilities

One of possible sources of free energy which may give rise to unstable electromagnetic fluctuations is the temperature anisotropy of the observed VDFs. In general, the more anisotropic is the plasma temperature, the higher is the growth rate γ of the corresponding unstable mode and the larger are field fluctuations caused by the given instability. The enhanced fluctuations from these instabilities reduce the anisotropy of the distribution function by wave-particle scattering. The anisotropy driven instabilities therefore put constraints on the temperature anisotropy $T_\perp/T_{||}$ itself. The unstable modes can be derived from the linear Vlasov theory. In the

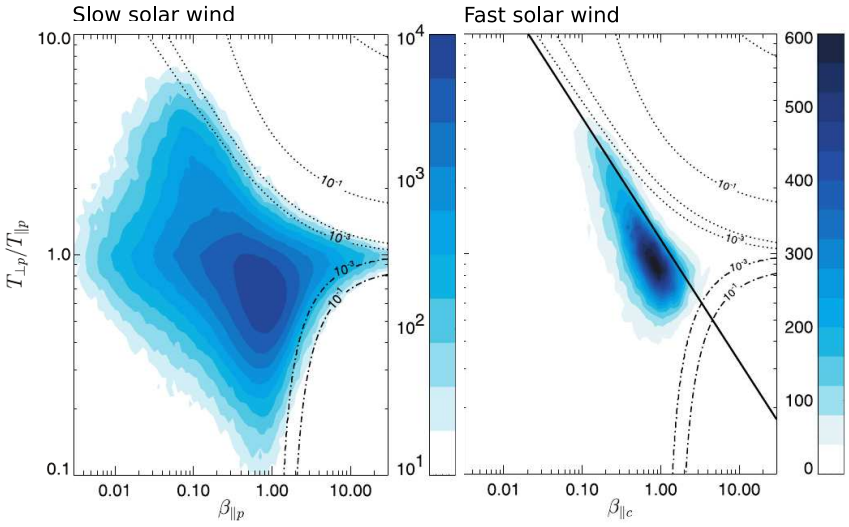

Figure 2.4: (Adapted from *Hellinger et al.* (2006)) Observations of the proton temperature anisotropy from WIND spacecraft as a function of the proton parallel $\beta_{||} = 8\pi n k_B T_{||}/B^2$ in the slow (left panel) and fast solar wind (right panel). The over plotted curves show the isocontours of the maximum growth rate for the mirror (dotted line) and oblique propagating fire hose (dash-dotted line) instabilities.

current study we will examine the effect of two most dominant electron temperature anisotropy driven instabilities.

The first type arises when the perpendicular electron temperature is greater than the parallel one ($T_{e,\perp}/T_{e,||} > 1$). For an electron population described by a single bi-Maxwellian distribution and for a sufficiently homogeneous plasma, the fastest growing instability caused by this type of anisotropy is the whistler one (*Kennel and Petscheck* (1966) and *Dum et al.* (1980)). Electrons are cyclotron resonant with whistler waves of the left-hand polarisation while protons are not, thus the proton temperature has no effect on the properties of this instability. *Gary and Wang* (1996) further showed that the wave-particle scattering induced by the whistler instability maintains the initial bi-Maxwellian character of the eVDF and confirmed that $T_{e,\perp}/T_{e,||}$ can be bounded by the threshold condition of this instability. Maximum growth rates of the whistler instability correspond to a wave propagation along the background magnetic field. Oblique propagation is also possible. However, in this case the growth rate factors are smaller than those derived for the parallel wave vectors.

In the opposite case when $T_{e,\perp}/T_{e,||} < 1$ the electron fire hose instability can develop (*Hollweg and Volk* (1970)). This instability is a kinetic extension to higher frequencies of the MHD fire hose instability, originally described by *Parker* (1958). While the MHD fire hose instability is of a completely non-resonant nature, the kinetic electron fire hose instability is typically proton-resonant and for sufficiently large anisotropy of the electron distribution also electron-resonant (*Pilipp and Benz*

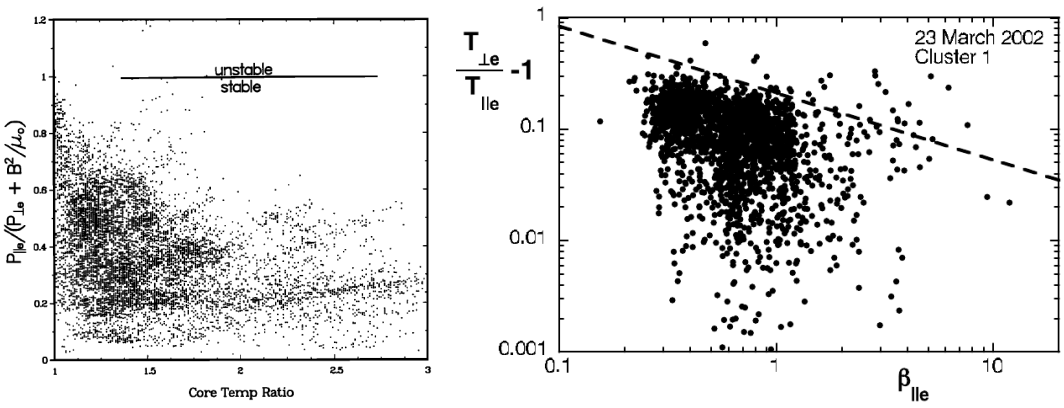

Figure 2.5: (Left panel) *Phillips et al.* (1989) analysed the electron temperature anisotropies ($T_{c,\perp}/T_{c,||}$ derived from ISEE 3 data with respect to the fire hose instability threshold defined by the kinetic ($P_{e,\perp}$,$P_{e,||}$) and magnetic (B^2/μ_0) pressures. Obviously most of all observations are found deep in the stable region far from the instability threshold. (Right panel) First observational evidence of the effect of whistler instability on the electron temperature anisotropy in the space plasmas was reported by *Gary et al.* (2005). The solid dots represent electron anisotropies measured by the CLUSTER spacecraft in the Earth's magnetosheath. The dashed line represents the corresponding threshold of the whistler instability as a function of the electron plasma beta.

(1977)). *Pilipp and Benz* (1977) considered only a parallel wave vector to the magnetic field. It was found by *Paesold and Benz* (1999) (and later confirmed by *Li and Habbal* (2000)) that an oblique propagation of the electron fire hose instability leads to higher growth rates. Note, that since protons are resonant with waves generated by this instability, growth rates for this instability are also a function of the proton temperature.

The effect of temperature anisotropy driven instabilities on the temperature anisotropy has already been studied in the case of solar wind protons from the observational point of view by *Kasper et al.* (2003), *Hellinger et al.* (2006), *Marsch and Tu* (2006) and *Matteini et al.* (2007), see Figure 2.4. These authors have shown fairly good agreement between the proton temperature anisotropy estimated from a large amount of WIND/SWE and HELIOS observations and constraints imposed by several theoretically predicted kinetic instabilities. Some studies of this kind have been already done also for electrons (see Figure 2.5). Solar wind electrons are rather observed with $T_{e,\perp}/T_{e,||} < 1$. *Phillips et al.* (1989) have shown on a large set of ISEE 3 measurements that electrons are typically found in the parameteric phase space of $(T_\perp/T_{||}, \beta_{||})$ far away from the fire hose threshold inside the stable region. First observational evidence of the effect of whistler instability on the electron temperature anisotropy in the space plasmas was reported by *Gary et al.* (2005). Using CLUSTER/PEACE measurements in the Earth magnetosheath, *Gary et al.*

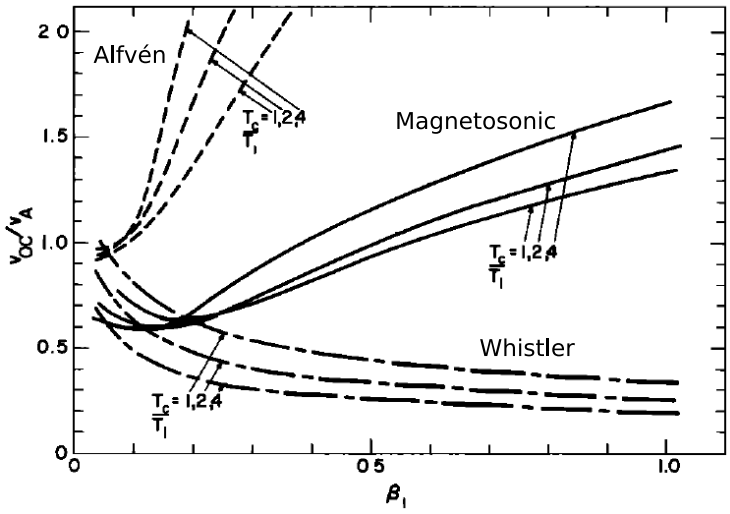

Figure 2.6: (From *Gary et al.* (1975)) Thresholds isocontours for the relative drift of the core component (normalized to the Alfvén speed) as a function of the ion plasma beta for different ratio of the electron core to ion temperature.

(2005) have shown that also whistler modes provide a constrain on the electron temperature anisotropy in the $(T_\perp/T_{||}, \beta_{||})$ space when $T_{e,\perp}/T_{e,||} > 1$. In chapter 5 we provide a summary of results presented in *Štverák et al.* (2008) where the temperature anisotropy estimated on a large data set was compared with theoretical constraints imposed by the whistlers and fire hose electron instabilities.

2.2.3 Heat flux instabilities

As well as the temperature anisotropies, the observed skewness of the solar wind eVDFs, i.e., the strahl component, which is responsible for the bulk of the solar wind heat flux, represents a source of free energy which can give rise to the plasma instabilities. Instabilities excited by this source of free energy can theoretically provide some constraints on the heat flux and consequently on the strahl itself. Observations indicate that the heat flux in the solar wind is not described by the conventional collisional conductivity (1.20), see, e.g., *Scime et al.* (1994a), instead its magnitude has a maximum limit which depends only on the local plasma parameters. Naturally, the observed upper bound of the solar wind heat flux can be related to the effect of corresponding kinetic instabilities.

Based on ideas of *Forslund* (1970), *Gary et al.* (1975) concluded from the the linear Vlasov theory that there are three kinetic instabilities, namely the Alfvén, magnetosonic and whistler instability, which can arise for a sufficiently large skewness of the eVDF. The model of *Gary et al.* (1975) used two bi-Maxwellian distributions, one for the core and one for the high-energy tails, and the heat flux was achieved by the relative drift of these two components. All three modes were shown to be electron resonant. While the magnetosonic and Alfvén modes resonate with

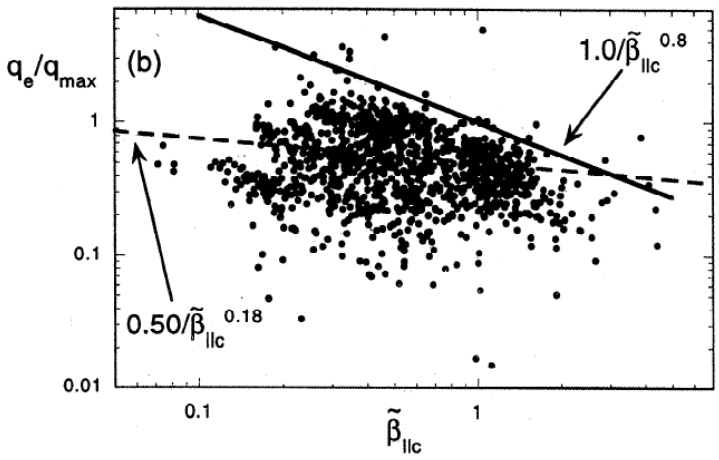

Figure 2.7: (From *Gary et al.* (1999)) Ulysses observations of normalized electron heat flux as a function of the parallel electron beta of the core component. The dashed line represents the fit to the data and the solid line represents the threshold condition for the whistler heat flux instability.

relatively slow electrons, the primary wave-particle interaction for the whistler heat flux instability is provided by high-energy electrons of non-thermal eVDF tails.

In order to decide which instability is the fastest growing one, we have to compare their threshold conditions. The value of growth rates factors of these heat flux instabilities depends on variety of parameters. *Gary et al.* (1975) showed that the whistler instability has the lowest threshold for most of the observed solar wind conditions. The magnetosonic and Alfvén instabilities become competitive only in some particular configurations (see Figure 2.6). Maximum growth rates of the whistler instability were examined in detail in *Gary et al.* (1994) and *Gary and Li* (2000). It was shown that the upper bound of the normalized heat flux (see Chapter 6 for explanations) is a function of the parallel plasma beta of the core component.

The numerical estimation of growth rates of the whistler heat flux instability were compared with in-ecliptic observations of the Ulysses mission by *Gary et al.* (1999), see Figure 2.7. It was shown, in agreement with the theoretical predictions, that the instability threshold provide a statistical constraint on the observed solar wind heat flux. The effect of whistler waves on strahl electrons was further numerically examined by *Vocks et al.* (2005), *Gary and Saito* (2007) and *Saito and Gary* (2007) with particle-in-cell simulations. These authors showed theoretically that whistler waves are capable of forming both the halo and strahl components and are effective in scattering of strahl electrons into the halo. In the chapter 6, we will apply theoretical findings of *Gary et al.* (1994) and *Gary et al.* (1999) to see whether the whistler heat flux instability can impose a constraint on the observed electron heat flux estimated from our fitting procedures.

Chapter 3

Data and Fitting Procedures

Observed solar wind eVDFs are typically composed from three different components: the thermal core, which typically represents more than 95% of the total electron number density, the hotter supra-thermal halo, representing the non-thermal tails which are present at all pitch angles, and the highly magnetic field-aligned beam-like component called the strahl. Several analytical models have been proposed in order to fit and study these non-trivial velocity distributions.

From the observational point of view, the first detailed solar wind eVDFs characterizations were done originally by *Feldman et al.* (1975) and later by *Pilipp et al.* (1987a,b). Their original model consisted of one bi-Maxwellian distribution for the core and a second bi-Maxwellian distribution drifting with respect to the solar wind plasma frame for the halo and strahl altogether. It was shown that the difference between the core and the halo charge fluxes (due to the relative core-halo drift) are in a good agreement with the zero-current condition as it is necessary to keep a zero current in the solar wind. Non-thermal electrons were shown to be the main source of the total electron heat flux. In addition, the natural choice of a Maxwellian distribution allowed an easier comparison with theoretical predictions. The Maxwellian VDF corresponds to a medium in local thermodynamic equilibrium which is the classical assumption in many theoretical approaches, namely in the MHD fluid descriptions. However, note that this is not valid anymore already for a sum of two Maxwellian distribution.

As an alternative, *Maksimovic et al.* (1997b) used a single Lorentzian or Kappa function f_κ to fit the entire eVDF

$$f_\kappa(v) \propto \left(1 + \frac{m}{k(2\kappa - 3)T} v^2\right)^{-\kappa-1} \tag{3.1}$$

At low speeds a Kappa distribution is nearly Maxwellian. Then It decreases as a power law at speeds greater than the thermal speed. The Kappa function can thus describe to a certain degree both the thermal core and the non-thermal tails but it does not describe the whole eVDF including the strahl.

More recently, *Maksimovic et al.* (2005) examined the relative importance of the non-thermal electrons in the fast solar wind as a function of the increasing radial distance from the Sun. These authors proposed that the best analytical model for

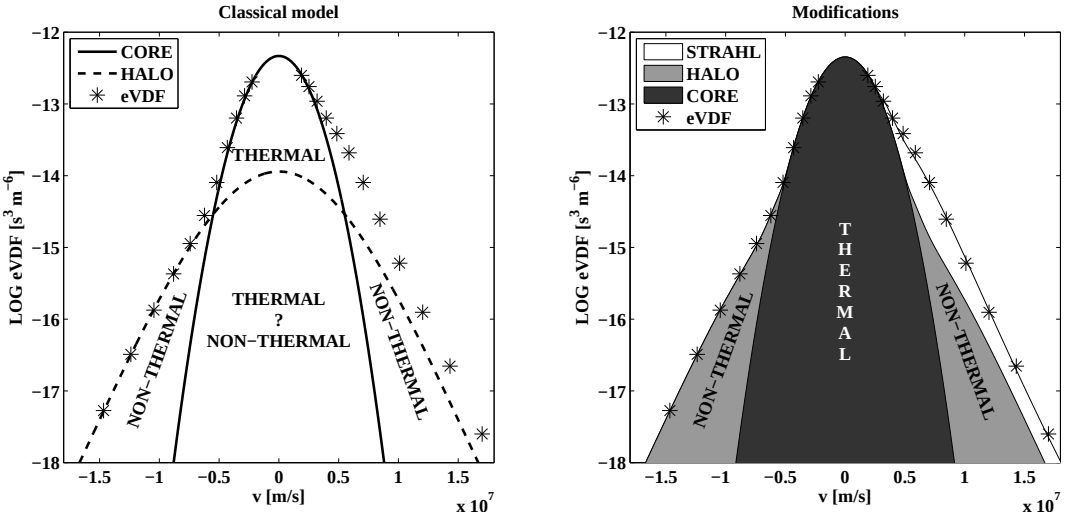

Figure 3.1: (From *Štverák et al.* (2009)) Classical eVDF model is not satisfactory for two reasons. It can not correctly handle the asymmetric strahl component and the halo component include both, electrons in the thermal equilibrium being the part of the core and non-thermal electrons at higher energies where tails are dominant above the Maxwellian core (left panel). The new model should include a third component for the strahl and separate the whole eVDF into the thermal (core) and non-thermal part (halo and strahl), giving a better estimation of their relative densities (right panel).

the core and halo is constituted by the sum of a bi-Maxwellian for the core and a bi-Kappa function for the halo. Concerning the strahl, they still did not propose any analytical model but rather computed its characteristics numerically by subtracting the core-halo model from measured eVDF. The complete fitting procedure of *Maksimovic et al.* (2005) proposed to model most precisely the solar wind eVDFs can be summarized as follows. As the first step, the portion of an eVDF, from which the strahl is absent, is fitted with the sum of one bi-Maxwellian (f_c) and one bi-Kappa function (f_h) for the core and halo respectively. f_c and f_h are defined over the whole velocity phase space $v_\perp$, $v_{||}$, where the subscripts $||$ and $\perp$ correspond to the direction with respect to the local magnetic field direction. Once f_c and f_h are determined, they are removed from the observed eVDF (f_{obs}) and the strahl characteristics such as the density are obtained by integrating $f_{obs} - f_c - f_h$ over the whole velocity phase space.

Even though the model of *Maksimovic et al.* (2005) represents an improvement to the previous models (a sum of two bi-Maxwellians or one single bi-Kappa function), this fitting procedure is still not fully satisfactory. The main two reasons are sketched in Figure 3.1. Firstly the missing analytical description for the strahl component is necessary for more accurate estimation of some fundamental parameters such as the electron heat flux. Secondly, there is a clear ambiguity when defining the halo component over the whole velocity phase space. On the left hand side of Fig. 3.1, it is not possible to decide whether an electron in the thermal velocity/energy range

belongs to the core population or to the halo one. Therefore, based on measured eVDFs, it is not possible uniquely define the model function of the halo component in the thermal energy range. Since the electrons in the thermal energy range represent a large fraction of the total halo density when f_h is defined over the whole velocity phase space, the resulting characteristics of the halo component in the classical model do not allow to separate and correctly describe properties of the thermal and non-thermal part of observed eVDFs.

In order to better compare and study separately properties of thermal electrons which are still affected by collisions and the suprathermal electrons which are almost collisionless, we proposed an improved model which analytically describes all three components of the observed eVDFs. The ambiguity between the thermal and non-thermal electrons is solved by restricting f_c and f_h to respectively the thermal and suprathermal parts of the velocity phase space as illustrated on the right-hand side of Figure 3.1. By doing so we can characterize more precisely the true difference between the theoretical Maxwellian distribution predicted for a gas in a local thermal equilibrium and eVDFs observed in the solar wind.

By use of the proposed analytical model, we perform a statistical study of a substantial amount of solar wind eVDFs. In our data set we combine measurements acquired on board three spacecraft (Helios, Cluster II and Ulysses) in the low ecliptic latitudes covering the heliocentric distance from 0.3 up to 4 AU. The complete descriptions of data samples and explanations of procedures which are applied on measured eVDFs before fitting them with the analytical model are given in the last two section of the current chapter.

3.1 Full Analytical Model

The model proposed for this study is composed of a sum of three analytical forms for each of the basic eVDF components observed in the solar wind, namely the core (f_c), halo (f_h) and strahl (f_s)

$$f = f_c + f_h + f_s. \tag{3.2}$$

For the core component we use a classical bi-Maxwellian function drifting in the parallel direction with respect to the magnetic field. Thus f_c reads as

$$f_c = A_c \exp\left[-\frac{m}{2k}\left(\frac{1}{T_{c\perp}}v_\perp^2 + \frac{1}{T_{c||}}(v_{||} - \Delta_c)^2\right)\right] \tag{3.3}$$

where m is the electron mass, k is the Boltzmann constant, $T_{c\perp}$ and $T_{c||}$ are the core perpendicular and parallel temperatures respectively and Δ_c is the drift velocity in the proton bulk speed frame. The normalization factor A_c is equal to

$$A_c = n_c \left(\frac{m}{2\pi k}\right)^{3/2} \frac{1}{T_{c\perp}\sqrt{T_{c||}}} \tag{3.4}$$

where n_c is the core number density.

For the halo population, we still use a bi-Kappa function as in *Maksimovic et al.* (2005) but drifting with the core. Moreover, we introduce one major modification in order to reach our requirements, that is the clear separation of the non-thermal electrons from the thermal ones. We require the inner part of the bi-Kappa function hidden in the thermal core to be truncated by the use of a flat top like function ($f_{h,ft}$). The analytical form for the halo (f_h) is then

$$f_h = (1 - f_{h,ft}) \cdot f_{h,\kappa}. \tag{3.5}$$

In (3.5), $f_{h,\kappa}$ is the classical bi-Kappa function defined as

$$f_{h,\kappa} = A_h \left(1 + \frac{m}{k(2\kappa_h - 3)} \left(\frac{v_\perp^2}{T_{h\perp}} + \frac{1}{T_{h||}}(v_{||} - \Delta_c)^2\right)\right)^{-\kappa_h - 1} \tag{3.6}$$

where m, k, $T_{h\perp}$ and $T_{h||}$ have the analogous meaning as in (3.3), Δ_c is the drift speed which is common for both the core and the halo and the κ_h parameter determines the power-law decrease of the suprathermal tails. The bi-Kappa function is normalized by

$$A_h = n_{h\kappa} \left(\frac{m}{\pi k(2\kappa_h - 3)}\right)^{3/2} \frac{1}{T_{h\perp}\sqrt{T_{h||}}} \frac{\Gamma(\kappa_h + 1)}{\Gamma(\kappa_h - 1/2)} \tag{3.7}$$

where $n_{h\kappa}$ is the zero-order moment of the Kappa function and $\Gamma()$ is the Gamma function. Because of the truncation, $n_{h\kappa}$, however, does not expresses the number density of the halo.

In (3.5), $f_{h,ft}$ is the so-called "flat top" function defined in our case as

$$f_{h,ft} = \left[1 + \left(\frac{m}{2k\delta}\left(\frac{v_\perp^2}{T_{c\perp}} + \frac{(v_{||} - \Delta_c)^2}{T_{c||}}\right)\right)^p\right]^{-q}. \tag{3.8}$$

This function is defined in such way that it creates a plateau (at level of one) symmetric with respect to the origin. At the edge of this plateau $f_{h,ft}$ rapidly falls with increasing velocity to zero. The width of the flat top is controlled via the parameter δ. The parameters p and q, which determine the shape of the edge of the plateau, are constant in this model and are equal to 10 and 1 respectively. These values are empirically found to be convenient for our analysis. Note that due to the truncation, the correct density of the halo component has to be computed by integrating (3.5) over the whole velocity phase space. Also the parameters $T_{h\perp}$ and $T_{h||}$ similarly do not correspond to the halo temperatures as it is the case for the core component.

Finally for the strahl population we also use a bi-Kappa function modified in such a way that it models only those high-energy electrons of the measured eVDF that are streaming away from the Sun and are aligned along the local magnetic field line. In general, the strahl exhibits properties similar to a beam-like population overrunning the core and halo electrons. Therefore, we use an analytical model with a positive drift in the parallel direction with respect to the plasma frame. More precisely, in the antisunward direction we use a classical bi-Kappa function

with a parallel temperature corresponding to the measured data. In the sunward direction the model is truncated by decreasing the parallel temperature with a given factor. This truncation excludes therefore the thermal core electrons from the strahl population. The analytical formula for the strahl is then

$$f_s = A_s \left(1 + \frac{m}{k(2\kappa_s - 3)} \left(\frac{v_\perp^2}{T_{s\perp}} + D\frac{(v_{||} - \Delta_s)^2}{T_{s||}}\right)\right)^{-\kappa_s - 1} \tag{3.9}$$

with

$$\begin{array}{ll} D = 1 & for \quad v_{||} \geq \Delta_s \\ D = \Theta & for \quad v_{||} < \Delta_s \end{array} \tag{3.10}$$

where m, k, $T_{s\perp}$, $T_{s||}$ and κ_s have analogous meaning as in (3.6), Θ in the case of $v_{||} < \Delta_s$ causes the eVDF to be truncated in the sunward direction and Δ_s is the drift of the beam with respect to the proton plasma frame. The function is normalized by

$$A_s = n_s \frac{2\sqrt{\Theta}}{\sqrt{\Theta + 1}} \left(\frac{m}{\pi k(2\kappa_s - 3)}\right)^{\frac{3}{2}} \frac{1}{T_{s\perp}\sqrt{T_{s||}}} \frac{\Gamma(\kappa_s + 1)}{\Gamma(\kappa_s - 1/2)} \tag{3.11}$$

so that n_s gives directly the strahl number density. During the fitting we do not adjust the parameter Θ. Actually the value of Θ is fixed to 10, this ensures a sufficient cutoff inside the thermal core velocity range. For our needs this value was empirically found to be convenient over the whole range of the observed eVDF characteristics.

Altogether, we have fourteen free parameters when adjusting (3.2), i.e. n_c, $T_{c\perp}$, $T_{c||}$, Δ_c, n_h, $T_{h\perp}$, $T_{h||}$, κ_h, δ, n_s, $T_{s\perp}$, $T_{s||}$, κ_s and Δ_s. Instead of fitting directly the measured values (f_m), we fit their logarithm ($\log f_m$). This is done in order to take into account the high-energy part of the eVDF, which is some orders of magnitude smaller than the central thermal part of the velocity distribution. Since our model eVDF depends non-linearly on the fitted parameters, we use an iterative fitting technique based on the well known Levenberg-Marquardt algorithm (*Marquardt* (1963)) to minimize the χ^2 function.

The fitting procedure itself consists of several consecutive steps. First the initial guesses of the parameters for the core, halo and strahl are performed separately and then a final fine adjusting fitting with all parameters together is accomplished. An example of an outcome of our fitting procedure is shown in Figure 3.2 for a sample acquired on board the Helios spacecraft. In these four panels, all of the eight azimuthal bins measured on board Helios are displayed with asterisks and the model eVDF and its three components, the core, the halo and the strahl, are represented with the solid, dashed, dash-dotted and dotted line respectively. The two main features of our new model are visible. The model functions for the high-energy tails are truncated on the thermal core velocity range, and the fit describes very well the complete eVDF including the asymmetric part in the parallel direction, i.e. the strahl. We chose a Helios data sample for the demonstration of the new model because of its relative simplicity. For Cluster and Ulysses observations the quality of our fitting procedure is similar.

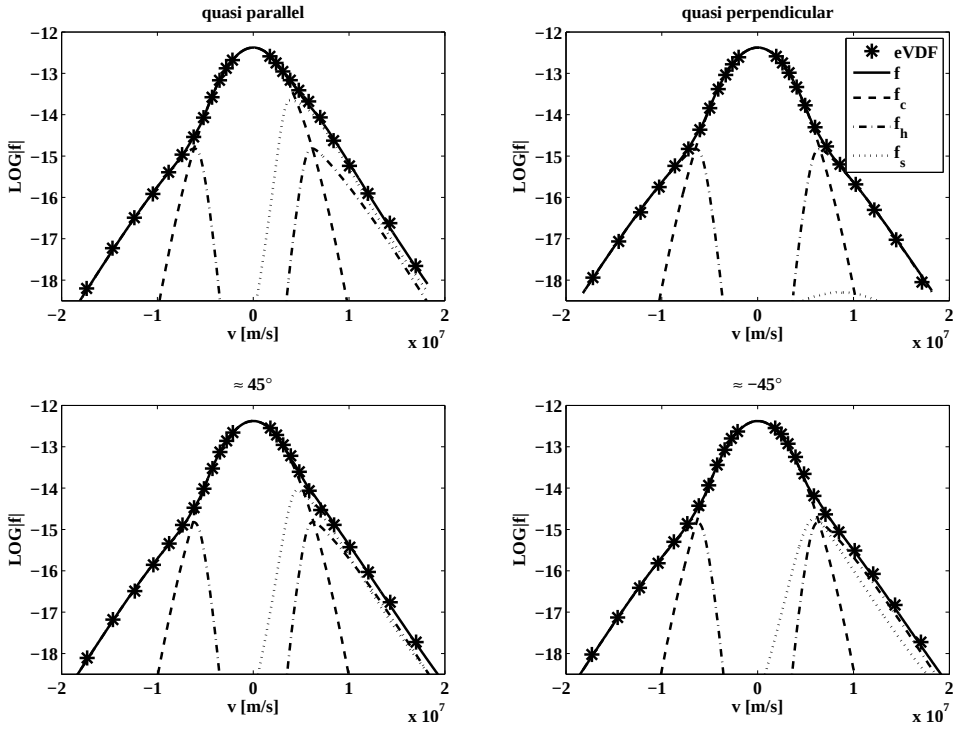

Figure 3.2: (From *Štverák et al.* (2009)) Sample fit of a measurement from Helios spacecraft using the analytical model proposed for our study. All three components of the measured eVDFs are included and both halo and strahl are truncated in the thermal part of the distribution. The asterisks, dashed line, dash-dotted line and dotted line represents the measured eVDF, core, halo and strahl population respectively. In these four panels all cuts through the eight azimuthal bins measured on board Helios are displayed. The strahl is strongest in the antisunward parallel direction while it is almost negligible in the perpendicular one. The halo is presented at all pitch angles.

The present work summarizes our results published in *Štverák et al.* (2008) and *Štverák et al.* (2009), where the already described model was not yet fully developed. In fact, results reported in *Štverák et al.* (2008) were obtain with model similar to the one of *Maksimovic et al.* (2005) where the strahl component was missing and the halo was not truncated in the thermal part of the eVDF. In the later work of *Štverák et al.* (2009), the model used to fit the measured eVDFs was already very similar to the current one. The only difference was that the halo component had no drift velocity with respect to the solar wind frame. One should keep in mind these differences when reading the discussions in chapters 4 and 5.

3.2 Computing Model eVDF Moments

The fitting parameters of the core component are directly consistent with the moments of the core itself, i.e., n_c, $T_{c\perp}$ and $T_{c||}$ give the core density and perpendicular

and parallel temperatures respectively. However, this is not the case for the halo and the strahl. The analytical form of these two components is not based on the familiar Maxwellian distribution and the concept of the thermodynamic temperature becomes violated. For a more general Lorentzian or Kappa distribution function the fitting parameters are still related to the physical meaning of the thermodynamic temperature as a measure of mean kinetic energy of individual particles. However, the bi-Kappa functions in the halo and strahl models are in addition truncated in the thermal regime and the original parameters of the bi-Kappa function lose their physical significations. Although we compute the true moments of the non-thermal components as defined in (1.2)-(1.6), note that the term temperature of the strahl and especially of the halo component has to be taken with caution compared to the classical thermodynamic temperature of the core.

Substituting analytical forms of halo and strahl components into (1.2)-(1.6) and computing the moments of these non-thermal components introduces some computational difficulties. While the high-energy tails of the Maxwellian distribution decrease exponentially with the increasing velocity, the tails of the Kappa distribution follow a power-law decrease

$$f_\kappa \sim (1+v^2)^{-(\kappa+1)}. \tag{3.12}$$

The VDF moments for the Kappa function can be thus written in a general integral form as

$$m_{n,\kappa} \sim \int_{-\infty}^{\infty} x^n (1+x^2)^{-(\kappa+1)} dx. \tag{3.13}$$

which is convergent only if

$$\kappa > \frac{1+n}{2}. \tag{3.14}$$

In the solar wind, the κ parameter can reach the values $\kappa \lesssim 2$ (*Maksimovic et al.* (1997b)). Therefore, from (3.14) the higher eVDF moments are not defined for the full range of κ observed in the solar wind plasmas.

One possible way how to solve this inconvenience is to restrict the integrating domain to a finite volume of the velocity phase space. The restrictions can be achieved by setting an maximum velocity v_{max} for the upper limit of the integration. Thus the general form of the moment definitions (1.2)-(1.6) will transform to

$$\iiint\limits_{|\mathbf{v}|<v_{max}} v^n f(\mathbf{v}) d\mathbf{v}. \tag{3.15}$$

A natural limit for the maximum velocity can represent for instance the speed of light. We have constrained the integration domain by the maximum velocity $v_{max} = 2.5e7 \;\; m/s$ which slightly exceeds the maximum energy range of all three instruments used in our data set. The main reason for this choice of the velocity constraint is that such restriction of the integrating domain does not add any substantial artificial information to the measured eVDFs. The resulting moments then describe only what we really observe.

S/C	Instrument	Period	Distance (AU)	Samples
HELIOS	I2	1975-78	0.3-1.0	$\approx$ 200 000
CLUSTER II	PEACE	2002-03	1.0	$\approx$ 25 000
ULYSSES	SWOOPS	1990-91	1.2-3.95	$\approx$ 15 000

Table 3.1: The measurements of eVDFs used in this study include data from several spacecraft: Helios 1 & 2, Cluster II and Ulysses. The data set includes roughly 240 000 samples covering the radial distances from the Sun from 0.3 up to 4 AU.

Because of the complicated analytical description of the strahl and especially of the halo, the definite integrals resulting from application of (3.15) on (1.2)-(1.6) are computed numerically on a discrete velocity grid. Although the core component have the bi-Maxwellian form, for which the moments are convergent and also very easy to evaluate, we used the truncated moments given by (3.15) for all three eVDF components. This procedure ensures a reasonable comparison of the resulting moments between all three components. Also note that the difference between the full and truncated moments for a bi-Maxwellian distribution is almost negligible which make this procedure acceptable when comparing our results with some previous studies of the core component.

3.3 eVDF Data Set

For our statistical study of electron properties in the solar wind, we have gathered a large number of measured eVDFs combining observations from three different space missions. In order to cover a sufficiently large spatial (radial distance) and temporal (different solar wind conditions) range we combine electron measurements obtained by the Helios 1 & 2, the Cluster and the Ulysses spacecraft. An overall description of the full data set and of the associated space instruments is given in Table 3.1. All measured data were acquired in the low ecliptic latitudes and cover altogether radial distances from 0.3 up to almost 4 AU. The data set thus represents the largest possible range of heliocentric distances in the ecliptic. Each one of the three spacecraft operated in a different time period, the data set thus combines several solar cycles and different periods of the solar activity.

On board the two Helios spacecraft electrons were measured with almost identical electron analyzers (*Schwenn et al.* (1975), *Rosenbauer et al.* (1977)). The probes continuously spun around an axis oriented perpendicular to the ecliptic plane. By use of the spacecraft rotation, the electron analyzer placed in the equatorial plane of the spacecraft recorded 2-D electron distribution functions. These velocity distributions cover an energy range between 0.5 and 1658 eV in 32 energy channels and 8 angular bins uniformly distributed in the polar plane. The radial coverage of both Helios probes ranges from 0.3 to 1 AU. For our analysis we use only those measurements for which the magnetic field vector is close enough to the ecliptic plane, that is when $B_z/|B| < 0.1$ (see *Štverák et al.* (2008) for more details). We

also require the magnetic field vector to be very close, with a maximum deviation of 10°, to the axis of one of the angular bins. These conditions guarantee to have a good estimate of the eVDF in the $(v_\perp, v_{||})$ plane, where the directions $\perp$ and $||$ are with respect to the local magnetic field vector.

The four satellites of the Cluster II mission (*Escoubet et al.* (1997)) measure electrons thanks to the PEACE instruments which are identical on each spacecraft (see *Johnstone et al.* (1997) for a detail description). The full energy range of all PEACE instruments scales from 0.6 eV to 26.5 keV. For our data set we use the SPINPAD data product which provides 2-D eVDFs covering one half of the $(v_\perp, v_{||})$ plane in 13 angular bins. In this study we use only data from Cluster 3. Since the spacecraft spends a part of its orbit in the Earth's magnetosphere we selected only periods when the satellite was in the unperturbed solar wind, not magnetically connected to the Earth's bow shock.

The data set is completed with measurements from the Ulysses spacecraft covering a radial range from 1.2 to 4 AU. On board Ulysses the eVDFs were measured by the SWOOPS instrument (*Bame et al.* (1992)). Its construction enables both 2-D and also full (95% of the unit sphere) 3-D electron measurements covering an energy range from 1.6 to 862 eV. We take data acquired only during the first part of the mission when the spacecraft traveled in the ecliptic plane towards Jupiter. The out of ecliptic fast solar wind measurements have already been analysed by *Maksimovic et al.* (2005). The 3-D eVDFs are projected in the $(v_\perp, v_{||})$ plane and then analysed in the same way as it is done for eVDFs from Helios and Cluster. Examples of measured eVDFs from the three space missions are displayed in Figure 3.3.

3.4 Corrections on Measured eVDFs

The space-born energy analyzers do not measure directly the eVDF but the counts of impacting electrons in corresponding energy/spatial bins of the instrument. By it self, this indirect technique of eVDFs acquisition represents a possible source of inaccuracy of the measurements. Based on the statistical nature of this measuring technique, a sufficient number of particle counts is needed to get a reasonable discrete approximation of the eVDF. With only a few counts per given measured energy bin the resulting value of the eVDF represents a non-negligible uncertainty. This problem becomes important at higher energies where the number of counts is rapidly decreasing. For samples in our data set, we exclude from further analysis all measured energy bins where the number of detected counts was two or less.

It is not only important to measure eVDFs with a good precision but also to interpret the measurements correctly. Not only is the measuring technique of eVDFs indirect, it is either interferenced by several other disturbing effects. The problem of a perfect plasma detector was already studied by *Song et al.* (1997). More recently, *Génot and Schwartz* (2004) and *Geach et al.* (2005) has shown that moments calculated directly from measured eVDFs can be overestimated up to more than 50% with respect to the real ones. Therefore, in order to get proper estimation of the electron properties, one has to first apply some corrections on the measured eVDFs

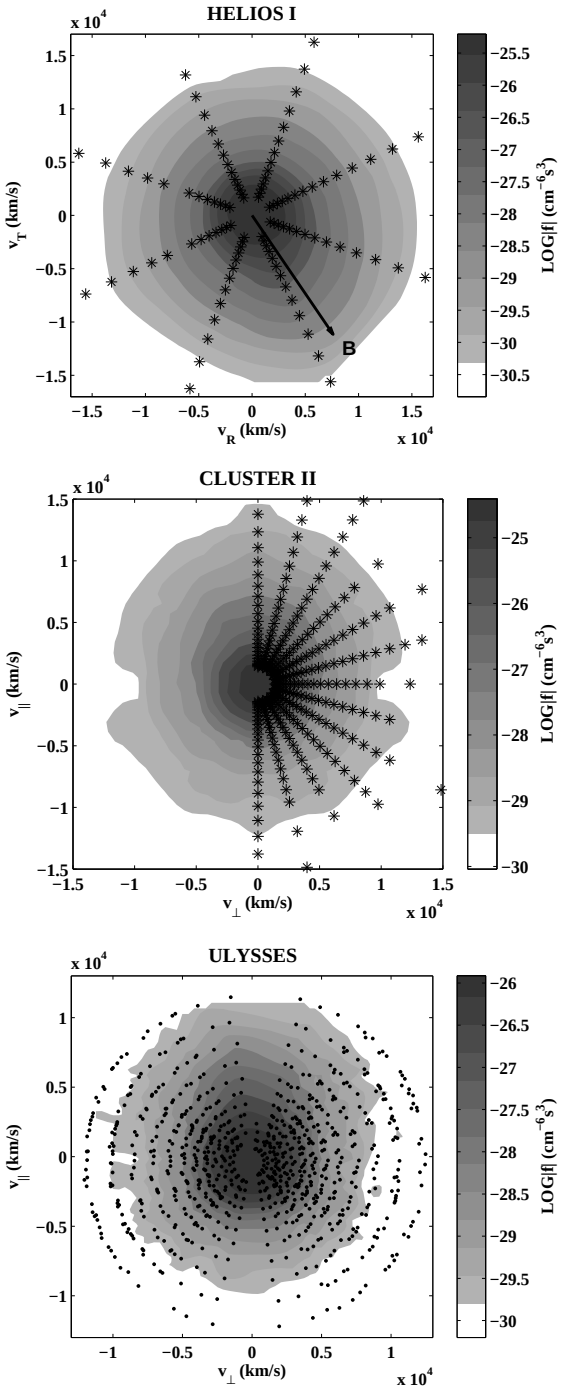

Figure 3.3: (From *Štverák et al.* (2008)) Examples of measured electron distributions acquired by the electron analyzer on board Helios I, Cluster II and Ulysses. The asterisks/dots represent the measured energy bins. For presentation purpose, the measured values are interpolated to a gray scale map. The arrow in the Helios sample shows the direction of the local interplanetary magnetic field.

before the main analysis can be performed.

In the solar wind, any object is exposed to a continuous flux of charged particles. An object with a conducting surface thus collects charge. At the same time photoelectrons are emitted from the surface by the effect of the solar radiation. As a result, the surface has a non-zero potential difference with respect to the ambient plasma. In the solar wind, this potential for a spacecraft (S/C) is typically positive and can reach up to a few tens of volts. Regarding the energy analyzers, this potential naturally leads to particle acceleration in the vicinity of the spacecraft. Measured eVDFs are thus distorted from those in the unperturbed plasma.

An electron with an initial kinetic energy $E_0 = \frac{1}{2}mv_0^2$ accelerated towards the analyzer by a potential $\Phi_{S/C}$ is detected with energy $E_{acc} = E_0 + e\Phi_{S/C}$. For 1-D detectors we may assume that only the radial component of the velocity is modified and the correction of the measured eVDF is quite straightforward. However, this scalar correction has limitations for 2-D instruments since the electric field (not strictly isotropic) produced by the potential around the spacecraft modifies not only the particle energies but also their trajectories. A corresponding, more sophisticated, vector correction was introduced by *Scime et al.* (1994b) for the Ulysses measurements. The authors mapped all the electron trajectories using the planar sheath approximation of the S/C electric field and consequently corrected not only the initial energy of the impacting electrons but also their actual velocity direction before entering the S/C sheath.

Without an a priori knowledge, correcting eVDFs to the effect of the potential is quite delicate since its value depends itself on the values we are estimating (the density and temperature). Estimation of the spacecraft potential is possible assuming the plasma to be locally neutral. Since estimation of ion densities is almost unaffected by the S/C potential ($E_{ion} \gg q_{ion}\Phi_{S/C}$) we can set the real electron density $n_{e,r}$ to the measured ion density $n_{ion,m}$. For a Maxwellian the measured eVDF $f_{e,m}$ distorted by the S/C potential $\Phi_{S/C}$ will be

$$f_{e,m} = n_{e,r}\left(\frac{m}{2\pi kT}\right)^{3/2}\exp\left[-\frac{m}{2kT}v_{||}^2\right]\exp\left[\frac{e\Phi_{S/C}}{kT}\right]. \tag{3.16}$$

Obviously the S/C potential does not change in this simple case the temperature of the electron population which can be estimated from the slope of $\log|f_{e,m}|$. The S/C potential can be then computed by comparing the real and measured electron density as

$$n_{e,m} = n_{e,r}\exp\left[\frac{e\Phi_{S/C}}{kT}\right]. \tag{3.17}$$

In our data set, the S/C potential was not measured on board Helios spacecraft. For its estimation, we used a generalized form of equation (3.17) for a sum of two bi-Maxwellian distributions. For the Cluster data, the S/C potential is available from in-situ measurements (*Gustafsson et al.* (1997)). Ulysses data samples were already corrected with a more sophisticated procedure. A complete description of this method is given in *Scime et al.* (1994b).

In addition, the measured eVDFs are at low energies polluted by photoelectrons emitted from the spacecraft itself. With a positive S/C potential, the relatively

cold photoelectrons ($E_{e,ph} < e\Phi_{S/C}$) are attracted back to the S/C surface and disallow measurements of pure solar wind electrons at lowest energies. The influence of photoelectrons has to be removed by introducing a given threshold energy and cutting off the whole part of the eVDF below this chosen energy limit. Consequently, the central part of the eVDF at low energies has to be recovered by fitting the unperturbed higher energy bins to some theoretical models. Otherwise one will loose important part of the distribution and the estimation of the eVDF moments will be incorrect. For our data set we set the energy threshold to 8 eV. This value was empirically shown to be sufficient in order to remove all possible photoelectron effects while keeping enough information for the subsequent fitting.

Finally it is convenient to apply a coordinate transformation from the S/C reference frame into the solar wind plasma frame where the desired moments of the eVDF should be computed. The S/C velocity is small with respect to the mean electron velocities and can be neglected. The transformation therefore consists in subtracting the solar wind bulk speed, usually taken from ion measurements, from the measured electron velocities. Note that this velocity transformation has to be applied after the corrections to the S/C potential.

Chapter 4

Radial Evolution of eVDFs

We have gathered more than 240 000 various solar wind eVDFs acquired in the low ecliptic latitudes. However, not all of the available samples were fitted by the model (3.2). In order to exclude measurements inappropriate for our analysis we imposed on our data set several restrictions.

For the Helios data, we analyse only measurements where the angle between the magnetic field vector and the axis of some of the eight azimuthal bins is sufficiently small. We impose an upper limit value of 10°. Less than 40% of Helios data set obeys this strong restriction. This approach however guarantees that at least one of the measured angular bins gives a good description of the strahl component. We apply a similar condition also to the Ulysses data: only measurements with enough data points in the strahl direction are taken for further analysis. For the Cluster data the first and last angular bins of the SPINPAD data product are always parallel to the local magnetic field line. Therefore, no restriction with respect to strahl characteristics are needed.

Next, the S/C potential was not measured directly on-board Helios, therefore, we first estimated its value for our further analysis. Consequently, we restricted the Helios data to samples with S/C potential estimated to be positive as it should be for spacecraft illustrated by the solar radiation. Finally, roughly only 50 000 samples from our initial data set satisfied all these restrictions and were processed by our fitting procedure.

We evaluate also the goodness of the fit, in order to better compare samples from different instruments. We compute a standard-error-like parameter ϵ defined by $\epsilon = (\chi^2/(N-1))^{1/2}$, where χ^2 is the sum of the squared deviations of the fit from the measured eVDF and N is the number of fitted points for the corresponding data sample. For further analysis, we keep only fits where this standard error satisfies $\epsilon \leq [\mu(\epsilon) + 2/3\, std(\epsilon)]$, here $\mu(\epsilon)$ is the mean value of ϵ over all eVDF samples and $std(\epsilon)$ is the standard sample deviation of the mean value. Furthermore, some of the samples are removed from the analysis by reason of unrealistic resulting parameters. For these samples, the standard error ϵ fulfills our condition for the quality of the fit but the resulting characteristics of the measured eVDF are considerably different from those typically observed, and the estimated moments do not correspond to expected conditions in the solar wind (e.g. core temperatures larger than 10^6 K

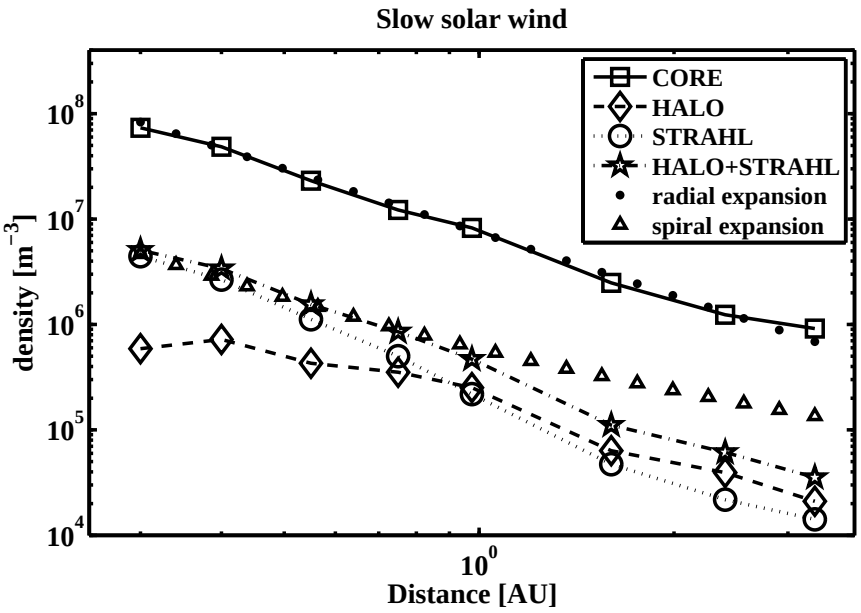

Figure 4.1: (From *Štverák et al.* (2009)) Radial evolution of the density profiles in the slow solar wind. Symbols represent mean values as computed from the fitting results in several radial bins. The error bars are of the order of the symbol size. Two theoretical reference profiles for a pure radial expansion and an expansion following the spiral magnetic field are plotted with dots and triangles respectively. The solid line with squares, dashed line with diamonds, dotted line with circles and dash-dotted line with stars represents the radial evolution of the core, halo, strahl and of the sum of the strahl and halo, respectively.

which is comparable to the temperature in the solar corona). Finally, only those results satisfying all these conditions imposed on the quality of the fit and on the resulting moments, about 70% of all fitted samples, are used for our final statistics.

By use of data from three different spacecraft we cover a heliocentric distance from 0.3 AU up to almost 4 AU. In this range we examine the radial profiles of the main characteristics of all three eVDF components, that is their densities and temperatures. We mainly focus on the radial evolution of the relative densities of the three eVDF components. Furthermore, by computing averages from all parameters, we provide an overview of the variation of the model eVDF shape with increasing radial distance. As a by-product of our analysis, we study the break-point energy of the electron population, i.e., the energy at which the eVDF loose its thermal (Maxwellian) properties and starts to develop the non-thermal tails. We examine also verify whether our model as applied on the large data set is in agreement with the zero-current condition in the solar wind.

Typically, three major regimes of solar wind flows are observed by space missions (*Marsch* (2006)). The first one is the steady fast wind originating from the open magnetic field lines in the coronal holes. The second is the unsteady slow wind

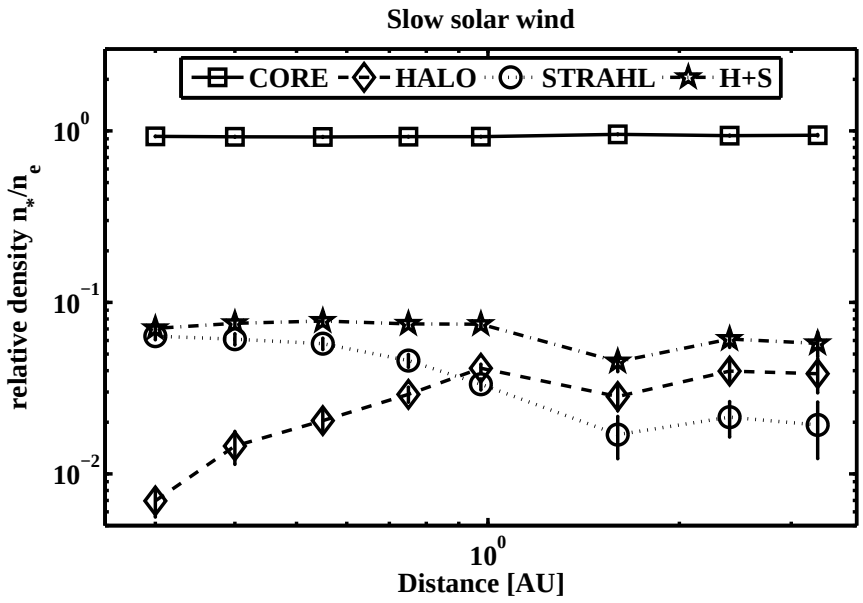

Figure 4.2: (From *Štverák et al.* (2009)) Radial evolution of the relative densities of the eVDF components for the slow solar wind observations. Symbols represent mean values with their error bars. The solid line with squares, dashed line with diamonds, dotted line with circles and dash-dotted line with stars represents the core, halo, strahl and a sum of strahl a halo, respectively. The total number of non-thermal electrons remains almost constant along the observed range. The strahl density decreases while the halo one concurrently grows - indicating electrons scattering between these two components.

coming from edges of temporarily open streamers or from opening loops and active solar regions. And finally, as a last solar wind regime we consider transient flows that are dominated by the so called coronal mass ejections (CMEs) prevailing during solar maximum cycle. In our study we focus on the main two regimes, i.e. the slow and fast solar wind. These two regimes are examined separately in the following two subsection.

We omit the transient disturbances for several reasons. The transient regime of the solar wind is associated with episodic solar events like ejections of material into interplanetary space from coronal regions. Therefore, for a large data set covering a sufficiently long time interval, the effect of such events on the overall average characteristics of the solar wind is assumed not to be significant.

4.1 eVDF radial evolution in the slow wind

We classify as a slow wind all the samples with a proton bulk speed lower than 500 km/s. This represents more than 90% of our whole data set. The density profiles for all three eVDF components and for the sum of the non-thermal parts

(i.e. the halo and the strahl) are shown in Figure 4.1. The whole data set is divided into radial bins in which the mean values of the respective densities are computed. The mean values are represented by squares for the core, diamonds for the halo, circles for the strahl and stars for the sum of the halo and the strahl. Error bars are of the order of the symbols size in this case.

For an isotropic steady state expansion the solar wind density should decrease as r^{-2}. In the solar wind, this should be the case of the core component. In Figure 4.1 we plot this theoretical profile (dots) for reference. It can be seen that this profile is in a good agreement with the radial evolution of the core density as expected. We find that this latter varies as $r^{-2.03\pm0.08}$, which indicates that the mean core density follows well, within the uncertainties, a steady state radial outflow. The halo and strahl profiles show different trends. While the strahl slope is slightly steeper, the halo density profile is flatter up to 1 AU. This difference demonstrates that the evolution of the non-thermal electron densities is more complex than a pure radial expansion.

For the strahl component we can not use the simplified approach of an isotropic expansion. Contrary to the core, the strahl is rather expanding along the magnetic field which can be approximated as radial only up to a limited distance. *Scime et al.* (1994a) has shown that a quantity expanding along the magnetic field in a spiral configuration (*Parker* (1963)) is rather proportional to

$$\propto \frac{1}{r^2}\sqrt{1+\left(\frac{r\omega}{v_{sw}}\right)^2} \tag{4.1}$$

where r is the heliocentric distance, ω is the angular speed of the Sun's rotation and v_{sw} is the solar wind speed. For a sufficiently small distance, (4.1) can still be replaced by $\sim r^{-2}$ but with increasing r this formula tends more to $\sim r^{-1}$. The theoretical profile (4.1) for a slow solar wind with $v_{sw} = 400\ km/s$ is plotted in Figure 4.1 with triangles. However, obviously neither this theoretical approach is matching with our observations. It is important to note that even by adjusting v_{sw} in (4.1) we can not achieve the observed characteristics. Therefore, other processes must explain the radial scaling of the density of the non-thermal eVDF components.

In addition to the radial profiles of the densities themselves, it is very useful to compute the radial variations of the relative number densities, i.e. the ratio of the density of individual eVDF components to the total electron density. In Figure 4.2 we plot these relative densities $n_{*,rel} = n_*/n_e$ of the eVDF components with respect to the total one n_e, that is the sum of the core, halo and strahl ($n_e = n_c + n_h + n_s$), again as a function of the heliocentric distance. The relative density of the core, halo, strahl and the sum of the halo and strahl are represented by solid line with squares, dashed line with diamonds, dotted line with circles and dash-dotted line with stars respectively. The vertical lines represent the error bars of the corresponding mean values in every radial bin. The most interesting result shown on this figure is the clear opposite trend between the halo and strahl relative densities. While the fractional number density of the strahl decreases with the radial distance, starting approximately at 6% at 0.3 AU and being less than 2% beyond 3 AU, the

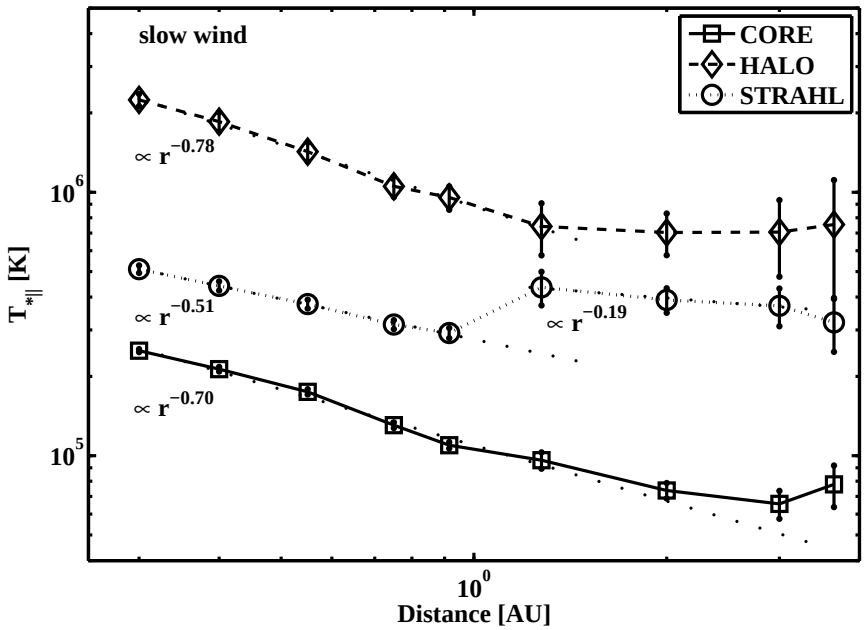

Figure 4.3: Radial evolution of the parallel temperatures of the three eVDF components in the slow wind. As for the density, the symbols represent mean values with their error bars. The solid line with squares, dashed line with diamonds and dotted line with circles represent the core, halo and strahl respectively. The mean values are overplotted with empirical power-law profiles (dotted lines). The core temperature gradient is in agreement with previous studies. For all three components, the cooling process slightly slows down beyond 1 AU.

halo relative density increases from less than 1% at 0.3 AU to more than 3% at the end of the observed radial range. There is another important result in Figure 4.2: by extrapolating the relative density of the halo component below 0.3 AU closer to the Sun, the contribution of halo electrons seems to be almost negligible with respect to the total electron density. The relative density of the summed non-thermal parts remains however more or less constant during the solar wind expansion as it is the case of the relative density of the thermal core. From our fitting it appears that the non-thermal electrons represent roughly 5-7% of the total electron number density, this fraction being constant with distance. These findings are similar to those observed by *Maksimovic et al.* (2005) in the fast wind except for the nominal values of the relative densities, which is due to the use of different fitting procedures. Our observations therefore support theories (*Gary et al.* (1994), *Vocks et al.* (2005), *Gary and Saito* (2007), *Saito and Gary* (2007)) proposing mechanisms which can be responsible for the scattering of the strahl electrons into the halo while keeping the thermal core unaffected.

Actually, the scattering of the strahl electrons can also partly explain the disagreement between the theoretical profile (4.1) and the observed one plotted in Figure 4.1. While in (4.1) we suppose the rarefaction of the strahl due to the expansion only, in Figure 4.2 we show that the decrease of the strahl density is also

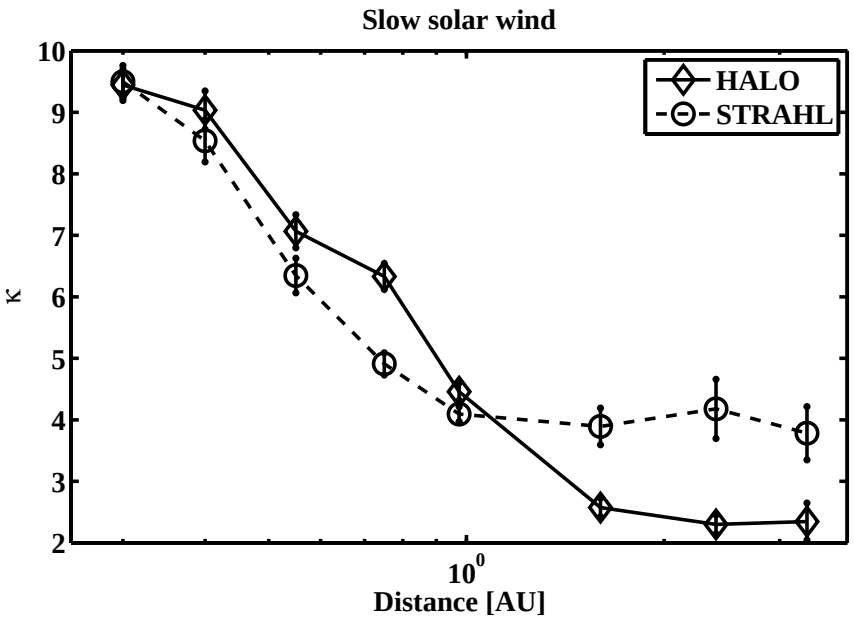

Figure 4.4: (From *Štverák et al.* (2009)) The parameter κ can serve as a measure of the non-thermal state of an electron population. Here we plot the mean κ parameter of the halo (dashed line with diamonds) and strahl component (dotted line with circles) in the slow solar wind as a function of the radial distance. Both of them are decreasing indicating stronger eVDF tails at larger distances from the Sun.

caused by the transfer of strahl electrons into other eVDF components.

Figure 4.3 shows the radial profile of parallel temperatures for the core (squares), halo (diamonds) and strahl (circles) respectively. We fitted the mean values in the radial bins up to 1 AU with a power-law profiles $T_{*,||} \propto r^{-\beta}$. The resulting profiles overplot the mean temperatures as a dotted lines with indicated values of the exponent β. For the core component the results with $T_{c,||} \propto r^{-0.70}$ are consistent with the previous findings of *Pilipp et al.* (1990), see Figure 1.1. Compared to the core the halo and strahl component are cooling slightly faster and slower respectively. The computation of the halo temperature, as described in the chapter 3, is different with respect to the previous studies where halo was modeled typically as a bi-Maxwellian or a bi-Kappa distribution functions. Therefore comparisons are rather irrelevant. Also for the strahl component, no observational results of the strahl temperature with a model comparable with our study have been yet reported. An important result clearly visible in Figure 4.3 is the deceleration of the cooling process beyond 1 AU. This may be related to the changing orientation of the IMF (*Scime et al.* (1994b)). There is no clear explanation for the jump in the strahl temperature around 1 AU. We suppose that it can be rather an artificial product related to different instruments used to acquire the eVDFs.

Another information about the non-thermal state of the observed eVDFs can be

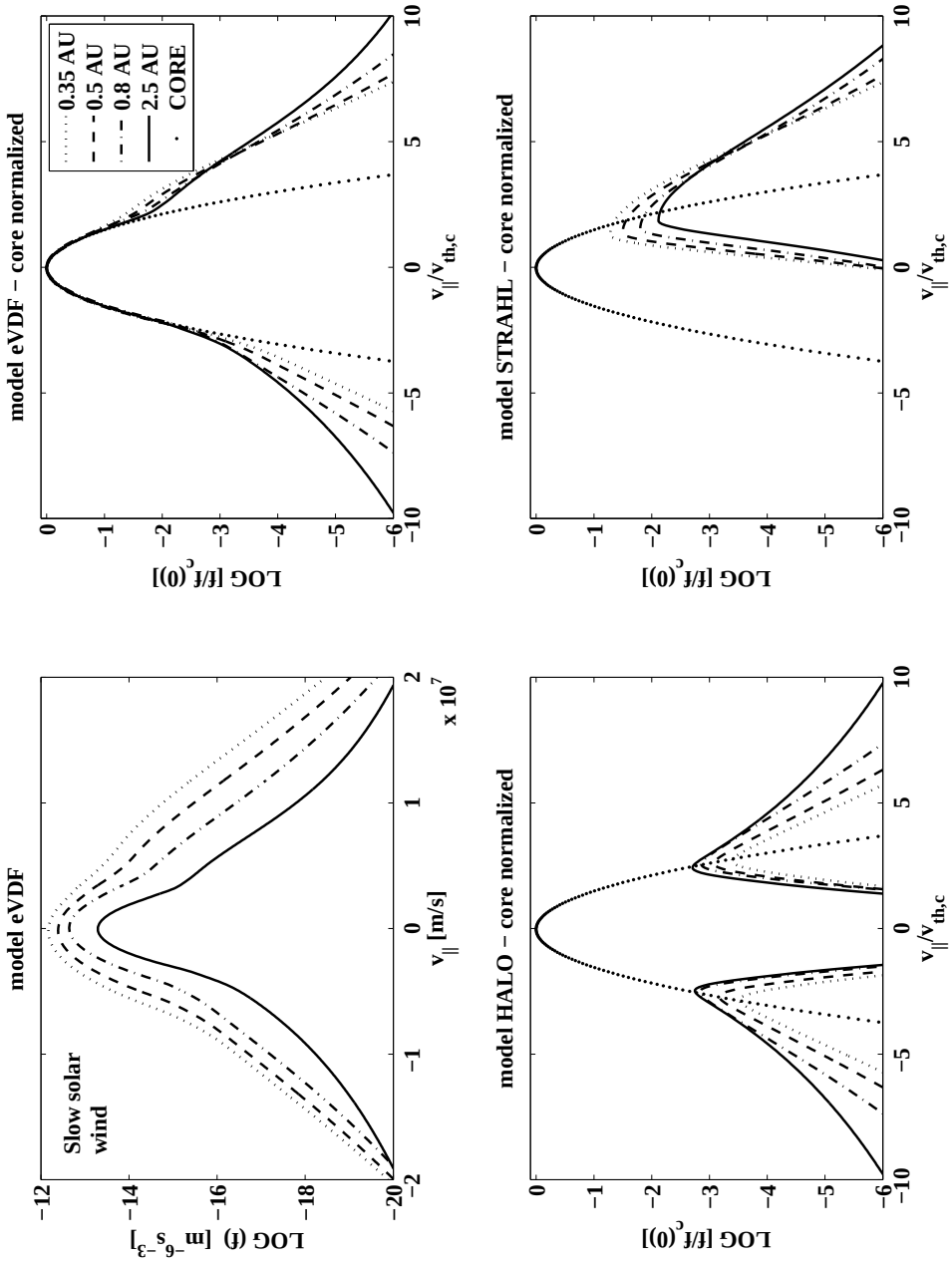

Figure 4.5: (From *Štverák et al.* (2009)) Radial evolution of a model eVDF function in the slow solar wind. Model functions are plotted using average values of all parameters as resulting from the fitting at four different radial distances: 0.35 AU (dotted line), 0.55 AU (dashed line), 0.75 AU (dash-dotted line) and 2.5 AU (solid line). Except the upper left panel, the model eVDF functions are normalized so that the value at the peak equals to 1 and the velocity is scaled by $v_{th,c}$ in order to remove the core radial trends. In the lower panels, the halo and strahl component evolution is compared with the normalized core. With increasing radial distance, the strahl electrons close to the thermal core are scattered, and the same time, the halo develops stronger tails and its relative importance is growing.

obtained from the parameter κ for both the halo and strahl components. The κ distribution is defined such as that with increasing κ, the function is becoming more and more Maxwellian (actually the distribution is almost Maxwellian for $\kappa \geq 10$). Therefore, we can use κ as a measure of the non-thermal character of the eVDF tails. The larger is κ the less pronounced are the tails. The radial evolution of κ is displayed in Figure 4.4. Here the dashed line with diamonds and dotted line with circles represent the κ parameter of the halo and strahl components respectively. For both of them, κ is decreasing with increasing radial distance. This means that as the solar wind expands, both the halo and the strahl become more and more non-Maxwellian.

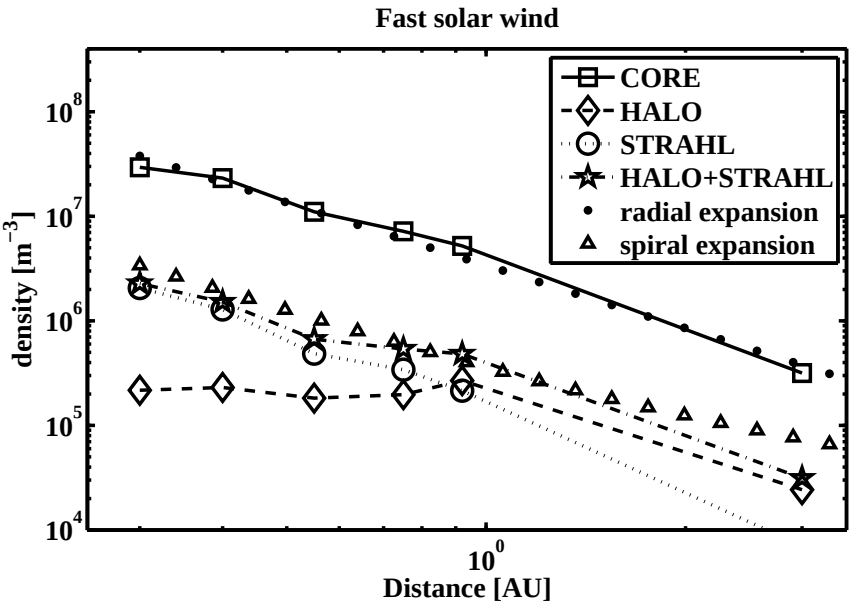

Figure 4.6: (From *Štverák et al.* (2009)) Radial evolution of the density profiles in the fast solar wind. As for the slow wind, the symbols represents the mean values as computed from the fitting results in several radial bins. The error bars are of the order of the symbol size. A theoretical reference profiles for an isotropic radial expansion and spiral expansion are plotted with dots and triangles respectively. The solid line with squares, dashed line with diamonds, dotted line with circles and dash-dotted line with stars represents the core, halo, strahl and a sum of strahl and halo, respectively.

In Figure 4.5, we summarize the radial evolution of the observed eVDFs in the slow solar wind. We display the radial evolution of the model distribution function (3.2) computed using the average parameters from the fitting process. Four different radial distances are compared: 0.35 AU (dotted line), 0.55 AU (dashed line), 0.75 AU (dash-dotted line) and 2.5 AU (solid line). Figure 4.5 thus gives very nice picture of the radial evolution of a typical eVDF shape in the slow solar wind. For every radial bin, we plot the cut of the model eVDF along the velocity parallel to the

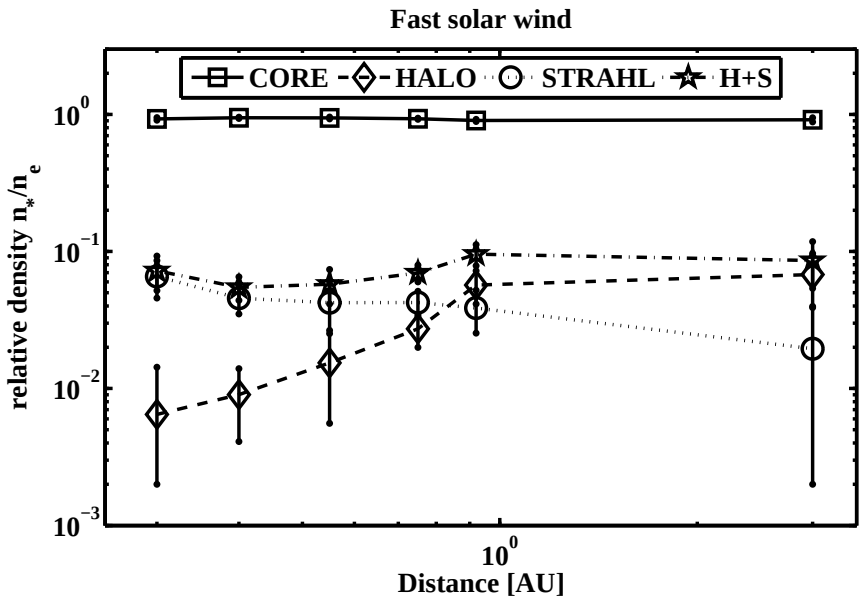

Figure 4.7: (From *Štverák et al.* (2009)) Fast wind radial evolution of the relative densities of the eVDF components. Symbols represent mean values and their error bars. The solid line with squares, dashed line with diamonds, dotted line with circles and dash-dotted line with stars represents the core, halo, strahl and a sum of strahl a halo, respectively. The total number of non-thermal electrons remains almost constant along the observed range, strahl density is decreasing while halo grows at the same time. The sum of non-thermal components seems to be more variable than in the slow wind.

magnetic field. In the upper left panel we plot the model eVDF as it results from the fitting procedure. One can see the natural cooling and rarefaction caused by the solar wind expansion. In order to better compare the radial evolution of the shape of the eVDF, we plot the normalized model functions in the remaining three panels. The normalization is done in such a way that the maximum of f is set to 1 and the velocity is given in $v_{th,c}$ units, where $v_{th,c} = \sqrt{2kT_{c||}/m}$ is the parallel thermal speed of core electrons. Such normalizations remove the radial trends (the cooling and rarefaction) of the core component caused by the solar wind expansion. The core component is represented in these three panels with dots. The upper right panel represents the whole model eVDF while the lower panels show the halo and strahl components respectively. All the properties discussed in Figures 4.1, 4.2 and 4.4 are also visible in Figure 4.5. The halo tails density is increasing at the expense of the strahl (as in Fig. 4.2). The non-thermal character of both the halo and the strahl increases with the heliocentric distance (as in Fig. 4.4). The lower right panel of Figure 4.5 is very interesting. It allows to better visualize the strahl scattering. From this figure it appears that strahl electrons around the core boundary, where the core electrons are still enough numerous, thus close to the thermal regime, decreases

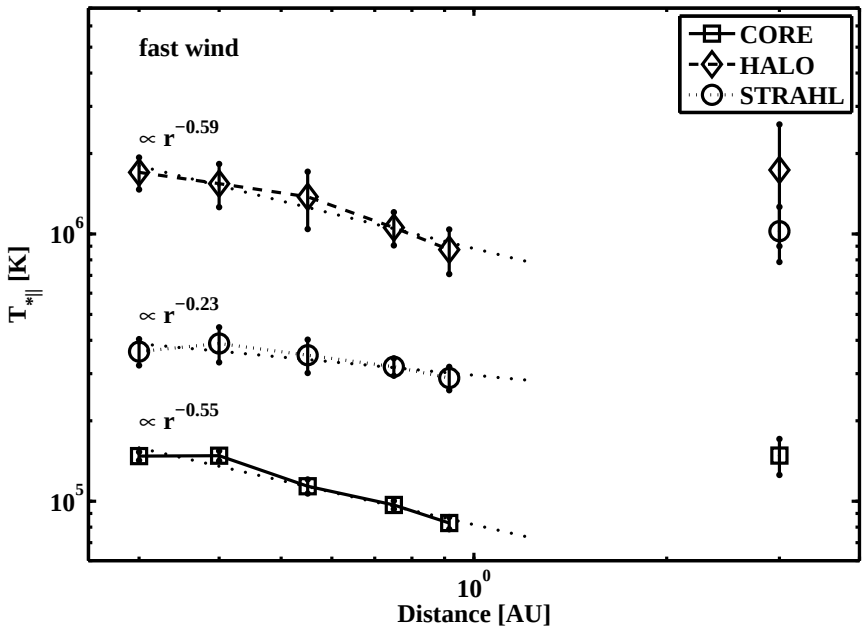

Figure 4.8: Radial evolution of the parallel temperatures of the three eVDF components in the fast wind. The symbols represent mean values in several radial bins. The solid line with squares, dashed line with diamonds and dotted line with circles represent the core, halo and strahl parallel temperature respectively. The mean values are overplotted with empirical power-law fits (dotted lines) up to 1 AU. There is a lack of fast wind observations at higher radial distances

significantly during the expansion and probably scattered in other pitch angles into the halo population. This behaviour can mean that Coulomb collisions could also act as one of the strahl scattering mechanisms.

4.2 eVDF radial evolution in the fast wind

The fast solar wind is in general considered as a steady-state outflow compared to the less stationary slow wind regime. It is typically less dense than the slow wind and the eVDF non-thermal features are thus observed to be more important. For our statistics we have selected only eVDF samples with measured proton bulk speed greater than 600 km/s. In our data set which includes in-ecliptic observations, only roughly 10% of the total number of eVDF samples represent the fast solar wind regime. Moreover, there are only about one hundred samples with the given bulk speed condition in the Ulysses radial range (1.2-4 AU). This can yield therefore larger uncertainties in the estimation of the mean eVDF properties. Nevertheless, in order to make the study complete, we present here the results concerning the fast solar wind, even though the statistical conclusions, in this case, will have to be taken with caution.

All figures concerning the fast wind are analogous to the previous subsection 4.1

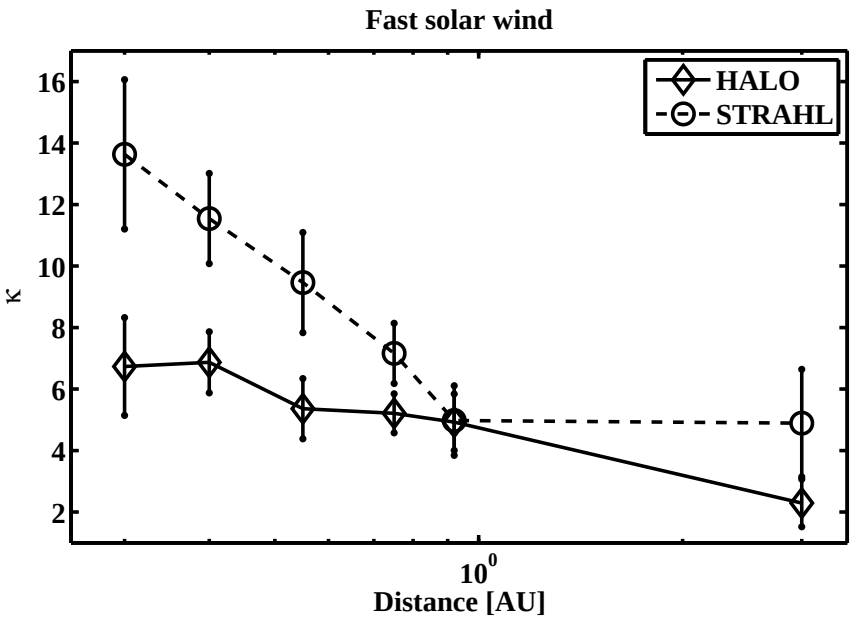

Figure 4.9: (From *Štverák et al.* (2009)) The parameter κ can serve as a measure of the non-thermal state of an electron population. Here we plot the mean κ parameter in the fast wind of the halo (dashed line with diamonds) and strahl component (dotted line with circles) as a function of the radial distance. Both of them are decreasing, indicating stronger eVDF tails at larger distances from the Sun.

describing the slow wind. The radial evolution of the electron number densities is shown in Figure 4.6. As for the slow wind, we plot all three eVDF components plus the sum of the two non-thermal parts. Again, the core density decreases as $\sim r^{-2}$. The exact law for the core density in the fast wind is proportional to $\propto r^{-2.11\pm0.17}$, with the exponent slightly smaller compared to *Maksimovic et al.* (2005). The radial trends of the halo and strahl densities are also similar to the slow wind case. At 0.3 AU the strahl density is higher than the density of the halo but it falls faster with radial distance. Therefore, the halo density overcomes at certain distance, around 1 AU, the strahl one. The radial profile of the strahl density decreases still slightly more steeply than the prediction for an expansion along the spiral oriented magnetic field. The theoretical profile for a spiral expansion (4.1), plotted with triangles in Figure 4.6, is now computed for the solar wind speed $v_{sw} = 650\ km/s$.

The relative densities of the eVDF components are displayed in Figure 4.7. Globally as for the slow wind case, the results for the fast wind tend to support the theory of strahl electrons being scattered into the halo, however, with two noticeable differences. First the sum of the halo and strahl relative densities is more variable with radial distance compared to the almost constant trend observed in the slow wind case. This could be due to either a statistical effect caused by a lack of fast wind samples, or to some possible interplay between the core and strahl/halo electrons

as well. Secondly, as already reported by several previous studies (*Feldman et al.* (1975), *Pilipp et al.* (1987a) and *Pilipp et al.* (1987b)) the relative densities of the non-thermal parts in the fast wind case are slightly higher compared to the slow wind one. The strahl relative density starts at 0.3 AU between 7 and 8% and falls to about 2% at 3 AU. The halo relative density, being less than 1% at the closest observed radial range to the Sun, reaches about 7% at 3 AU, i.e. about 4% more compared to the slow solar wind results.

The radial profiles of the parallel temperatures in the fast wind are shown in Figure 4.8 again for the core (squares), halo (diamonds) and strahl (circles) respectively. The empirical power-law profiles $T_{*,||} \propto r^{-\beta}$ which fit the mean values up to 1 AU, now mainly because of the lack of fast wind observations from the Ulysses spacecraft, are displayed with dotted lines. The core profile $T_{c,||} \propto r^{-0.55}$ is still in the range reported by *Pilipp et al.* (1990). In general, the cooling in the fast wind of the core, and as well of the halo and strahl components, is found to be much slower than in the slow wind (compare with Figure 4.3). However, the main trends are the same. The strongest gradient is observed for the halo component while the slowest cooling is again observed for the strahl and the core is in between. Contrary to the slow wind, we do not have enough observations beyond 1 AU in order to make any conclusions about larger heliocentric distances.

Regarding the non-Maxwellian character of eVDF tails in the fast wind, the radial evolution of the parameter κ for both the halo and the strahl components is qualitatively similar to the slow wind case. However, Figure 4.9 shows that at 0.3 AU the halo eVDF tails are already more non-Maxwellian than in the slow wind (compare Figure 4.4), while the relative densities are roughly the same.

As for the slow wind case, we plot in Figure 4.10 the radial evolution of the model distribution function (3.2) for the fast wind. We compute the average values of all parameters at four radial bins: 0.35 AU (dotted line), 0.55 AU (dashed line), 0.75 AU (dash-dotted line) and 3 AU (solid line). Because of the lack of fast wind data samples, the furthest radial bin differs from Figure 4.5. The upper left panel displays the overall model distribution, while in the other panels the model function and its components are normalized with respect to the total density (y-axis) and to the core thermal parallel velocity (x-axis) again in order to remove the effects of the cooling and the rarefaction of the wind. The relative growth of the halo and the damping of the strahl as well as the decrease of the parameter κ for both of the non-thermal components are clearly visible on the lower-left and lower-right panel respectively. The basic trends in the radial evolution for the fast solar wind are actually very similar to those we have shown for the slow wind regime. However, the nominal values of the relative densities indicate on average stronger non-thermal tails.

4.3 Break-point energy

Due to the properties of Coulomb collisions the solar wind electrons can be treated as a gas in a thermal equilibrium only up to certain energy level. Particles beyond

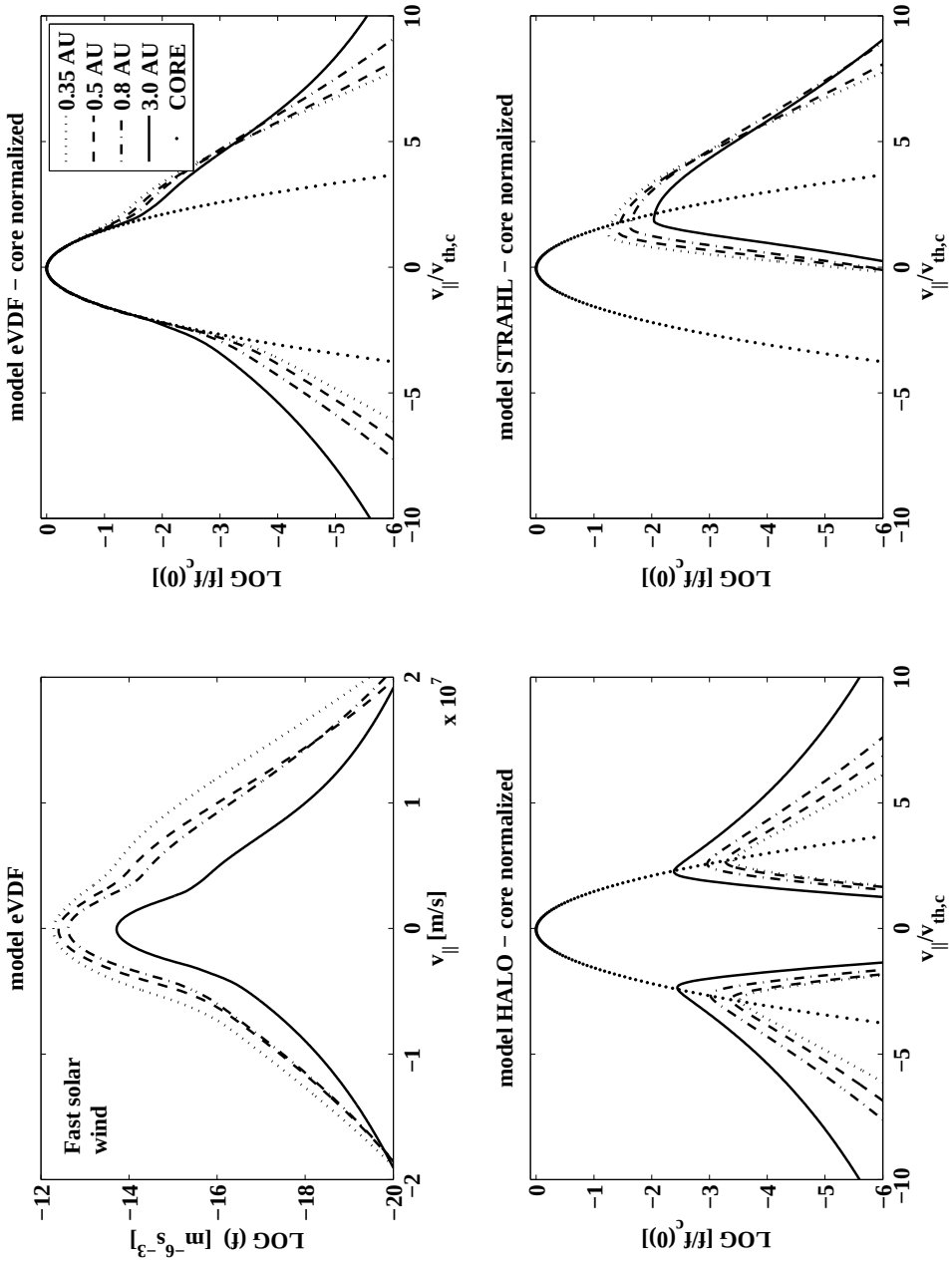

Figure 4.10: (From *Štverák et al.* (2009)) Radial evolution of a model eVDF function in the fast solar wind. Model functions are plotted using average values of all parameters as resulting from the fitting at four different radial distances: 0.35 AU (dotted line), 0.55 AU (dashed line), 0.75 AU (dash-dotted line) and 3 AU (solid line). Except for the upper left panel, the model eVDF functions are normalized in such a way, that the value at the peak equals to unity and the velocity is scaled by $v_{th,c}$. In the lower panels, only the halo and strahl component evolution is compared with the normalized core. With increasing radial distance, the strahl electrons close to the thermal core are scattered while the halo develops stronger tails - slightly stronger than in the slow wind.

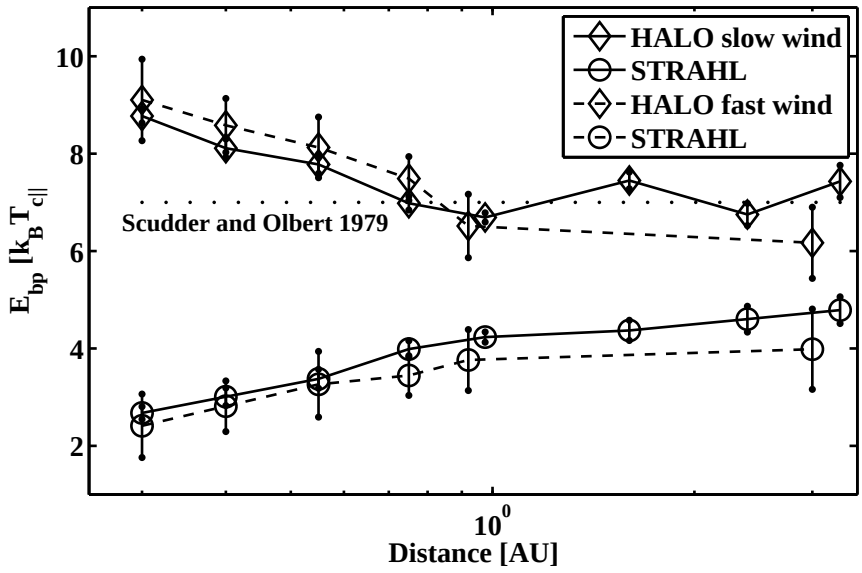

Figure 4.11: (From *Štverák et al.* (2009)) Radial evolution of the break-point energy E_{bp} normalized by $k_B T_{c||}$. The halo break-point energy (dashed line with diamonds) is decreasing and reaching a theoretical limit (dots) around 0.8 AU. In this radial range, no upper limit is reached by the strahl break-point energy (dotted line with circles).

this break-point energy E_{bp} have a minimal local interaction with surroundings and create non-thermal tails of the observed eVDFs. In *Scudder and Olbert* (1979) the authors proposed that the observed eVDF in the solar wind are shaped primarily by Coulomb collisions. They conclude that the effect of Coulomb collisions by itself is sufficient to determine the shape of the eVDFs in both the thermal ($E < kT$) and suprathermal ($E > kT$) energy regimes. Furthermore, they theoretically predicted that the break-point energy scales with local temperature as

$$E_{bp}(r) \approx 7kT_C(r). \tag{4.2}$$

where k is the Boltzmann constant and $T_C(r)$ is the local core electron temperature at the radial distance r.

In this study we define two energy-normalized break points, both in the parallel direction. One is defined in the sunward part of the eVDF: the halo energy break point $E_{bp,h}$, and one in the antisunward direction: the strahl energy break point $E_{bp,s}$. These normalized energies in units of $[kT_{c,||}]$ are given as

$$E_{bp,*} = \frac{mv_{bp,*}^2}{2kT_{c||}} \tag{4.3}$$

where the velocity $v_{bp,*}$ for halo and strahl is determined by

$$\begin{aligned} f_h(v_{bp,h}) &= f_c(v_{bp,h}) \\ f_s(v_{bp,s}) &= f_c(v_{bp,s}) + f_h(v_{bp,s}) \end{aligned} \tag{4.4}$$

respectively. Results from our eVDF analysis are displayed in Figure 4.11. The dashed line with diamonds and the dotted line with circles represent the mean halo and strahl break-point energy, respectively, as a function of the heliocentric radial distance. The error bars of the mean values are expressed by vertical lines. The halo break-point energy slowly decreases with the increasing radial distance reaching the theoretical value of *Scudder and Olbert* (1979) between 0.7 and 0.8 AU. At larger distance it seems that this theoretical value represents a lower constraint, similar results are reported also in *McComas et al.* (1992). An inverse trend is observed for the strahl break-point energy. The strahl break-point energy grows up with increasing radial distance and the slope of this growth is slowly decreasing. However, from this radial interval it is not clear whether the strahl break-point energy has some upper limit smaller than in the case of the halo. That is to say whether the strahl at a certain distance completely disappears or not. Actually, Figure 4.11 describes the radial evolution of competing halo and strahl components already demonstrated in the lower panels of Figures 4.5 and 4.10.

4.4 Charge flux

In the solar wind, both ions and electrons are flowing together in the same direction. In order to maintain the global charge neutrality, no electric currents can exist in such an environment. This means that the ion and electron charge flux through a given area (larger than the Debye radius) has to be equal. If the core and halo components would be flowing with the same velocity as the ions, the strahl electrons would break this equality and produce a non-zero current in the direction parallel with respect to the magnetic field. In order to satisfy the zero-current condition, i.e.

$$v_{bulk,e} n_e = v_{bulk,ion} n_{ion}, \tag{4.5}$$

in our model eVDF we allow not only the strahl drift Δ_s in (3.9) for $v_{||}$ but also a drift of the core Δ_c in (3.3). For the model eVDF in the ion plasma frame the condition (4.5) can be thus rewritten as

$$v_{bulk,c} n_c + v_{bulk,s} n_s = 0. \tag{4.6}$$

During the fitting procedure we do not impose any dependence between Δ_c and Δ_s, both are completely independent. From the result we then compute the core charge flux Φ_c and strahl charge flux Φ_s as

$$\Phi_{c/s} = |v_{bulk,c/s}| n_{c/s} \tag{4.7}$$

According to (4.6), both Φ_c and Φ_s have to be equal. These fluxes are compared in Figure 4.12. Here we plot the correlation between Φ_c and Φ_s separately for all three instruments used in our data set. We compute the mean values of Φ_s in several bins defined over the Φ_c range. Both slow and fast solar wind regimes are mixed in Fig. 4.12 since the zero-current condition has to be valid in any case. For all three instruments, the fluxes are well correlated. However, except $\Phi_c \gtrsim$

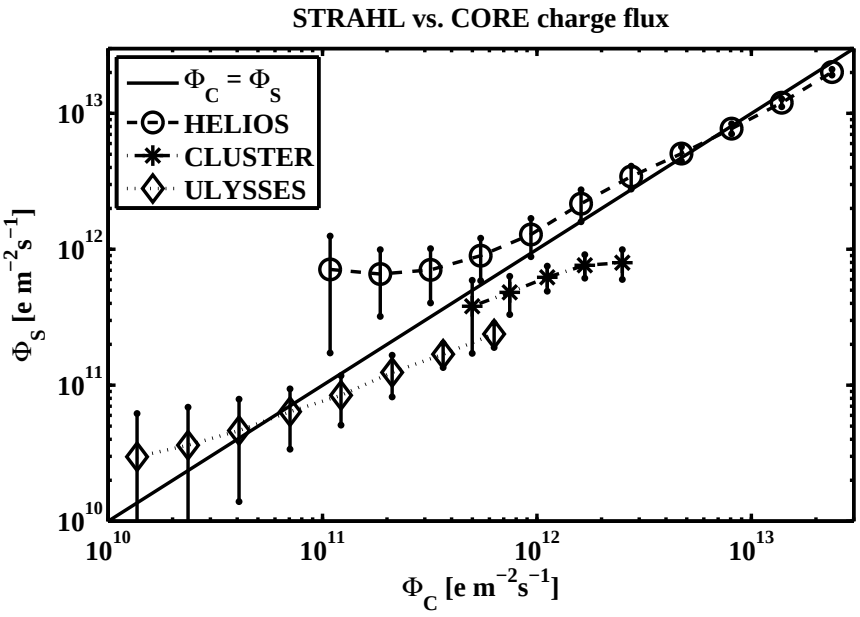

Figure 4.12: (From *Štverák et al.* (2009)) The charge flux of core Φ_c and strahl Φ_s is compared separately for all three spacecraft. We plot the mean values of Φ_s over all eVDF samples in several bins defined over the Φ_c range with circles, stars and diamonds for Helios, Cluster and Ulysses respectively. The fluxes are well correlated for all three instruments. However, namely for Cluster and Ulysses, the correlation slightly deviates from the theoretical zero-current condition $\Phi_c = \Phi_s$. The figure represents all analyzed data samples including observation of both slow and fast solar wind.

$10^{12} e\ m^{-2} s^{-1}$ for Helios spacecraft, the fluxes do not exactly match the theoretical zero-current condition $\Phi_c = \Phi_s$. These discrepancies can result from many reasons. First, one should note that we use as a reference frame the proton bulk speed and that we neglect the alpha particles velocity. We are not therefore in the exact zero-current frame. Second, because of the large electron thermal speeds, the estimation of the drift velocities, namely for the core, can already contain a non-negligible error. Also the estimation of the density itself, especially for the strahl, can be inaccurate as well. Finally we have to take into account different designs of the instruments. For example, in Figure 4.12 we can see larger deviations from the mean values with decreasing charge flux which can be due to limited sensitivity of the individual sensors. All these facts put together make our fitting procedure acceptable corresponding to the zero-current condition and indicate that the strahl charge flux is balanced by the oppositely drifting core.

Finally note that in this case we did not allow any drift for the halo component. If we suppose that the halo drifts together with the core, the halo contribution to the total electron charge flux will be negligible since the core drift is much smaller then the strahl drift while the densities of strahl and halo are comparable. Also

the estimate of the halo drift would be highly inaccurate because of the very large thermal speeds of halo electrons. Therefore an assumption of a non-drifting halo is acceptable. Furthermore, this assumption also makes the model and its analysis less complicated.

Chapter 5

Electron Temperature Anisotropy

In the absence of some mechanisms for interchange of the parallel and perpendicular kinetic energy, the application of the classical CGL relations (*Chew et al.* (1956)) to the solar wind electrons expanding in the spiral structured interplanetary magnetic field predicts large temperature anisotropies. Starting with an isotropic electron distribution close to the Sun, this simple model predicts, for a typical slow solar wind at 1 AU, a temperature ratio between the parallel $T_{||}$ and perpendicular $T_{\perp}$ temperature (the directions are with respect to the ambient magnetic field) of more than 30 (*Phillips and Gosling* (1990)). However, the observed solar wind at this distance is found much closer to the isotropic state with an average $T_{e,||}/T_{e,\perp}$ of 1.2 (*Feldman et al.* (1975) and *Pilipp et al.* (1987b)). In order to explain these observations some physical processes that can effectively transfer the internal kinetic energy of the solar wind electrons from the parallel to the perpendicular directions are needed to counteract the adiabatic expansion and thereby maintain the plasma close to the isotropic state. There are two main kinetic processes able to cause these effects: kinetic plasma instabilities driven by temperature anisotropy itself and Coulomb collisions.

In the present study, we analyse a large number of solar wind eVDFs acquired by three different spacecraft in the low-ecliptic latitudes from 0.3 up to to 4 AU. We estimate the electron temperature anisotropy by fitting of the measured velocity distributions with an analytical model. We fit the core component with the bi-Maxwellian distribution and the halo with a bi-Kappa function. The model and the fitting procedure are described in detail in *Štverák et al.* (2008). In this case, we do not truncate the halo in the thermal regime as it is done for the analysis of the relative densities in chapter 4. Therefore, we obtain directly the second order moments of the eVDFs corresponding to the parallel and perpendicular temperatures directly from the parameters of the analytical model function.

Based on the observations and parameters obtained from the fitted eVDFs, we provide a statistical study of possible constraints imposed on the electron temperature anisotropy by kinetic instabilities and Coulomb collisions. In the case of kinetic instabilities, we examine all the acquired data in terms of temperature anisotropy vs. parallel electron plasma beta which is predicted by the linear dispersion theory to be related to growth rates of unstable modes. Both fitted eVDF components, the

core and the halo, are studied separately. The effect of Coulomb collisions on the electron temperature anisotropy is studied in terms of the electron collisional age A_e defined as the number of collisions suffered by an electron during the expansion of the solar wind. We show that both instabilities and collisions are strongly related to the isotropisation process of the electron core population while the answer to this question for the halo component is still open.

5.1 Kinetic instabilities

The fastest growing modes of electron temperature anisotropy instabilities are the whistler and the fire hose instability (see chapter 2). For the whistler instability and as well for the fire hose instability, *Gary and Wang* (1996) and *Gary and Nishimura* (2003) have shown that the threshold conditions for each of these instabilities, as predicted by the linear dispersion theory, can be written as

$$\frac{T_\perp}{T_{||}} = 1 + \frac{a}{\beta_{||}^b}, \tag{5.1}$$

where the parameter a is positive for the whistler instability and negative for the fire hose and b is always positive. The parameter $\beta_{||} = 2\mu_0 n k_B T_{||}/B^2$ is the electron parallel plasma beta. The equation (5.1) thus represents a relation between the electron temperature anisotropy and the ratio between the particle kinetic and magnetic field pressure. The values we have used in our study for the parameters a and b for the whistler and fire hose instability are given in table 1 of *Gary and Wang* (1996) and table I of *Gary and Nishimura* (2003) respectively.

We compare the curves of constant growth rates of both dominant unstable modes with the electron temperature anisotropy obtained from the fitting process in the $(T_\perp/T_\parallel, \beta_\parallel)$ space. These isocontours of growth rate factors represent in the $(T_\perp/T_\parallel, \beta_\parallel)$ plane threshold conditions of the marginal stability and should thus constrain the observed electron temperature anisotropies.

Results obtained from fitted eVDFs for the thermal core population are shown in Figure 5.1. Results for the slow wind (upper panel) and fast wind (lower panel) are presented separately. For the slow solar wind we consider the samples with electron bulk speed less then 500 km/s and for fast wind we consider samples with bulk speed greater than 600 km/s. The dash-dotted and the dashed line represent the isocontours of growth rates for the whistler and fire hose instability respectively. The counts of the observed ratio between the core perpendicular temperature $T_{c,\perp}$ and parallel temperature $T_{c,||}$ are represented by a logarithmic scale.

The temperature anisotropy of thermal core population in the slow wind seems to be fairly well constrained by instability thresholds predicted by the linear theory because. The core represents the majority of the total electron number density and is well described by a single bi-Maxwellian velocity distribution. A single bi-Maxwellian distribution is also assumed in the theoretical model used in *Gary and Wang* (1996) and *Gary and Nishimura* (2003) to compute the instability thresholds. Namely for higher $\beta_{||}$, the slow wind is well constrained by predicted thresholds of

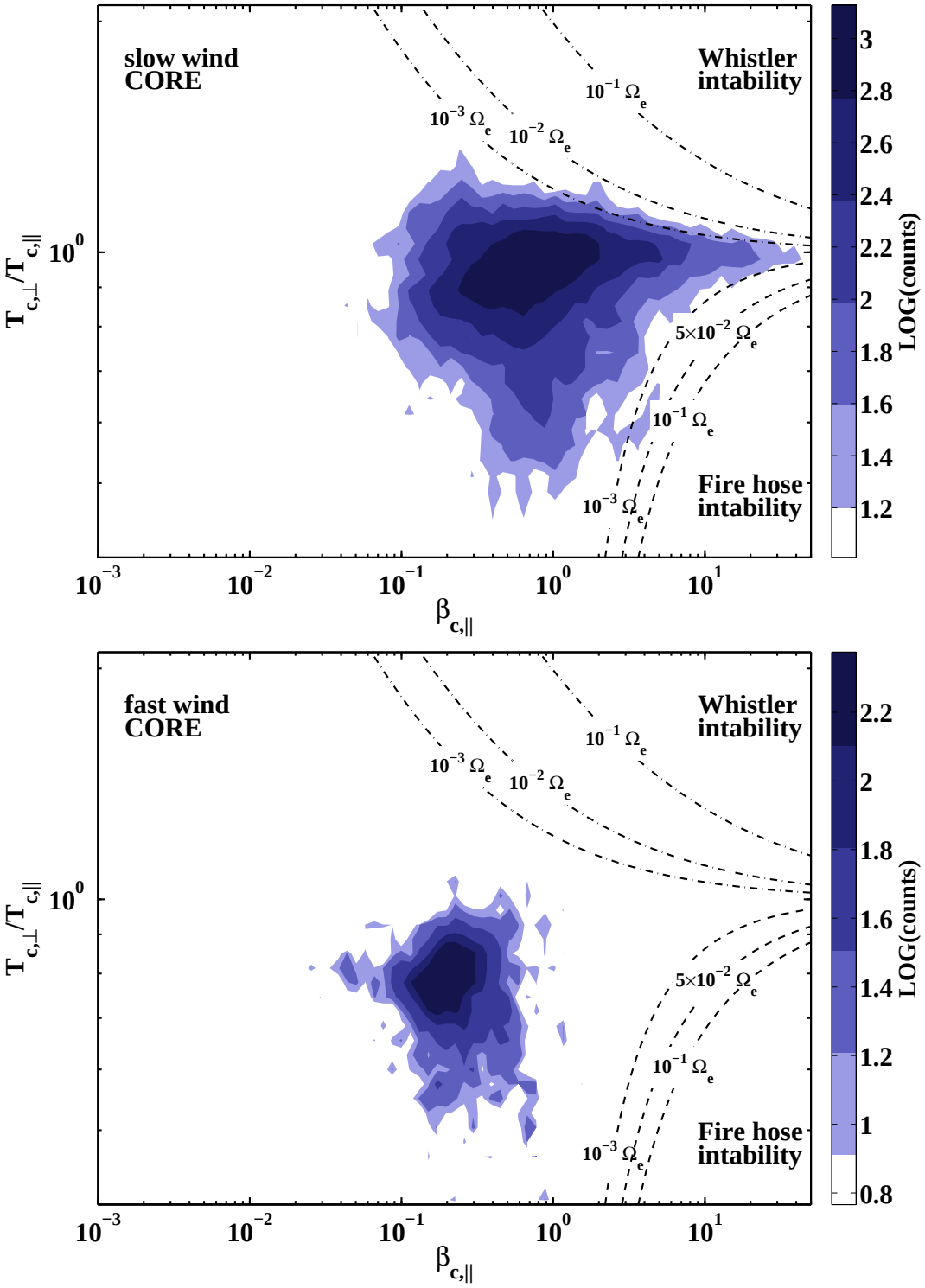

Figure 5.1: (From *Štverák et al.* (2008)) Occurrence rates in our large data set of the temperature anisotropy $T_\perp/T_{||}$ as a function of $\beta_{||}$ for the core population in the slow (upper panel) and fast (lower panel) solar wind. The curves represent the isocontours of growth rates for the whistler (dash-and-dot line) and the fire hose (dashed line) instability.

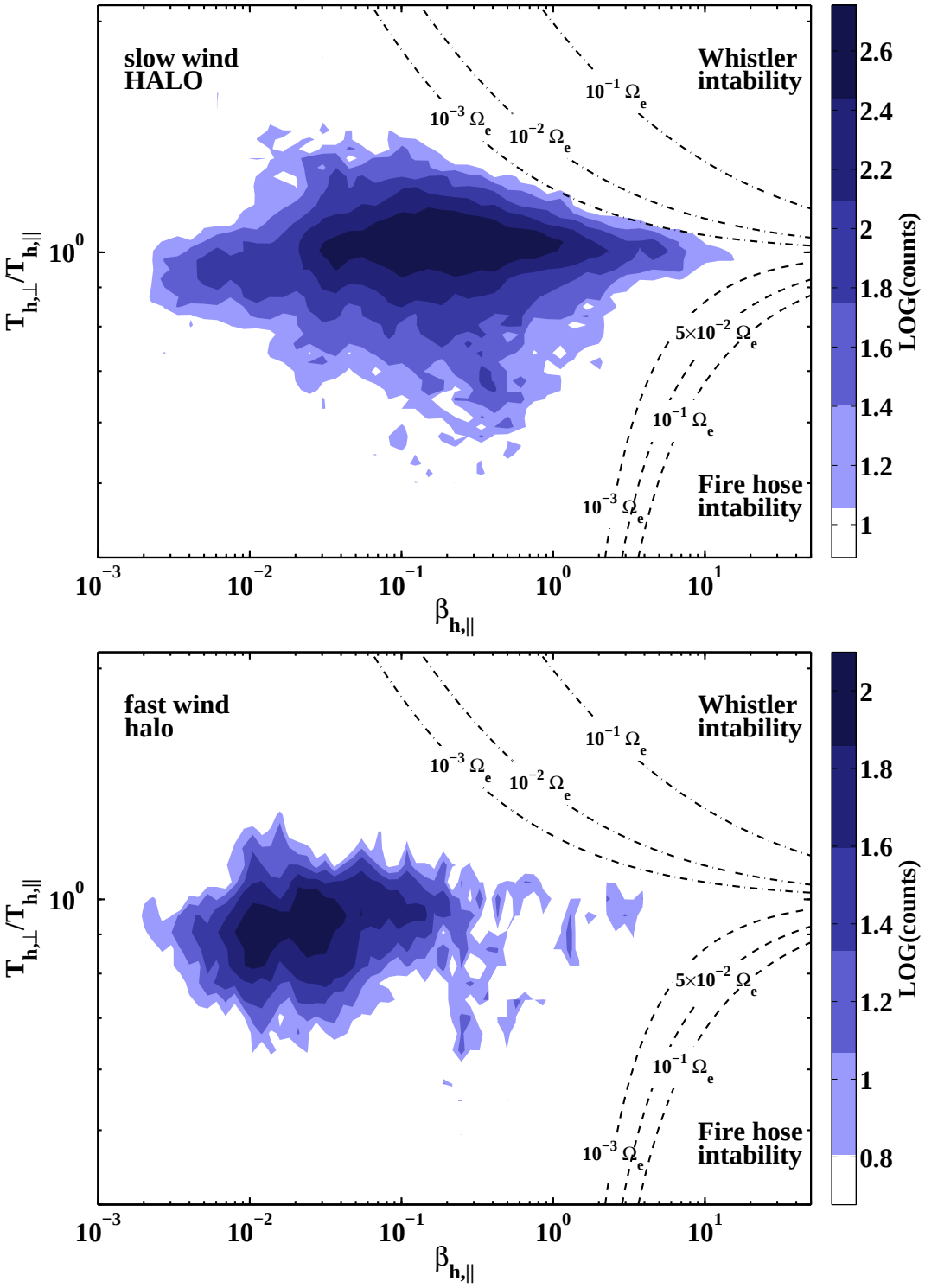

Figure 5.2: (From *Štverák et al.* (2008)) Counts histogram of the $T_\perp/T_{||}$ vs. $\beta_{||}$ from our data set for the halo population in the slow (upper panel) and fast (lower panel) solar wind. The curves represent the contours of constant growth rates for the whistler (dash-and-dot line) and the fire hose (dashed line) instability. Here, the theoretical model does not correspond to the analytical model used for the data analysis.

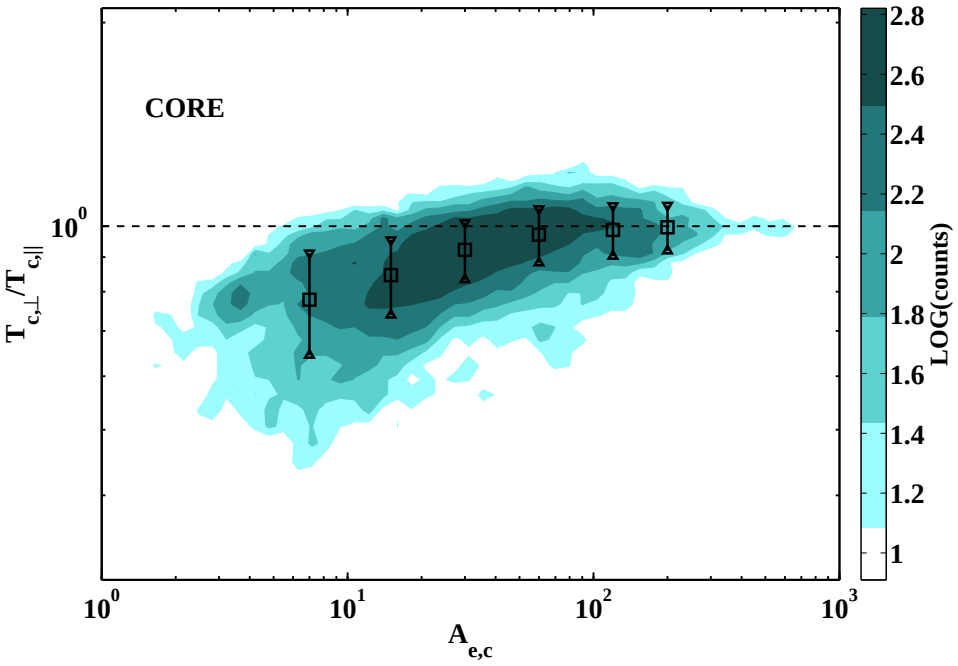

Figure 5.3: (From *Štverák et al.* (2008)) The dependence of the electron temperature anisotropy of the core population on the Coulomb collisions represented by the electron collisional age A_e.

both the whistler and also fire hose instability. For the fire hose instability, there is still a small gap between the observed plasma conditions and the isocontour of even very low growth rate. This little disagreement between observations and predictions of the linear theory can results from the simplified model used in *Gary and Nishimura* (2003). Observed electron distributions in the solar wind exhibit more complicated properties including the supra thermal halo and the strahl populations. These deviations from the simple bi-Maxwellian shape of the velocity distribution could have an influence on the predicted shape of the isocontours of the growth rate factors.

For the core population in the fast solar wind (lower panel of Figure 5.1) the situation is quite different. Here the electron temperature anisotropies are well localized far away from the unstable regions with a mean $T_\perp/T_{||}$ ratio of 0.75 ± 0.15. This can be explained as a consequence of insufficient number of samples in our data set with a electron bulk speed greater than 600 km/s, which we have selected as a lower limit for the fast solar wind or that the instability thresholds have no relevance in the fast wind. The bulk speed condition for the fast solar wind is satisfied for roughly 10% of Helios and Cluster data while it is less then 1% from all the Ulysses samples. From the theory, confirmed by observations, greater anisotropies develop at larger distances from the Sun. The fact that we do not have sufficient amount of data from larger distances from the Sun can be a reason why we do not see any evolution of the electron temperature anisotropy for the fast solar wind in our data set.

	core	*halo*
slow wind	0.5	
fast wind	0.6	0.3

Table 5.1: The power-law decrease of the electron temperature $\propto r^{-\alpha}$ is observed to be different for the slow and the fast solar wind. For the computation of the electron collisional age we have used for the core and halo electron populations values displayed in this table.

Analogous results for the halo population are shown in Figure 5.2. The upper and lower panels show results obtained for the slow and fast solar wind respectively. Note, however, two restrictions in this case. Firstly, the theoretical model used in the linear prediction of the growth rates of the instabilities (bi-Maxwellian) and the analytical model used for the data analysis (bi-Kappa) are different. Secondly, when computing the theoretical predictions for the halo component, we completely neglect the possible effect of the core. One can thus expect disagreement between the results predicted by the theoretical model and the results based on the analysis of real data. The isocontours of growth rate are here plotted mainly for better comparison with figure 5.1. Nevertheless, results obtained for the halo population are similar to results of the core population. We find the observed electron temperature anisotropy fairly constrained by thresholds predicted by the linear theory as in the slow solar wind. For $T_\perp > T_{||}$ the data are almost consistent with the growth rates of the whistler instability predicted for a bi-Maxwellian plasma. In the opposite of $T_\perp > T_{||}$, similar processes to the fire hose instability seem to take an effect. If we would use a bi-Kappa rather than a bi-Maxwellian velocity distribution for the computation of the instability threshold, we could possibly find the result closer to the observations. For the fast wind, we again observe the plasma relatively far from the predicted thresholds in the $(T_\perp/T_{||},\beta_{||})$ plane.

5.2 Coulomb Collisions

In the following we shall examine the effect of Coulomb collisions which also can participate in exchanging of internal kinetic energy between the plasma particles. Since our data were sampled at different radial distances, we have compared the temperature anisotropy with the electron collisional age A_e (*Salem et al.* (2003)). The advantage of expressing the effect of Coulomb collisions by the collisional age is that it does not only take into account the current in situ properties of the plasma but it also in a certain manner reflects the time already spent during the expansion of the solar wind from the corona. The collisional age is obtained by integrating the collision frequency from some initial distance up to location of the measurement. The density and temperature heliospheric gradients are assumed to be given by the power laws r^{-2} and $r^{-\alpha}$ respectively. This computation supposes electrons expanding along open magnetic field lines with a constant flow speed. It

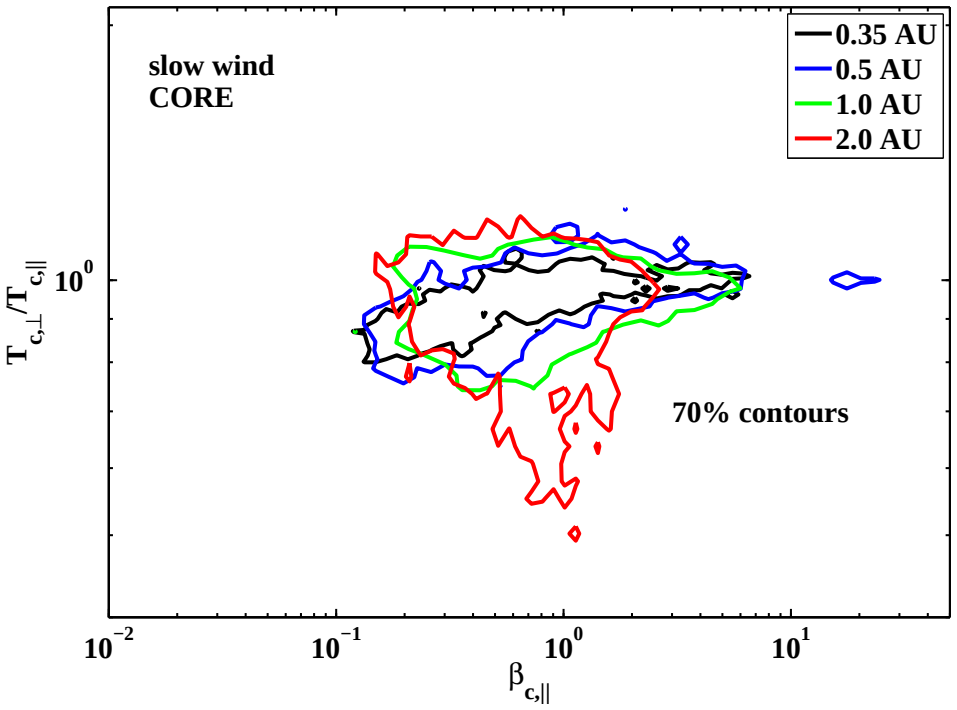

Figure 5.4: (From *Štverák et al.* (2008)) The radial evolution of the core $T_\perp/T_{||}$ vs. $\beta_{||}$ correlation in the slow solar wind. The lines represent contours circumscribing 70% of all samples at a given radial distance.

does not therefore distinguish trapped electrons bouncing back and forth on closed trajectories which already spent more time in the expanding solar wind.

The formula for the electron collisional age reads

$$A_e = \nu_{e\perp} \frac{R}{v_{sw}} \left(\frac{1 - (R/r_0)^{1-1.5\alpha}}{1.5\alpha - 1} \right). \tag{5.2}$$

Here R is the radial distance at which the data sample was acquired, r_0 is the initial distance from which we count the collisions, v_{sw} is the solar wind bulk speed and $\nu_{e\perp}$ represents the total transverse collision frequency of electrons (see *Phillips and Gosling* (1990)) at the place where the data are acquired (thus at the distance R from the Sun). The parameter α in (5.2) depends on the solar wind properties and it varies for the slow and fast wind and also for the core and halo population (see *Issautier et al.* (1998), *Maksimovic et al.* (2000), *Fludra et al.* (1999), *Marsch et al.* (1989)). Because of a large number of various studies published on this topic, we have used some average values from all these results. These values of α are displayed in Table 5.1. The initial distance r_0 was set to 0.2 AU, a small step back from the minimum distance R of our data samples in order to keep the term in the brackets on the right hand side of (5.2) positive.

The correlation between the electron collisional age and the temperature anisotropy of the core population is shown in figure 5.3. All samples are represented by a gray

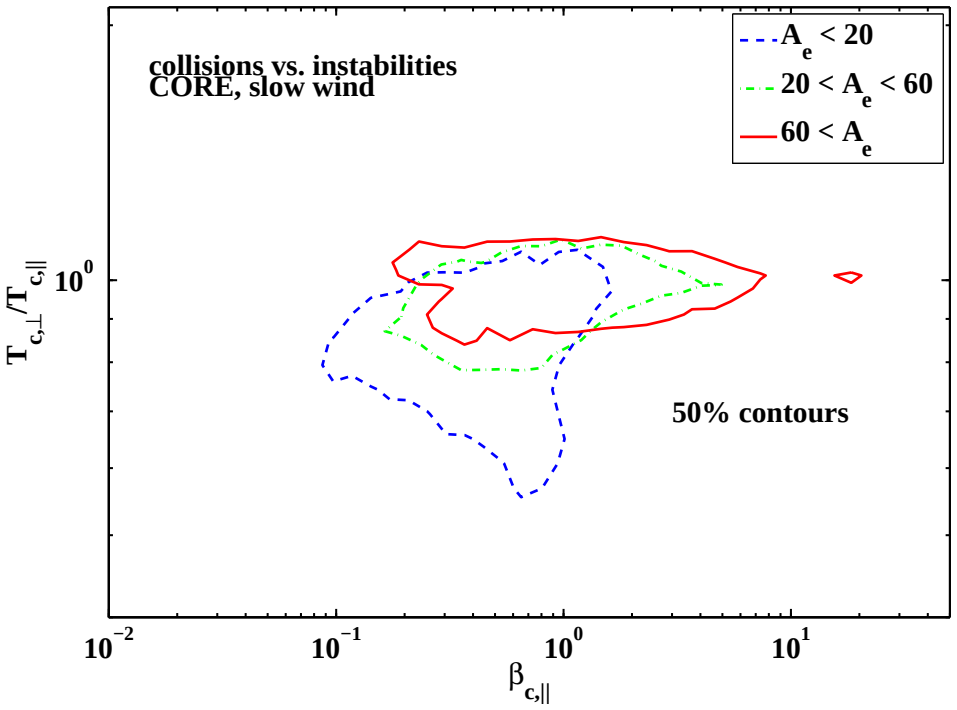

Figure 5.5: (From *Štverák et al.* (2008)) Correlation of electron anisotropy instabilities and electron Coulomb collisions. The electron temperature anisotropy is plotted as a function of the electron parallel plasma beta. All the samples are divided into three bins corresponding to different levels of the electron collisional age.

scale 2D histogram. The results are in good agreement with our expectations and also with previous results of *Phillips et al.* (1989) and *Salem et al.* (2003). With increasing number of collisions, the observed electron distribution functions are closer to the isotropic state. We have also divided the resulting A_e into several bins and computed the corresponding mean collisional age (squares) and the standard deviations (triangle error bars) of the temperature ratio. There is a clearly visible trend of the mean temperature anisotropy tending to 1.0 with increasing number of collisions.

We have also examined the electron temperature anisotropy in the frame of instabilities as a function of the radial distance. According to our expectations based on the theory of the expanding solar wind, higher temperature anisotropies are observed at greater distances with parallel temperature exceeding the perpendicular one. Our data set enables us to examine the relation between the electron temperature anisotropy and the parallel plasma beta as a function of the increasing radial distance from 0.3 AU up to almost 4 AU. The radial evolution is presented (for the core population only) in figure 5.4. The lines represent contours circumscribing 70% of all samples at a given radial distance. No visible path in the $(T_\perp/T_{||}, \beta_{||})$ plane can be clearly seen. Only a gentle spreading of the temperature anisotropy with increasing distance can be noticed. Since our statistics for the fast solar wind is

insufficient, it is more difficult to perform such an analysis in this case.

We have shown that both, the instabilities as well as the Coulomb collisions, can influence the temperature anisotropy of the solar wind electrons. The final question is whether these effects act independently or are somehow correlated. In general higher plasma beta implies more collisions but nearly isotropic electron distributions are also observed for lower beta. Actually these isotropic distributions with low beta are a consequence of the Coulomb collisions rather than instabilities. This correlation of instabilities and collisions is demonstrated in Figure 5.5. On this figure all the samples are divided into three bins corresponding to different levels of the electron collisional age. For the bin where collisional age A_e is greater than 60, we find only nearly isotropic electron distributions not only at high electron parallel plasma beta but as well at low values of this parameter. Here the instabilities do not play any role, or are very weak, thus electrons have most likely been isotropized mainly via collisions. The figure 5.5 gives another important result. While there was no clear correlation between the temperature anisotropy in the parallel beta frame with increasing radial distance (figure 5.4), we can see a nice trend with increasing number of collisions. Instead of a radial trend we may rather speak of a collisional evolution of the temperature anisotropy for the solar wind electrons.

Chapter 6

Electron Heat flux in the Solar Wind

The heat flux is a fundamental quantity in the solar wind. It is the consequence of mechanisms which transport the energy from the hot solar source to the cold outer heliosphere. In particular, the way the heat is transported is probably strongly linked to the way how the wind is accelerated and heated. A complete understanding of the solar wind would thus require a thorough understanding of how the heat flux evolves and how it is controlled during the whole process of the solar wind expansion. However, this energy flow and the associated issue of the solar wind heating are still not well understood.

In the solar corona, the heat flux required to produce the observed solar wind (see e.g. *Meyer-Vernet* (2007)) is estimated to values which are greater than it can be provided by the collisional electron heat flux given by (1.20) as

$$Q_{e,col} = -\kappa_e \nabla T_e(r).$$

On the other hand, already early observations (*Montgomery et al.* (1968), *Hundhausen* (1969) or *Hollweg* (1974)) have shown that in the solar wind near 1 AU the heat flux is significantly smaller than predicted by *Spitzer and Härm* (1953). Since the theory based on the effect of frequent Coulomb collisions can not explain the observations, a kinetic treatment, i.e. a detailed study of VDFs, is needed to correctly describe the true mechanism transporting the heat from the corona out to the whole heliosphere.

The bulk of the solar wind heat flux is transported by electrons (*Feldman et al.* (1975)) and is observed to flow along the local background magnetic field (e.g. *Scime et al.* (1994a)). From the kinetic point of view, the heat flux is produced by the skewness of observed eVDFs represented by the strahl component. We present an observational study of the heat flux properties based on our large data set which combines measured eVDFs from three spacecraft. The measured eVDFs are fitted with the 3-component model described in chapter 3 where all three components are described by fully analytical forms. The heat flux is then estimated by numerical integration of the model distribution functions, performed for each component, namely the core, the halo and the strahl, separately. Resulting estimations of the

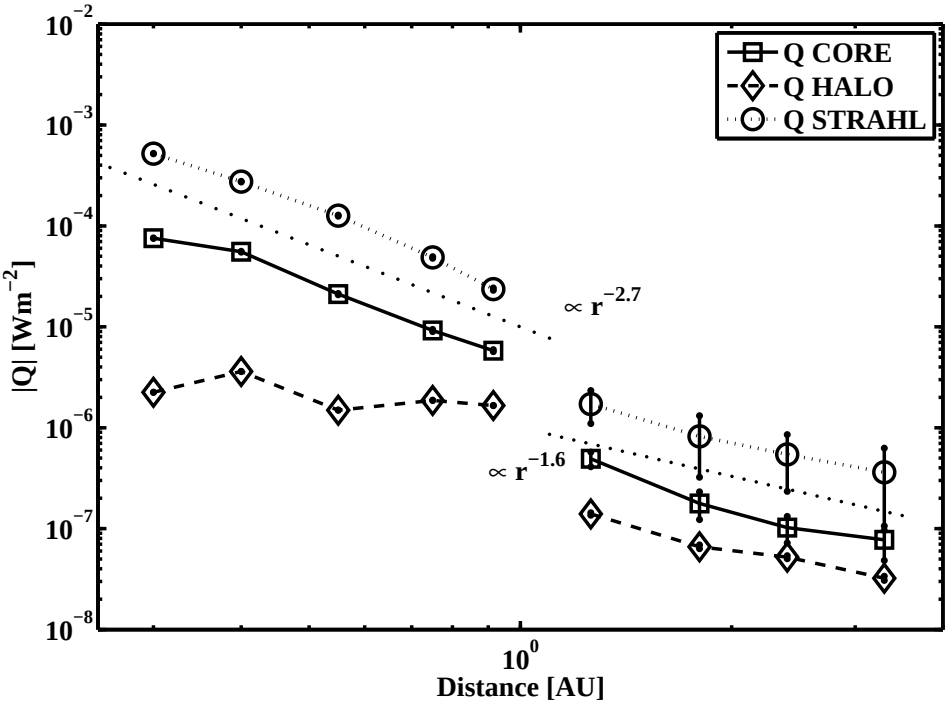

Figure 6.1: The observed radial evolution of average absolute electron heat fluxes as result from our analysis of the large eVDF data set. We plot the partial heat flux of the core (squares), halo (diamonds), and strahl (circles) as a function of the radial distance from Sun. Note that the core and halo electron heat fluxes represent a negative contributions to the total electron heat flux. Dotted lines represent the empirical power law for the strahl heat flux as derived from our analysis.

heat flux should thus be more precise than a direct discrete integration of measured eVDFs. In this chapter we present the observed radial evolution of the electron heat flux throughout the solar wind expansion from 0.3 up to 4 AU. Consequently, we examine some possible theoretical constraints imposed on the solar wind heat flux by wave-particle interactions and Coulomb collisions.

We use an analytical model in which two components, the core and the halo, may be drifting in the plasma rest frame along the magnetic field in the sunward direction (Q negative), while an antisunward drift is imposed on the strahl component (Q positive). The heat flux for each of the three components is calculated in the rest frame of the whole distribution function, therefore, the total electron heat flux equals to

$$Q_{tot} = Q_c + Q_h + Q_s = Q_s - |Q_c| - |Q_h| \tag{6.1}$$

where Q_c, Q_h and Q_s are partial heat fluxes of the core, halo, and strahl respectively. Since the drift of the core is typically much smaller than the drift of the strahl, the core and particularly the halo sunward oriented heat flux are expected to be much smaller than the antisunward oriented heat flux of the strahl.

$Q \propto r^{\alpha}$	**Core**	**Halo**	**Strahl**	**Total**
$r < 1AU$	-2.43 ± 0.12	-0.45 ± 0.24	-2.75 ± 0.10	-2.90 ± 0.13
$r > 1AU$	-1.93 ± 0.14	-1.47 ± 0.07	-1.61 ± 0.06	-1.51 ± 0.03

Table 6.1: List of power law gradients as deduced from our large data set by fitting of the measured eVDFs to the proposed analytical model. Exponents α of the empirical power law $Q \propto r^{\alpha}$ are listed for the core, halo and strahl components and for the total electron heat flux for samples acquired in radial distance r from the Sun below and above 1 AU respectively.

6.1 Radial Evolution

In the classical collisional theory for the energy transport in plasmas the heat flows against the local temperature gradient as given by equation (1.20). The magnitude of the heat flux further depends on the thermal conductivity κ_{col} of the transport medium represented by electrons. The electron thermal conductivity depends on the electron temperature as

$$\kappa_{e,col} \propto T_e^{5/2} \tag{6.2}$$

while it is almost independent on the electron density[1] (*Spitzer and Härm* (1953)). For a radially expanding general polytrope flow ($p \propto \rho^{\gamma}$), the radial profile of the polytropic temperature is given by (1.17). Substituting (6.2) and (1.17) into (1.20), we find the theoretical collisional heat flux to decrease with the heliocentric radial distance r as

$$Q_{e,col} \propto Q_0 r^{-7\gamma+6} \tag{6.3}$$

thus for the adiabatic and isothermal flow we have $Q_{e,col} \propto r^{-17/3}$ and $Q_{e,col} \propto r^{-1}$ respectively. Note that for the isothermal case, Q_0 will in fact limit to zero. In order to have a non-zero isothermal heat flux, we have to assume that the thermal conductivity depends also on the polytropic index as $\kappa_e \propto 1/(\gamma - 1)$. However, the thermal conductivity derived in *Spitzer and Härm* (1953) is independent on the polytropic index.

Since the heat flows along the magnetic field lines, the radial expansion is valid only up to a limited distance. Assuming the model of *Parker* (1963) for the IMF, *Scime et al.* (1994a) derived that the radial gradient in (1.20) should be replaced by

$$\nabla = \left(1 + \left(\frac{r\omega}{v_{sw}}\right)^2\right)^{-1/2} \nabla_r \tag{6.4}$$

where ω is the angular speed of the Sun's rotation and v_{sw} is the solar wind speed. Therefore, at a larger radial distance r the heat flux profile given in (6.3) will change to

$$Q_{e,col} \propto r^{-7\gamma+5} \tag{6.5}$$

[1] In fact, the thermal conductivity depends on the density only indirectly through the Coulomb logarithm which variation in the solar wind plasmas is very small and is thus usually considered to be constant.

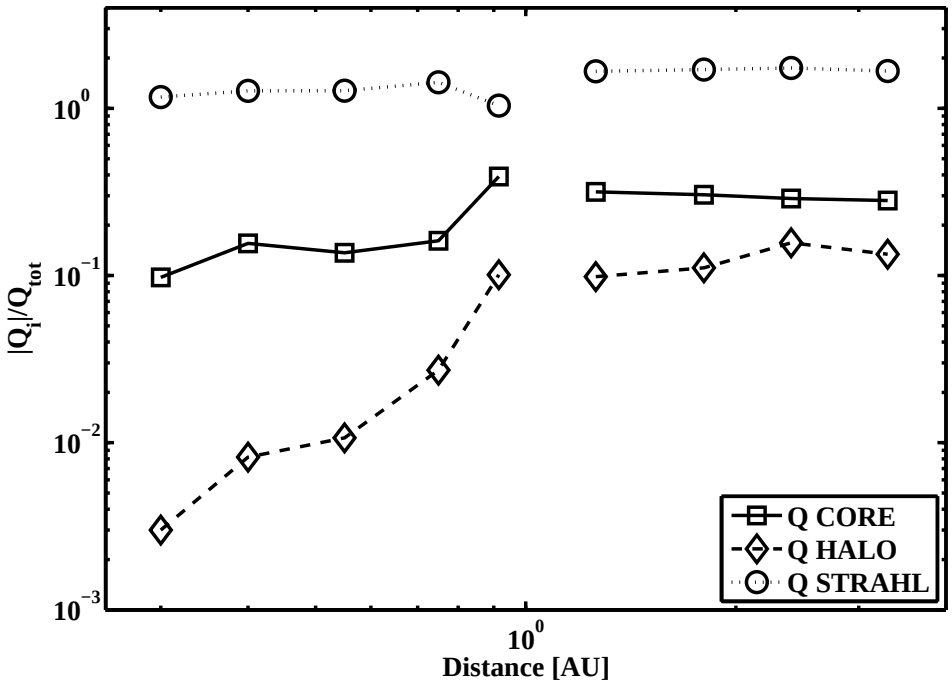

Figure 6.2: Radial evolution of average partial electron heat fluxes of the core (squares), halo (diamonds) and strahl (circles) normalized to the total electron heat flux Q_{tot} plotted as a function of the heliocentric radial distance. As expected, the most important for the overall electron heat flux is the strahl component while the smallest portion in our model represents the heat flux of the halo component.

The adiabatic expansion ($\gamma = 5/3$) thus predicts a radial scaling of the collisional heat flux to be $Q_e \propto r^{-17/3}$ and to have even steeper gradient, $Q_e \propto r^{-20/3}$, at larger distance. However, as already indicated, for instance, by the observed temperature gradients, the solar wind expansion can not be described as an ideal adiabatic process. And, indeed, also the observations of the radial scaling of the electron heat flux indicate a different power law from the one predicted for the adiabatic expansion. Based on the Helios and Ulysses observations, *Pilipp et al.* (1990) and *Scime et al.* (1994a) found the electron heat flux that decreases with the heliocentric distance slower, namely as $Q_e \propto r^{-3}$. Obviously, the observed radial profile of Q_e is neither in agreement with the adiabatic expansion but nor with theoretical predictions for a freely expanding quantity along the spiral oriented magnetic field lines (*Scime et al.* (1994a)).

The observed radial evolution of the average electron heat flux as it results from our analysis of the large eVDF data set is summarized in Figure 6.1 for all three eVDF components. The squares, diamonds and circles represent mean absolute values of the core, halo and strahl partial heat fluxes respectively. Two dotted lines indicate the radial evolution as suggested by a deduced empirical power law using the data for the strahl heat flux. A complete list of all observed power laws for the three components and for the total electron heat flux is given in Table 6.1. For

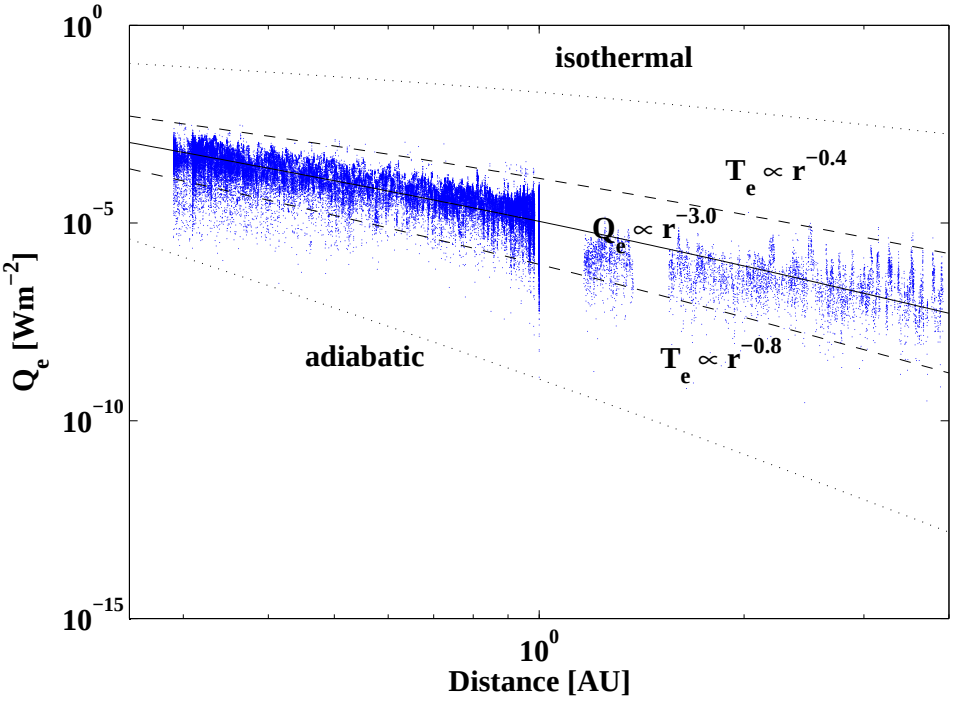

Figure 6.3: The radial evolution of the total electron heat flux as observed from our data set (blue dots) is compared with five theoretical profiles which are computed for different values of the electron temperature gradient using a general form of the collisional heat flux. It seems that the observed heat flux as a function of the radial distance is driven by the local temperature gradient.

observations below 1 AU the results are consistent with those of *Pilipp et al.* (1990). However, the analysis of data samples above 1 AU gives a less steep gradient than it was observed by *Scime et al.* (1994a). Furthermore, mean heat fluxes seem to be slightly inconsistent with each other when crossing 1 AU. It is likely caused by different calibration or interpretation of data acquired on board Helios and Ulysses spacecraft. However, there is no clear reasonable explanation for this observed disagreement between the Helios and Ulysses observations.

We further compare all three partial heat fluxes of the three components to the total heat flux (6.1). Corresponding results are plotted in Figure 6.2. Here the three symbols (squares, diamonds and circles) represent the same components as in Figure 6.1, i.e. the core, halo and strahl respectively. All three ratios of the partial heat fluxes to the total electron heat flux are again displayed as a function of the heliocentric distance r. As expected, in our model the least important for the overall heat flux is the halo component, although the relative heat flux of the halo reaches about 10% at the upper limit of the observed radial range. Naturally, the most important portion of the total heat flux represents the heat transported by the strahl component. The positive strahl heat flux is then partly balanced with the negative sunward oriented heat flux of the core component which builds only

about 10% of Q_{tot} close to the Sun (about 0.3 AU) but can reach up to about 30% at larger distances. In general, increasing relative sunward heat fluxes associated with the core and the halo as well as the increasing heat flux associated with the strahl indicates an increasing separation (relative drift) of the core and halo with respect to the strahl in the solar wind rest frame.

Finally, we examine the total electron heat flux, i.e., the sum of partial heat fluxes of the core, halo and strahl components, with respect to the theoretically predicted radial distance dependency of the classical collisional transport of the heat. Following equations (6.3) and (6.4), we use a general form of the theoretical heat flux given as

$$Q_{e,col} = Q_0 r^{-\alpha} \left(1 + \left(\frac{r\omega}{v_{sw}}\right)^2\right)^{-1/2} \tag{6.6}$$

to compute consecutively five radial profiles based on different temperature gradients. These are namely the adiabatic and isothermal limits, heat fluxes for the two typical limits of the observed temperature gradients ($T_e \propto r^{-0.4}$ and $T_e \propto r^{-0.8}$) and finally the empirical heat flux profile which behaves close to the Sun as $Q_e \propto r^{-3.0}$. All profiles are normalized by Q_0 so that each of them is equal to 1 Wm^{-2} at 5 R_S above the surface of the photosphere. In Figure 6.3 we overplot these five radial profiles over the observed total electron heat flux (blue dots), as it was estimated from the fitting of the analytical eVDF model to measured eVDFs. Obviously, the observed radial evolution of the electron heat flux seems to be well constrained by the two theoretical profiles computed for the two limits of the typical temperature gradients. The radial profile observed by *Pilipp et al.* (1990) and *Scime et al.* (1994a) is well correlated with our observations namely in the Helios radial range. The most important conclusion from Figure 6.3 is following. Although the observed electron heat flux in the solar wind does not reach the theoretical limit of *Spitzer and Härm* (1953), it still seems to be driven by the local temperature gradient and can be thus expressed in a form similar to (1.20) with an appropriate term for the heat conductivity.

6.2 Regulation of Electron Heat Flux

Observations in the solar wind show the electron heat flux to be typically smaller than the predicted one by *Spitzer and Härm* (1953). The lower values of the observed heat flux are addressed to the limited effect of the Coulomb collisions. The magnitude of the electron heat flux seems to reach rather another upper bound which value is given only by local plasma parameters. As we have shown in the previous section, the decrease of Q_e with radial distance can be related to the slower decrease of the electron temperature which implies an electron heating in addition to the adiabatic cooling of the expanding plasma. As for the temperature anisotropies, there is one candidate which can drive the heat flux through the solar wind expansion and transfer the energy to particles reducing the effect of the adiabatic cooling. Kinetic plasma instabilities represent the most plausible mechanism. In addition,

the observed upper bound of the solar wind heat flux is still expected to depend on the local frequency of Coulomb collisions. In this paragraph we examine the possible effect of both kinetic instabilities and Coulomb collisions on the electron heat flux derived from our data set.

The electron heat flux, i.e. the skewness of the eVDF along the magnetic field, represents by itself a source of free energy which may give rise to several unstable wave modes. *Gary et al.* (1975) derived from the linear dispersion theory three unstable modes, namely modes corresponding to the Alfvén, magnetosonic and whistler heat flux instabilities, and found that the whistler heat flux instability has the lowest threshold in the typically observed range of electron parallel plasma beta of the core electron population ($\beta_{c,||} = 2\mu_0 n_c k_B T_{c,||}/B^2$). For isotropic core and halo populations, *Gary et al.* (1994) showed that the threshold for the whistler heat flux instability has the following form

$$\frac{Q_e}{Q_{max}} = \frac{a}{\beta_{c,||}^b} \tag{6.7}$$

where a and b are fitting parameters and

$$Q_{max} = \frac{3}{2} m_e n_e v_{the,c}^3 \tag{6.8}$$

is the free-streaming heat flux (*Hundhausen* (1972)) defined as the internal kinetic energy convected at the parallel thermal speed of the core $v_{the,c} = \sqrt{k_B T_{c,||}/m_e}$. *Gary et al.* (1999) numerically solved the threshold condition for the mean values of the observed solar wind parameters. Consequently, the $\beta_{c,||}$-dependent expression (6.7) was used to fit the isocontour of the constant growth rate factor $\gamma = 10^{-2}\Omega_p$, where Ω_p is the proton cyclotron frequency. The median values of fitting parameters a and b yielded

$$a = 1.0\ , \quad b = 0.8 \tag{6.9}$$

for $0.1 < \beta_{c,||} < 5.0$. In addition, *Gary et al.* (1999) presented an observational evidence that (6.7) with (6.9) can correspond to an upper bound on the solar wind heat flux.

In Figure 6.4 we compare the findings of *Gary et al.* (1999) expressed in (6.7) with the total electron heat flux computed on our data set. The color scale histogram displays the observed heat flux normalized by (6.8) as functions of $\beta_{c,||}$ and the blue line represents the threshold condition (6.7) with the fitting parameters given by (6.9). The Figure 6.4 is completed with an empirical threshold (dashed line) which represents a true upper bound for our observations. The observed normalized heat flux is not completely constrained by predictions of *Gary et al.* (1999). However, *Gary et al.* (1999) used a different eVDF model than we use for our analysis. The core was described also by a single bi-Maxwellian distribution but the halo together with the strahl were modeled by one drifting bi-Maxwellian distribution function producing the heatflux. On the other hand, the empirical threshold found in our data set has the same parameter $b = 0.8$ as given in (6.9). The different parameter a found empirically in our data set could be caused by the normalization which was

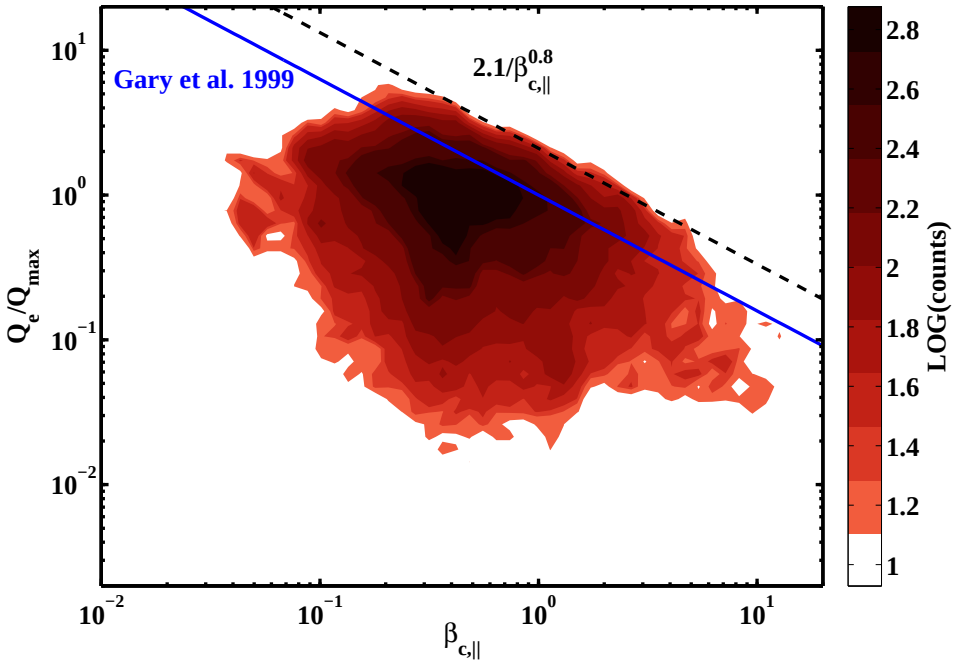

Figure 6.4: The whistler heat flux instability impose on the normalized heat flux a possible upper bound in the (Q_e/Q_{max},$\beta_{c,||}$) space. The observed upper bound (dashed line) is found slightly above the one predicted by the linear theory for a given growth rate of the unstable mode (blue line). However, the observed upper bound has the same form as the theoretical one.

computed from our data set, or by the fact that this constraint may be provided by a plasma mode other than the whistler heat flux instability. In general we conclude from Figure 6.4 that a heat flux instability may represent a significant constraint on the solar wind heat flux. However, the exact threshold conditions imposed on the normalized heat flux, probably not only by this type of kinetic instability, should be further investigated.

In order to quantify the role of Coulomb collisions on the overall transport of the heat in the expanding solar wind, we compere the total electron heat flux (6.1) as estimated from our data set normalized to the collisional heat flux of *Spitzer and Härm* (1953) with the theoretical electron-electron collision frequency ν_{ee}. While the relaxation of the temperature anisotropy is related to temporal evolution, the heat flux should depend rather on local parameters. Therefore we do not use the concept of the electron collisional age which we have applied in the study of electron temperature anisotropies but rather the electron-electron collision frequency. The formula for the electron-electron collision frequency was originally derived in *Spitzer* (1956) and can be approximated as

$$\nu_{ee} \simeq 2.9 \times 10^{-6} n_e T_e^{-3/2} \ln \Lambda \quad s^{-1} \tag{6.10}$$

where the electron density n_e is given in cm^{-3} and the electron temperature T_e in eV, $\ln \Lambda$ is the Coulomb logarithm. The collisional heat flux Q_{SH} is computed from

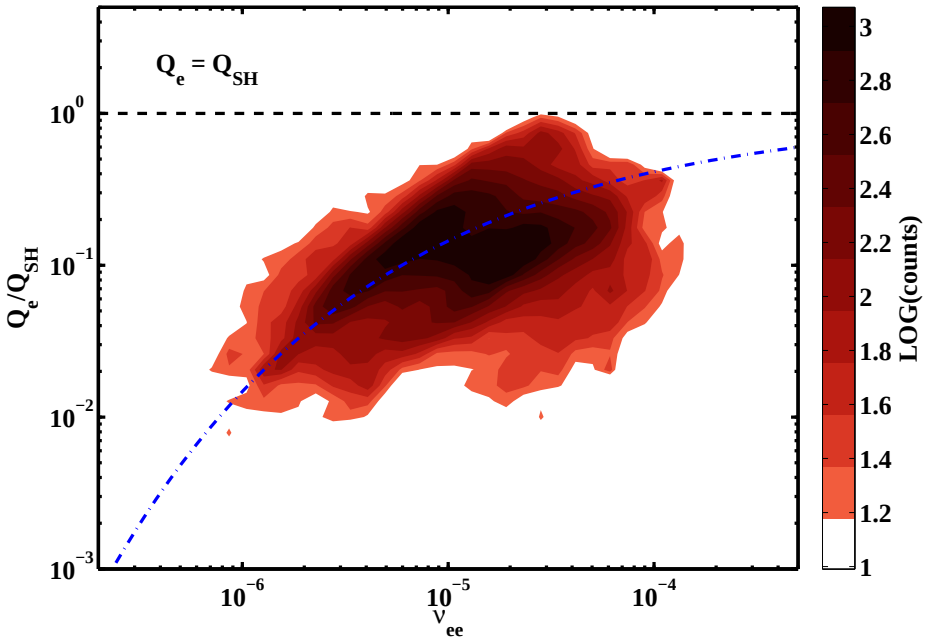

Figure 6.5: Electron heat flux Q_e estimated from our data set and normalized to the collisional heat flux Q_{SH} predicted by *Spitzer and Härm* (1953) as a function of the electron-electron collisional frequency. The theoretical limit is not reached in the solar wind. However, the heat flux is fouind closer to this limit with increasing collision frequency (as indicated by the blue dashed line).

(1.20) assuming an empirical radial profile of the electron temperature decreasing with the radial distance r as $T_e \propto r^{-0.7}$ which is similar to what we observe in our data set in the slow solar wind for the core component (see Fig. 4.3).

The correlation between the observed electron heat flux Q_e normalized by Q_{SH} and the electron-electron collision frequency ν_{ee} is shown in Figure 6.5. The color scale represents histogram of all eVDF samples in the (Q_e/Q_{SH},ν_{ee}) plane and the blue dash-dotted line shows an empirical trend of the of the Q_e/Q_{SH} as a function of the electron-electron collision frequency. As expected, the observed electron heat flux in the solar wind does not reach the theoretical collisional heat flux. However, it is approaching closer to the Q_{SH} limit with increasing frequency of electron collisions. Coulomb collisions thus seem to be one of the mechanism which regulate the overall transport of the heat, even their effect in the solar wind is limited. These conclusions are consistent with *Salem et al.* (2003) where authors have examined the solar wind heat flux in terms of the Knudsen number which was defined through the empirical temperature gradient. *Salem et al.* (2003) also showed that the observed heat flux is closer to the collisional one when Coulomb collisions become more important, i.e., when the Knudsen number is sufficiently smaller than one.

Chapter 7

Conclusions and Perspectives

We have performed a statistical study of a substantial amount of solar wind electron velocity distribution functions (eVDFs). The large data set combines measured eVDF samples acquired *in situ* on board different spacecraft, namely Helios I&II, Cluster II and Ulysses, in the low ecliptic latitudes. Altogether, eVDF samples in the data set cover the radial heliocentric distance from 0.3 up to 4 AU. The aim of the present study was *(i)* to propose and validate an analytical model to fit separately for the first time all three components of the solar wind eVDFs (i.e. the core, the halo and the strahl) which are typically observed; *(ii)* to apply the proposed analytical model on the whole eVDF data set and provide the radial evolution of the main characteristics of solar wind electrons; *(iii)* to study the non-thermal character of the high-energy eVDF tails; and *(iv)* to examine the possible constraints imposed on electron temperature anisotropies and on the overall electron heat flux by the wave-particle interactions and Coulomb collisions.

The proposed analytical form of the eVDF model comprises a bi-Maxwellian distribution for the core and modified bi-Kappa distributions for the halo and strahl respectively. One of the main properties of the new model is to fit the thermal and the non-thermal part of the observed eVDF separately since halo and strahl components are truncated in the thermal velocity range of the core. The model was applied on a large data set of eVDF samples and was shown to be convenient to fit the observed eVDFs in the whole heliocentric radial range. Electron characteristics, namely the density, the temperature and the heat flux, were estimated either directly from the fitting parameters of the model eVDF (electron temperature anisotropies) or by the numerical integration of the fitted eVDFs (the eVDF radial evolution.and electron heat flux). The radial evolution of eVDFs was examined for the slow wind and for the fast solar wind separately. It is important to note that all conclusions concerning the fast wind case have to be taken with caution since only about 10% of the total number of all eVDF samples (and even less per cent above 1 AU) represent the fast solar wind regime.

7.1 Radial Evolution

The radial evolution of solar wind electrons was first focused on electron densities and temperatures. All three eVDF components were analysed separately and compared to each other. The decrease of th electron density of the core was shown to follow the law of a steady radial expansion. The radial evolution of halo and strahl densities was found more complex and neither agreed to the observed power law of the core nor to a steady expansion along the spiral oriented magnetic field lines. The cooling of the electron temperature caused by the solar wind expansion is observed to be highly variable. We have found the core parallel temperature to decrease as $\propto r^{-0.7}$ in the slow solar wind and to decrease slightly slower as $\propto r^{-0.55}$ in the fast solar wind. These findings are in the range of observed temperature gradients already presented in many previous studies. Although we present the radial evolution of halo and strahl temperatures, note that they have to be perceived rather as the corresponding second order moments of the model functions.

The non-thermal character of the observed eVDFs was examined through relative densities of the three eVDF components as a function of the radial distance from the Sun. We have shown that with increasing radial distance the relative density of the strahl decreases while the relative density of the halo increases, for both the slow fast solar wind regimes. For the slow wind, the total relative density of the non-thermal electrons, i.e. the sum of the halo and the strahl, remains almost constant in the whole observed radial range. The ratio of non-thermal electrons in the slow wind is found to be about 5-7%. In the fast wind the relative density of non-thermal electrons is more variable and grows up to about 10% close to 1 AU. The relative density of non-thermal electrons in the fast solar wind seems to be slightly higher compared to the slow wind. This can be caused by typically lower densities observed in the fast wind, which makes the effect of Coulomb collisions less effective. The relatively stronger non-thermal eVDF tails in the fast wind can be, however, attributed to the slightly steeper gradient of the core density with respect to the slow wind case.

As another characteristic which can quantity character of non-thermal eVDF tails, we have examined the κ parameter of model functions used to fit the halo and strahl components. κ is decreasing with increasing radial distance from Sun for both the halo and the strahl. This indicates that deflections of non-thermal tails of eVDFs from the bi-Maxwellian core rise further from the Sun. In the slow wind the κ halo starts at 0.3 AU with a value of roughly 9.5 while in the fast wind the κ parameter is already less than 7. This shows that the fast wind has already more important non-thermal tails close to the Sun compared to the slow one (*Pilipp et al.* (1987a,b)). Smallest values, with a lower limit of 2, are observed at the largest radial distances. For the halo component in the fast wind, our results are again in fair agreement with *Maksimovic et al.* (2005) (see the lower left panel in Fig. 5 of the concerned paper).

In order to summarize how the shape of observed eVDFs changes with increasing radial distance from Sun, we have also displayed the radial evolution of a mean model function, that is a model function computed from mean values of all its parameters.

In general our results are in agreement with those reported by *Maksimovic et al.* (2005) where only the fast solar wind was examined. Our results also support the scenario proposed by several authors (see *Gary et al.* (1994), *Vocks et al.* (2005), *Gary and Saito* (2007), *Saito and Gary* (2007)) of strahl electrons being scattered into the halo. Adopting the scattering mechanisms, the observed radial evolution of non-thermal eVDF components likewise agrees with the numerical modeling of *Owens et al.* (2008) describing the expansion of non-thermal electrons on a background of spiral oriented magnetic field.

We have also analysed the break-point energy, i.e. the limit energy where the non-thermal tails start to deviate from the Maxwellian core. The halo break-point energy normalized to the thermal energy of the core population was shown to approach with increasing radial distance the theoretical limit predicted by *Scudder and Olbert* (1979). Furthermore, we have examined the agreement between relative velocity drifts of the eVDF components in the rest frame of the solar wind and the zero-current condition. We found the sunward electron flux approximately equal to the oppositely oriented antisunward flux of the strahl component.

In addition to the results provided in this paper, we can make a prediction concerning the properties of a eVDF outside the observed radial range. This prediction holds for both solar wind regimes, the slow one and the fast one. The more interesting edge of the interval, regarding the initial solar wind conditions, is the one pointing toward the Sun. Even though we cannot make any real conclusions about eVDFs in the coronal regions which are critical for the solar wind acceleration, our results seem to indicate that closer to the Sun, less than 0.3 AU, the fraction of halo electrons in high-energy tails tends to vanish. Vice-versa, the strahl beam is possibly even stronger than what we observe beyond 0.3 AU. From our observations it is not clear whether or not the strahl will completely disappear, being after certain distance absorbed by the halo at the farther limit of the observed radial range.

7.2 Electron Temperature Anisotropies

In contradiction to the classical CGL relations, the solar wind electrons are typically observed in a nearly isotropic state. We have studied two possible mechanisms which can constrain the electron temperature anisotropy in the solar wind plasma, namely kinetic plasma instabilities and Coulomb collisions. For this purpose, we have fitted eVDF samples in our data set with a simplified two component model for the core and halo populations and excluded the removed the antisunward part of the eVDF, which includes the strahl, from the fitting procedure. The electron temperature anisotropy was then estimated by the fitting parameters of analytical core/halo models of velocity distribution functions. We have then examined the effect of electron temperature anisotropy instabilities and Coulomb collisions and have shown that both, the instabilities as well as Coulomb collisions, influence the temperature anisotropy of the solar wind electrons.

In the case of the slow solar wind having higher electron parallel plasma beta (i.e. $\beta_{||} \gtrsim 1$), the temperature anisotropy of the core population is well constrained

by thresholds of the whistler and fairly well of the fire hose electron instabilities predicted by the linear theory. Similar mechanisms may also act for the non thermal halo component of the solar wind electrons. However, in this case the prediction of the instability thresholds from the linear theory has to be recomputed using a corresponding model for the distribution function. For the fast wind, electron populations are quite well localized far away from unstable regions in the $(T_\perp/T_{||}, \beta_{||})$ space. Consequently, it is hard to make any conclusions about the electron anisotropy constraints in the fast solar wind, neither for the core nor for the halo population. This is because our statistics in this case is not sufficient. For further studies this part of the data set has to be completed.

Even though the solar wind is usually considered to be a collisionless medium, our results show that electron Coulomb collisions still may have an effect to maintain the temperature anisotropy of the core population. This was demonstrated by use of the electron collisional age and it is in agreement with already published results (*Phillips et al.* (1989) and *Salem et al.* (2003). With an increasing number of collisions suffered by electrons the temperature ratio $T_\perp/T_{||}$ tends to unity.

Since the measurements cover a large range of radial distances, we are also able to examine the radial evolution of the electron temperature anisotropy. We have shown that, in agreement with theoretical predictions, greater temperature anisotropies can develop at larger distances from the Sun. However, there is no clear evolution of the data in the $(T_\perp/T_{||}, \beta_{||})$ space as a function of the radial distance. The situation is more interesting if we look at the evolution in the $(T_\perp/T_{||}, \beta_{||})$ space as a function of collisions. There is a clear trend in the evolution of the core electron populations in dependence upon the collisional age. By virtue of these results, we suggest the core electron Coulomb collisions to be the basic mechanism driving the electron temperature anisotropy of the solar wind electron population. The importance of kinetic instabilities is increasing for higher parallel electron plasma betas.

Note that the electron collisional age used in our study is not the only way to express the importance of collisions in a medium. Furthermore the collisional age does not apply to the trapped electrons that circle on closed magnetic field lines. Another way of judging the collision state of the environment is to use the Knudsen number K_n, which is defined as the ratio between the mean free path and the typical density or temperature scale height of the medium. In order to verify the conclusions based on the collisional age, we have followed the same analysis of the temperature anisotropy with the Knudsen number K_n. The results based on the usage of the Knudsen number are qualitatively the same as obtained by using the electron collisional age. This supports our conclusions about the effect of collisions on the electron temperature anisotropy.

7.3 Electron Heat Flux

As the last, however, the most important parameter from the basic eVDF moments, we have studied the properties of the electron heat flux. We estimate the electron heat flux by numerical integration of our model eVDF fitted to eVDF samples in

our data set. The model eVDF was shown to well describe all components of eVDFs observed in the solar wind. The numerical integration thus should provide a more precise estimation of the electron heat flux than direct discrete integration of the measured eVDF samples. We have computed the electron heat flux separately for core, halo and strahl components. We have shown, that, in our model, the bulk of the overall electron heat flux is carried by the strahl. The strahl heat flux is than only fractionally balanced by sunward heat flux of the core and halo components.

The observed radial evolution of the total electron heat flux was found to be consistent with early observations of *Pilipp et al.* (1990) in the Helios radial range. However, the power law deduced from our data set above 1 AU is found to be less steep than it was reported in *Scime et al.* (1994a). We have further compared the estimated heat flux to a general theoretical law derived for the theoretical predictions of *Spitzer and Härm* (1953) applied to an expansion along spiral oriented magnetic field lines (*Scime et al.* (1994a)). Our findings indicate that although the heat flux magnitude does not reach the predicted value for collisional transport it seems to be still driven by the local temperature gradient.

We have further examined, whether the observed values of the electron heat flux are constrained by imposed threshold conditions of some kinetic plasma instabilities and how is the heat flux biased from the theoretical predictions by the limited effect of Coulomb collisions. We provide an observational evidence, that the normalized electron heat flux has a net upper bound which is very close to the threshold condition estimated in *Gary et al.* (1999) for the whistler heat flux instability. The role of Coulomb collisions in regulation of the solar wind heat flux was expressed in terms of the electron collision frequency. Our estimation of the electron heat flux confirm that the theoretical collisional heat flux of *Spitzer and Härm* (1953) represents an upper limit which is not reached in the solar wind plasmas. However, with increasing collision frequency the observed electron heat flux draw nearer the collisional one.

7.4 Summary and Perspectives

We provided a quite comprehensive observational insight on the radial evolution of electron populations in the solar wind as they were measured *in situ* in low latitudes near the ecliptic plane. By fitting of the measured eVDF samples with a new fully analytical model, we first examined the density and temperature of the core, halo and strahl eVDF components respectively. As a summary of all fitting parameters of our model, averaged over the whole data set, we presented the radial evolution of the model eVDF in both slow and fast solar wind regimes. We confirmed by our analysis that observed radial profiles of electron characteristics do not follow a pure adiabatic radial expansion. These findings imply other mechanisms providing some additional heating or energy dissipation seem to be effective during the radial evolution of solar wind eVDFs. Therefore, we analysed possible constraints of electron temperature anisotropies and the electron heat flux imposed by kinetic plasma instabilities and Coulomb collisions. We presented an observational evidence

that both kinetic plasma instabilities and Coulomb collisions can possibly explain observed eVDF properties.

However, there are still other aspects concerning the properties of the measured eVDFs in the solar wind (especially of the high-energy tails) which we did not examine in current study. For example we did not study the angular broadening of the velocity distribution of strahl electrons as it was done, for instance, by *Hammond et al.* (1996). The majority of our data set comes from Helios measurements. In this case only eight angular bins are acquired which makes angular analysis less accurate. We have also presented most of the results only as a function of the heliocentric radial distance. In order to better understand the mechanisms responsible for the scattering of strahl electrons, we will also need to examine the evolution of the non-thermal eVDF tails with respect to Coulomb collisions and, if possible, with the observed intensity of electromagnetic oscillations.

In the case of electron temperature anisotropies, we have to notice that we omitted possible effects of the strahl population. In particular, we did not examine whether the electron heat flux, provided by the strahl component, have some relation with the observed ratio of parallel and perpendicular electron temperatures. Since both temperature anisotropies and electron heat flux give rise to several unstable wave modes which in turn can constrain the eVDF properties, they should be better studied altogether. However, this involve first some (probably numerical) solution of linear dispersion theory applied on true eVDFs observed in the solar wind.

Finally, one should remind that most of our conclusions are relevant for the slow solar wind near the ecliptic plane only since in our data set the number of fast wind observations is considerably limited. Furthermore more the present study should be also extend to out-ecliptic observations and it would be desirable to provide similar analysis for some shorter periods and special events. Obviously, there are still open questions and issues which we would like to examine in our future studies.

Bibliography

Bame, S. J., J. R. Asbridge, W. C. Feldman, J. T. Gosling, and R. D. Zwickl (1981), Bi-directional streaming of solar wind electrons greater than 80 eV - ISEE evidence for a closed-field structure within the driver gas of an interplanetary shock, *Geophys. Res. Lett.,* , *8*, 173–176.

Bame, S. J., D. J. McComas, B. L. Barraclough, J. L. Phillips, K. J. Sofaly, J. C. Chavez, B. E. Goldstein, and R. K. Saturai (1992), The Ulysses solar wind plasma experiment, *Astron. Astrophys. Suppl. Ser.*, *92*, 237–265.

Baumjohann, W., and R. A. Treumann (1996), *Basic space plasma physics*, London: Imperial College Press, —c1996.

Chew, G. F., M. L. Goldberger, and F. E. Low (1956), The Boltzmann euqtion and the one-fluid hydromagnetic equations in the absence of particle collisions, *Proc. R. Soc. London*, *236*, 112.

Crooker, N. U., S. W. Kahler, D. E. Larson, and R. P. Lin (2004), Large-scale magnetic field inversions at sector boundaries, *Journal of Geophysical Research (Space Physics)*, *109*, 3108–+, doi:10.1029/2003JA010278.

Dum, C. T., E. Marsch, and W. Pilipp (1980), Determination of wave growth from measured distribution functions and transport theory, *Journal of Plasma Physics*, *23*, 91–113.

Escoubet, C., R. Schmidt, and M. Goldstein (1997), Cluster: Science and mission overview, *Space Sci. Rev.*, *79*, 11–32.

Feldman, W., J. R. Asbridge, S. J. Bame, M. D. Montgomery, and S. P. Gary (1975), Solar wind electrons, *J. Geophys. Res.*, *80*, 4181–4196.

Fludra, A., G. Del Zanna, D. Alexander, and B. J. I. Bromage (1999), Electron density and temperature of the lower solar corona, *J. Geophys. Res.*, *104*, 9709–9720, doi:10.1029/1998JA900033.

Forslund, D. W. (1970), Instabilities associated with heat conduction in the solar wind and their consequences., *J. Geophys. Res.,* , *75*, 17–28, doi:10.1029/JA075i001p00017.

Gary, S. P. (1993), *Theory of Space Plasma Microinstabilities*.

Gary, S. P., and H. Li (2000), Whistler Heat Flux Instability at High Beta, *Astrophys. J.,* , *529*, 1131–1135, doi:10.1086/308294.

Gary, S. P., and K. Nishimura (2003), Resonant electron firehose instability: Particle-in-cell simulations, *Physics of Plasmas*, *10*, 3571–+.

Gary, S. P., and S. Saito (2007), Broadening of solar wind strahl pitch-angles by the electron/electron instability: Particle-in-cell simulations, *Geophys. Res. Lett.,* , *34*, 14,111–+, doi:10.1029/2007GL030039.

Gary, S. P., and J. Wang (1996), Whistler instability: Electron anisotropy upper bound, *J. Geophys. Res.*, *101*, 10,749–10,754, doi:10.1029/96JA00323.

Gary, S. P., W. C. Feldman, D. W. Forslund, and M. D. Montgomery (1975), Electron heat flux instabilities in the solar wind, *Geophys. Res. Lett.,* , *2*, 79–82, doi:10.1029/GL002i003p00079.

Gary, S. P., E. E. Scime, J. L. Phillips, and W. C. Feldman (1994), The whistler heat flux instability: Threshold conditions in the solar wind, *J. Geophys. Res.,* , *99*, 23,391–+.

Gary, S. P., E. Neagu, R. M. Skoug, and B. E. Goldstein (1999), Solar wind electrons: Parametric constraints, *J. Geophys. Res.*, *104*, 19,843–19,850, doi:10.1029/1999JA900244.

Gary, S. P., B. Lavraud, M. F. Thomsen, B. Lefebvre, and S. J. Schwartz (2005), Electron anisotropy constraint in the magnetosheath: Cluster observations, *Geophys. Res. Lett.,* , *32*, 13,109–+, doi:10.1029/2005GL023234.

Geach, J., S. J. Schwartz, V. Génot, O. Moullard, A. Lahiff, and A. N. Fazakerley (2005), A corrector for spacecraft calculated electron moments, *Annales Geophysicae*, *23*, 931–943.

Génot, V., and S. Schwartz (2004), Spacecraft potential effects on electron moments derived from a perfect plasma detector, *Annales Geophysicae*, *22*, 2073–2080.

Gosling, J. T., D. N. Baker, S. J. Bame, W. C. Feldman, R. D. Zwickl, and E. J. Smith (1987), Bidirectional solar wind electron heat flux events, *J. Geophys. Res.,* , *92*, 8519–8535.

Gosling, J. T., S. J. Bame, W. C. Feldman, D. J. McComas, J. L. Phillips, and B. E. Goldstein (1993), Counterstreaming suprathermal electron events upstream of corotating shocks in the solar wind beyond approximately 2 AU: ULYSSES, *Geophys. Res. Lett.,* , *20*, 2335–2338, doi:10.1029/93GL02489.

Gustafsson, G., et al. (1997), The Electric Field and Wave Experiment for the Cluster Mission, *Space Science Reviews*, *79*, 137–156, doi:10.1023/A:1004975108657.

Hammond, C. M., W. C. Feldman, D. J. McComas, J. L. Phillips, and R. J. Forsyth (1996), Variation of electron-strahl width in the high-speed solar wind: ULYSSES observations., *Astron. Astrophys.,* , *316*, 350–354.

Hellinger, P., P. Trávníček, J. C. Kasper, and A. J. Lazarus (2006), Solar wind proton temperature anisotropy: Linear theory and WIND/SWE observations, *Geophys. Res. Lett.,* , *33*, 9101–+, doi:10.1029/2006GL025925.

Hollweg, J. V. (1974), On electron heat conduction in the solar wind., *J. Geophys. Res.,* , *79*, 3845–3850, doi:10.1029/JA079i025p03845.

Hollweg, J. V., and H. J. Volk (1970), New plasma instabilities in the solar wind, *J. Geophys. Res.*, *75*, 5297.

Huba, J. D. (2007), *NRL Plasma Formulary*, Washington, DC: Naval Research Lab.

Hundhausen, A. J. (1969), Nonthermal heating in the quiet solar wind., *J. Geophys. Res.,* , *74*, 5810–5813, doi:10.1029/JA074i024p05810.

Hundhausen, A. J. (1972), *Coronal Expansion and Solar Wind*.

Issautier, K., N. Meyer-Vernet, M. Moncuquet, and S. Hoang (1998), Solar wind radial and latitudinal structure - electron density and core temperature from ulysses thermal noise spectroscopy, *J. Geophys. Res.*, *103*, 1969.

Johnstone, A. D., et al. (1997), Peace: A plasma electron and current experiment, *Space Sci. Rev.*, *79*, 351–398.

Jokipii, J. R., and B. Thomas (1981), Effects of drift on the transport of cosmic rays. IV - Modulation by a wavy interplanetary current sheet, *Astrophys. J.,* , *243*, 1115–1122, doi:10.1086/158675.

Kasper, J. C., A. J. Lazarus, S. P. Gary, and A. Szabo (2003), Solar Wind Temperature Anisotropies, in *Solar Wind Ten*, *American Institute of Physics Conference Series*, vol. 679, edited by M. Velli, R. Bruno, F. Malara, and B. Bucci, pp. 538–541.

Kennel, C. F., and H. E. Petscheck (1966), Limit on stably trapped particle fluxes, *J. Geophys. Res.*, *71*, 1–28.

Lamy, H., V. Pierrard, M. Maksimovic, and J. F. Lemaire (2003), A kinetic exospheric model of the solar wind with a nonmonotonic potential energy for the protons, *Journal of Geophysical Research (Space Physics)*, *108*, 1047–+, doi:10.1029/2002JA009487.

Lemaire, J., and M. Scherer (1971), Kinetic models of the solar wind., *J. Geophys. Res.,* , *76*, 7479–7490.

Li, X., and S. R. Habbal (2000), Electron kinetic firehose instability, *J. Geophys. Res.,* , *105*, 27,377–27,386, doi:10.1029/2000JA000063.

Lie-Svendsen, Ø., V. H. Hansteen, and E. Leer (1997), Kinetic electrons in high-speed solar wind streams: Formation of high-energy tails, *J. Geophys. Res.,* , *102*, 4701–4718, doi:10.1029/96JA03632.

Livi, S., and E. Marsch (1987), Generation of solar wind proton tails and double beams by Coulomb collisions, *J. Geophys. Res.,* , *92*, 7255–7261, doi: 10.1029/JA092iA07p07255.

Livi, S., E. Marsch, and H. Rosenbauer (1986), Coulomb collisional domains in the solar wind, *J. Geophys. Res.,* , *91*, 8045–8050.

Maksimovic, M. (2007), On the Existence of Non-maxwellian Velocity Distribution Functions in the Corona and their Consequences for the Solar Wind Acceleration, in *Lecture Notes in Physics, Berlin Springer Verlag*, *Lecture Notes in Physics, Berlin Springer Verlag*, vol. 725, edited by K.-L. Klein and A. L. MacKinnon, pp. 191–+.

Maksimovic, M. (2009), Private communication.

Maksimovic, M., V. Pierrard, and J. F. Lemaire (1997a), A kinetic model of the solar wind with Kappa distribution functions in the corona., *Astron. Astrophys.,* , *324*, 725–734.

Maksimovic, M., V. Pierrard, and P. Riley (1997b), Ulysses electron distributions fitted with Kappa functions, *Geophys. Res. Lett.,* , *24*, 1151–1154, doi: 10.1029/97GL00992.

Maksimovic, M., S. P. Gary, and R. M. Skoug (2000), Solar wind electron suprathermal strength and temperature gradients: Ulysses observations, *J. Geophys. Res.*, *105*, 18,337.

Maksimovic, M., V. Pierrard, and J. Lemaire (2001), On the Exospheric Approach for the Solar Wind Acceleration, *Astroph. and Space Science*, *277*, 181–187, doi: 10.1023/A:1012250027289.

Maksimovic, M., et al. (2005), Radial evolution of the electron distribution functions in the fast solar wind between 0.3 and 1.5 au, *J. Geophys. Res.*, *110*, A09104, doi: 10.1029/2005JA011119.

Marquardt, D. (1963), An algorithm of least-squares estimation of nonlinear parameters, *J. Appl. Math.*, *11*, 431–441.

Marsch, E. (2006), Kinetic Physics of the Solar Corona and Solar Wind, *Living Reviews in Solar Physics*, *3*, 1–+.

Marsch, E., R. Schwenn, H. Rosenbauer, K.-H. Muehlhaeuser, W. Pilipp, and F. M. Neubauer (1982), Solar wind protons - Three-dimensional velocity distributions and derived plasma parameters measured between 0.3 and 1 AU, *J. Geophys. Res.,* , *87*, 52–72, doi:10.1029/JA087iA01p00052.

Marsch, E., K. M. Thieme, H. Rosenbauer, and W. G. Pilipp (1989), Cooling of solar wind electrons inside 0.3 AU, *J. Geophys. Res.,* , *94*, 6893–6898.

Marsch, L. E., Zhao, and C.-Y. Tu (2006), Limits on the core temperature anisotropy of solar wind protons, *Annales Geophysicae*, *24*, 2057–2063.

Matteini, L., S. Landi, P. Hellinger, F. Pantellini, M. Maksimovic, M. Velli, B. E. Goldstein, and E. Marsch (2007), Evolution of the solar wind proton temperature anisotropy from 0.3 to 2.5 AU, *Geophys. Res. Lett.,* , *34*, 20,105–+, doi: 10.1029/2007GL030920.

McComas, D. J. (2003), The Three-Dimensional Structure of the Solar Wind Over the Solar Cycle, in *Solar Wind Ten*, *American Institute of Physics Conference Series*, vol. 679, edited by M. Velli, R. Bruno, F. Malara, and B. Bucci, pp. 33–38, doi:10.1063/1.1618535.

McComas, D. J., S. J. Bame, W. C. Feldman, J. T. Gosling, and J. L. Phillips (1992), Solar wind halo electrons from 1-4 AU, *Geophys. Res. Lett.,* , *19*, 1291–1294.

Meyer-Vernet, N. (2007), *Basics of the Solar Wind*, Basics of the Solar Wind, by Nicole Meyer-Vernet. ISBN-10 0-521-81420-0 (HB); ISBN-13 978-0-521-81420-1 (HB). Published by Cambridge University Press, Cambridge, UK, 2007.

Montgomery, M. D., S. J. Bame, and A. J. Hundhausen (1968), Solar Wind Electrons: Vela 4 Measurements, *J. Geophys. Res.,* , *73*, 4999–5003, doi: 10.1029/JA073i015p04999.

Owens, M. J., N. U. Crooker, and N. A. Schwadron (2008), Suprathermal electron evolution in a Parker spiral magnetic field, *Journal of Geophysical Research (Space Physics)*, *113*, 11,104–+, doi:10.1029/2008JA013294.

Paesold, G., and A. O. Benz (1999), Electron Firehose instability and acceleration of electrons in solar flares, *Astron. Astrophys.,* , *351*, 741–746.

Parker, E. N. (1958), Dynamical Instability in an Anisotropic Ionized Gas of Low Density, *Physical Review*, *109*, 1874–1876, doi:10.1103/PhysRev.109.1874.

Parker, E. N. (1963), *Interplanetary dynamical processes.*, New York, Interscience Publishers, 1963.

Phillips, J. L., and J. T. Gosling (1990), Radial evolution of solar wind thermal electron distributions due to expansion and collisions, *J. Geophys. Res.*, *95*, 4217–4228.

Phillips, J. L., J. T. Gosling, D. J. McComas, S. J. Bame, S. P. Gary, and E. J. Smith (1989), Anisotropic thermal electron distributions in the solar wind, *J. Geophys. Res.*, *94*, 6563–6579.

Pierrard, V., and J. Lemaire (1996), Lorentzian ion exosphere model, *J. Geophys. Res.,* , *101*, 7923–7934, doi:10.1029/95JA03802.

Pierrard, V., M. Maksimovic, and J. Lemaire (1999), Electron velocity distribution functions from the solar wind to the corona, *J. Geophys. Res.,* , *104*, 17,021–17,032, doi:10.1029/1999JA900169.

Pierrard, V., M. Maksimovic, and J. Lemaire (2001), Self-consistent model of solar wind electrons, *J. Geophys. Res.,* , *106*, 29,305–29,312, doi:10.1029/2001JA900133.

Pilipp, W. G., and A. O. Benz (1977), On the scattering hypothesis for type V radio bursts, *Astron. Astrophys.,* , *56*, 39–51.

Pilipp, W. G., K.-H. Muehlhaeuser, H. Miggenrieder, M. D. Montgomery, and H. Rosenbauer (1987a), Characteristics of electron velocity distribution functions in the solar wind derived from the HELIOS plasma experiment, *J. Geophys. Res.,* , *92*, 1075–1092.

Pilipp, W. G., K.-H. Muehlhaeuser, H. Miggenrieder, H. Rosenbauer, and R. Schwenn (1987b), Variations of electron distribution functions in the solar wind, *J. Geophys. Res.,* , *92*, 1103–1118.

Pilipp, W. G., K.-H. Muehlhaeuser, H. Miggenrieder, H. Rosenbauer, and R. Schwenn (1990), Large-scale variations of thermal electron parameters in the solar wind between 0.3 and 1 AU, *J. Geophys. Res.,* , *95*, 6305–6329, doi:10.1029/JA095iA05p06305.

Rosenbauer, H., et al. (1977), A survey on initial results of the HELIOS plasma experiment, *Journal of Geophysics Zeitschrift für Geophysik*, *42*, 561–580.

Saito, S., and S. P. Gary (2007), Whistler scattering of suprathermal electrons in the solar wind: Particle-in-cell simulations, *Journal of Geophysical Research (Space Physics)*, *112*, 6116–+, doi:10.1029/2006JA012216.

Salem, C., D. Hubert, C. Lacombe, A. Mangenay, D. Larson, and L. R.P. (2003), Electron properties and coulomb collisions in the solor wind at 1 au: Wind observations, *Astrophys. J.*, *585*, 1147–1157.

Schwenn, R., H. Rosenbauer, and H. Miggenrieder (1975), Das Plasmaexperiment auf Helios, *Raumfahrtforschung*, *19*, 226.

Scime, E. E., S. J. Bame, W. C. Feldman, S. P. Gary, J. L. Phillips, and A. Balogh (1994a), Regulation of the solar wind electron heat flux from 1 to 5 AU: ULYSSES observations, *J. Geophys. Res.,* , *99*, 23,401–+.

Scime, E. E., J. L. Phillips, and S. J. Bame (1994b), Effects of spacecraft potential on three-dimensional electron measurements in the solar wind, *J. Geophys. Res.,* , *99*, 14,769–+.

Scudder, J. D. (1992), Why all stars should possess circumstellar temperature inversions, *Astrophys. J.,* , *398*, 319–349, doi:10.1086/171859.

Scudder, J. D., and S. Olbert (1979), A theory of local and global processes which affect solar wind electrons. I - The origin of typical 1 AU velocity distribution functions - Steady state theory, *J. Geophys. Res.,* , *84*, 2755–2772.

Song, P., X. X. Zhang, and G. Paschmann (1997), Uncertainties in plasma measurements: effect of lower cutoff energy and spacecraft charge, *Planet. Space Sci.*, *45*, 255.

Spitzer, L. (1956), *Physics of Fully Ionized Gases*.

Spitzer, L., and R. Härm (1953), Transport Phenomena in a Completely Ionized Gas, *Physical Review*, *89*, 977–981, doi:10.1103/PhysRev.89.977.

Stix, T. H. (1992), *Waves in plasmas*.

Štverák, Š., P. Trávníček, M. Maksimovic, E. Marsch, A. N. Fazakerley, and E. E. Scime (2008), Electron temperature anisotropy constraints in the solar wind, *Journal of Geophysical Research (Space Physics)*, *113*, 3103–+, doi:10.1029/2007JA012733.

Štverák, Š., M. Maksimovic, P. M. Trávníček, E. Marsch, A. N. Fazakerley, and E. E. Scime (2009), Radial evolution of nonthermal electron populations in the low-latitude solar wind: Helios, Cluster, and Ulysses Observations, *Journal of Geophysical Research (Space Physics)*, *114*, 5104–+, doi:10.1029/2008JA013883.

Vocks, C., C. Salem, R. P. Lin, and G. Mann (2005), Electron Halo and Strahl Formation in the Solar Wind by Resonant Interaction with Whistler Waves, *Astrophys. J.,* , *627*, 540–549, doi:10.1086/430119.

Zouganelis, I., M. Maksimovic, N. Meyer-Vernet, H. Lamy, and K. Issautier (2004), A Transonic Collisionless Model of the Solar Wind, *Astrophys. J.,* , *606*, 542–554, doi:10.1086/382866.